*JETP Letters, Vol. 75, No. 11, 2002, pp. 527–529. From Pis'ma v Zhurnal Éksperimental'noĭ i Teoreticheskoĭ Fiziki, Vol. 75, No. 11, 2002, pp. 643–645.*


# Contribution of the $\pi^0\gamma$ and $\eta\gamma$ Intermediate States to Vacuum Polarization and the Muon Anomalous Magnetic Moment[1]

**N. N. Achasov* and A. V. Kiselev****

*Laboratory of Theoretical Physics, Sobolev Institute for Mathematics, Siberian Division, Russian Academy of Sciences, pr. Akademika Koptyuga 4, Novosibirsk, 630090 Russia*

** e-mail: achasov@math.nsc.ru*

*** e-mail: kiselev@math.nsc.ru*

Received April 26, 2002

Using new experimental data, we calculated, with a high precision, a contribution to the muon anomalous magnetic moment from the vacuum-polarization intermediate states $\pi^0\gamma$ and $\eta\gamma$ taking into account a correction for the trapezoidal rule: $a_\mu(\pi^0\gamma) + a_\mu(\eta\gamma) = (53.1 \pm 1.5) \times 10^{-11}$. We also determined a small contribution from the $e^+e^-\pi^0$, $e^+e^-\eta$, and $\mu^+\mu^-\pi^0$ intermediate states, which was found to be equal to $0.5 \times 10^{-11}$. © *2002 MAIK "Nauka/Interperiodica".*

PACS numbers: 13.40.Em; 14.60.Ef

New experimental data [1–3] allow one to calculate a contribution to the anomalous magnetic moment $a_\mu \equiv (g_\mu - 2)/2$ of a muon from the vacuum-polarization intermediate states $\pi^0\gamma$ and $\eta\gamma$ with a high accuracy. We also found a contribution from the $e^+e^-\pi^0$, $e^+e^-\eta$, and $\mu^+\mu^-\pi^0$ intermediate states.

A contribution to $a_\mu$ from an arbitrary vacuum-polarization intermediate state $X$ (hadrons, hadrons + $\gamma$, etc.) can be obtained via the dispersion integral

$$a_\mu = \left(\frac{\alpha m_\mu}{3\pi}\right)^2 \int \frac{ds}{s^2} K(s) R(s), \tag{1}$$

$$R(s) \equiv \frac{\sigma(e^+e^- \longrightarrow X)}{\sigma(e^+e^- \longrightarrow \mu^+\mu^-)},$$

$$\sigma(e^+e^- \longrightarrow \mu^+\mu^-) \equiv \frac{4\pi\alpha^2}{3s},$$

$$K(s > 4m_\mu^2) = \frac{3s}{m_\mu^2}\left\{x^2\left(1 - \frac{x^2}{2}\right) + (1+x)^2\left(1 + \frac{1}{x^2}\right)\right.$$

$$\left.\times\left[\ln(1+x) - x + \frac{x^2}{2}\right] + \frac{1+x}{1-x}x^2\ln(x)\right\}$$

$$= \frac{3}{a^3}\left(16(a-2)\ln\frac{a}{4} - 2a(8-a)\right.$$

$$\left. - 8(a^2 - 8a + 8)\frac{\operatorname{arctanh}(\sqrt{1-a})}{\sqrt{1-a}}\right),$$

$$x = \frac{1 - \sqrt{1 - 4m_\mu^2/s}}{1 + \sqrt{1 - 4m_\mu^2/s}}, \quad a = \frac{4m_\mu^2}{s}.$$

$$K(s < 4m_\mu^2) = \frac{3}{a^3}\left(16(a-2)\ln\frac{a}{4} - 2a(8-a)\right.$$

$$\left. - 8(a^2 - 8a + 8)\frac{\arctan(\sqrt{a-1})}{\sqrt{a-1}}\right).$$

By evaluating the integral in Eq. (1) using the trapezoidal rule and the experimental data from SND [1, 2] (Fig. 1a), one finds a contribution from $\pi^0\gamma$:

$$a_\mu^{\text{trap}}(\pi^0\gamma) = (46.2 \pm 0.6 \pm 1.3) \times 10^{-11}, \quad 600\ \text{MeV} < \sqrt{s} < 1039\ \text{MeV}. \tag{2}$$

The first error is statistical, and the second one is systematic. Note that the contribution from the $\phi$ region (970 MeV $< \sqrt{s} <$ 1039 MeV) is $0.7 \times 10^{-11}$.

For our level of accuracy, it is necessary to take into account the error of the trapezoidal rule. The point is that, when using the trapezoidal rule for determining an exact value of $R(s)$, we calculate not the integral, but a sum. So, there is a problem of removing the error of the trapezoidal rule. In our case we use three SND fits to $R(s)$ from [1], based on the vector dominance model [4] (Fig. 1) for the experimental data in the energy region 600 MeV $< \sqrt{s} <$ 970 MeV.

[1] This article was submitted by the authors in English.

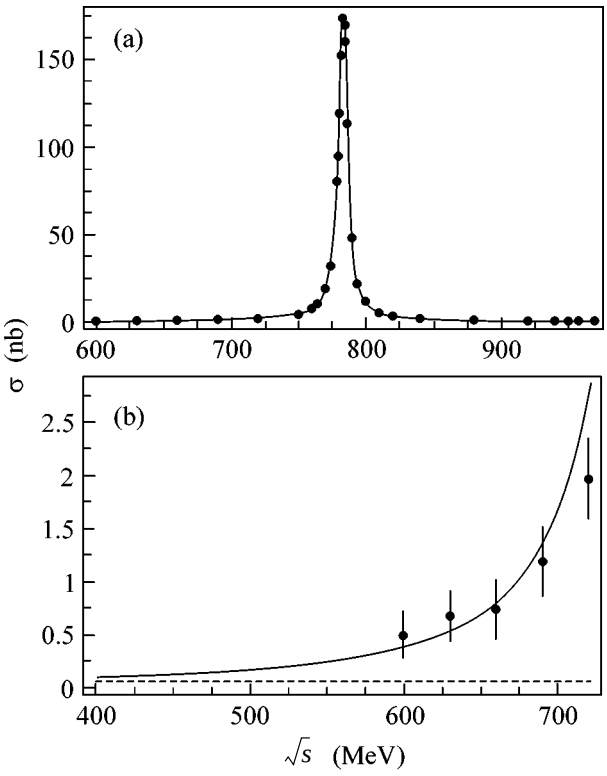


**Fig. 1.** (a) Plot of the dependence of $\sigma(e^+e^- \longrightarrow \pi^0\gamma)$ (in nb) on $\sqrt{s}$ (in MeV; SND experimental data and fit). (b) Comparison of the theoretical formulas for $\sigma(e^+e^- \longrightarrow \pi^0\gamma)$. Equation (6) is shown by the solid line, and the prediction of the pointlike model is shown by the dashed line.

We construct a new small quantity which represents the correction for the error of the trapezoidal rule,

$$\Delta a_\mu(\pi^0\gamma, E_1, E_N) = \left(\frac{\alpha m_\mu}{3\pi}\right)^2 \int_{s_1}^{s_N} \frac{ds}{s^2} K(s)R(s) - \sum_{i=1}^{N-1} \left(\frac{\alpha m_\mu}{3\pi}\right)^2 \frac{s_{i+1}-s_i}{2}\left[\frac{K(s_{i+1})R(s_{i+1})}{s_{i+1}^2} + \frac{K(s_i)R(s_i)}{s_i^2}\right], \quad (3)$$

where $E_i$ are the experimental energies, $E_1 = 600$ MeV, $E_N = 970$ MeV, $s_i = E_i^2$, and $R(s_i)$ are the SND fits. We get

$$\Delta a_\mu(\pi^0\gamma, 600\ \text{MeV}, 970\ \text{MeV}, fit) = -1.5 \times 10^{-11}. \quad (4)$$

This result varies by less than 1% for different fits. Note that the statistical error is also negligible ($0.01 \times 10^{-11}$). So, we can neglect the errors in Eq. (4) and add it to Eq. (2) to get the result

$$a_\mu(\pi^0\gamma) = (44.7 \pm 0.6 \pm 1.3) \times 10^{-11}, \quad 600\ \text{MeV} < \sqrt{s} < 1039\ \text{MeV}. \quad (5)$$

The point is that the values of both terms in Eq. (3), as calculated using the fits, have a nonnegligible model error. The contribution $a_\mu(\pi^0\gamma, 600\ \text{MeV}, 970\ \text{MeV})$ calculated using the SND fits differs by $\sim 0.4 \times 10^{-11}$ from fit to fit. But the difference $\Delta a_\mu(\pi^0\gamma, E_1, E_N)$ has a negligible model error because of the inequality $\Delta a_\mu(\pi^0\gamma, E_1, E_N) \ll a_\mu(\pi^0\gamma, E_1, E_N)$, although the relative model error is on the same order of magnitude.

For the energy region $\sqrt{s} < 600$ MeV, we use the following theoretical formula for the cross section:

$$\sigma(e^+e^- \longrightarrow \pi^0\gamma) = \frac{8\alpha f^2}{3}\left(1 - \frac{m_{\pi^0}^2}{s}\right)^3 \frac{1}{(1 - s/m_\omega^2)^2}, \quad (6)$$

where $f^2 = (\pi/m_{\pi^0}^3)\Gamma_{\pi^0 \to \gamma\gamma} \cong 10^{-11}/\text{MeV}^2$, according to [5]. Equation (6) is written in the approximation

$$\Gamma_\rho = \Gamma_\omega = 0, \quad m_\rho - m_\omega = 0. \quad (7)$$

The $\gamma^* \longrightarrow \pi^0\gamma$ amplitude is normalized to the $\pi^0 \longrightarrow \gamma\gamma$ amplitude at $s = 0$. The result is

$$a_\mu(\pi^0\gamma) = 1.3 \times 10^{-11}, \quad \sqrt{s} < 600\ \text{MeV}. \quad (8)$$

Note that the region $\sqrt{s} < 2m_\mu$ gives a negligible contribution of $2 \times 10^{-13}$.

We neglect small errors associated with the experimental error in width $\Gamma_{\pi^0 \to \gamma\gamma}$ (7%) and with approximation (7) (1.5%).

Equation (6) agrees with the data in the energy region $\sqrt{s} < 700$ MeV; at higher energies, approximation (7) does not work satisfactorily (Fig. 1b).

If we use a pointlike model, as in [6], we will obtain Eq. (6) without the factor $(1 - s/m_\omega^2)^{-2}$. The low-energies contribution predicted by this formula is several times lesser than given by Eq. (8) (Fig. 1b).

Treating the CMD-2 and SND data [2, 3] in the same manner and combining the results, one gets for the contribution from $\eta\gamma$

$$a_\mu(\eta\gamma) = (7.0 \pm 0.2 \pm 0.2) \times 10^{-11}, \quad 720\ \text{MeV} < \sqrt{s} < 1040\ \text{MeV}. \quad (9)$$

Note that the correction for the trapezoidal rule gives $-0.3 \times 10^{-11}$.

According to the quark model (and also to the vector dominance model), the energy range $\sqrt{s} < 720$ MeV is dominated by the $\rho$ resonance, and, hence, $\sigma(e^+e^- \longrightarrow \eta\gamma) \cong \sigma(e^+e^- \longrightarrow \rho \longrightarrow \eta\gamma)$. So, we can change Eq. (6) according to this fact and take into account the $\rho$ width, to obtain a small contribution

$$a_\mu(\eta\gamma) = 0.1 \times 10^{-11}, \quad \sqrt{s} < 720\ \text{MeV}. \quad (10)$$

Combining Eqs. (5), (8), (9), and (10), one can write

$$a_\mu(\pi^0\gamma) + a_\mu(\eta\gamma) = (53.1 \pm 0.6 \pm 1.4) \times 10^{-11}, \quad (11)$$

where the statistical and systematic errors are separately added in quadrature. In the table, we present our results with the statistical and systematic errors added in quadrature. Comparing Eq. (11) with the analogous calculation in [6] (table), one can see that our result is 23% greater and the error is 2.5 times smaller. Note that the increased result is mainly due to the interference of $\rho$ and $\omega$ in the $\pi^0\gamma$ channel, which was not taken into account in previous works, where the Breit–Wigner formula for the cross section was used. Contribution (11) accounts for 133% of the projected error of the E821 experiment at the Brookhaven National Laboratory ($40 \times 10^{-11}$) or 35% of the attained accuracy ($151 \times 10^{-11}$ [7]).

We can also take into account the intermediate state $\pi^0 e^+ e^-$ by using the obvious relation

$$\sigma(e^+e^- \longrightarrow \pi^0 e^+ e^-, s) = \frac{2}{\pi} \times \int_{2m_e}^{\sqrt{s}-m_{\pi^0}} \frac{dm}{m^2} \Gamma_{\gamma^* \to e^+e^-}(m) \sigma(e^+e^- \longrightarrow \pi^0\gamma^*, s, m), \quad (12)$$

where $m$ is the invariant mass of the $e^+e^-$ system,

$$\Gamma_{\gamma^* \to e^+e^-}(m) = (1/2)\alpha\beta_e m(1 - \beta_e^2/3),$$

$$\beta_e = \sqrt{1 - 4m_e^2/m^2},$$

$$\sigma(e^+e^- \longrightarrow \pi^0\gamma^*, s, m) = (p(m)/p(0))^3 \sigma(e^+e^- \longrightarrow \pi^0\gamma, s),$$

and

$$p(m) = (\sqrt{s}/2) \times \sqrt{(1 - (m_{\pi^0} + m)^2/s)(1 - (m_{\pi^0} - m)^2/s)}$$

is the c.m. momentum of $\gamma^*$.

In the same manner, we can calculate $a_\mu(\mu^+\mu^-\pi^0)$ and $a_\mu(e^+e^-\eta)$. The result is

$$a_\mu(e^+e^-\pi^0) + a_\mu(\mu^+\mu^-\pi^0) + a_\mu(e^+e^-\eta) = (0.4 + 0.026 + 0.057) \times 10^{-11} = 0.5 \times 10^{-11}. \quad (13)$$

Note that, if $m \gtrsim m_\rho$, we have the resonance excitation effect in the reaction $e^+e^- \longrightarrow \pi^0(\rho, \omega) \longrightarrow \pi^0 e^+ e^-$. However, this effect increases final result (13) by less than 10% because of the $(p(m)/p(0))^3$ factor, which suppresses the high value of $m$. So, we ignore this correction. We also neglect $a_\mu(\mu^+\mu^-\eta) = 2 \times 10^{-14}$.

Contribution to $a_\mu \times 10^{11}$

| State | Our value | Ref. [6] |
|---|---|---|
| $\pi^0\gamma$ | $46.0 \pm 1.4$ | $37 \pm 3$ |
| $\eta\gamma$ | $7.1 \pm 0.3$ | $6.1 \pm 1.4$ |
| $\pi^0\gamma + \eta\gamma$ | $53.1 \pm 1.5$ | $43 \pm 4$ |
| hadrons + $\gamma$, total | $95.7 \pm 2.1$ | $93 \pm 11$ |

As was noted in [6] and [8], it is also necessary to take into account

$$a_\mu(\text{hadrons} + \gamma, \text{rest}) = a_\mu(\pi^+\pi^-\gamma) + a_\mu(\pi^0\pi^0\gamma) + a_\mu(\text{hadrons} + \gamma, s > 1.2\ \text{GeV}^2).$$

We take $a_\mu(\pi^+\pi^-\gamma) = (38.6 \pm 1.0) \times 10^{-11}$ from [8] (see also [6]) and $a_\mu(\pi^0\pi^0\gamma) + a_\mu(\text{hadrons} + \gamma, s > 1.2\ \text{GeV}^2) = (4 \pm 1) \times 10^{-11}$ from [6]. Adding this to Eq. (11), we get

$$a_\mu(\text{hadrons} + \gamma, \text{total}) = (95.7 \pm 2.1) \times 10^{-11}. \quad (14)$$

Contribution (14) accounts for 239% of the projected error of the E821 experiment or 63% of the attained accuracy.

In fact, the errors in Eqs. (11) and (14) are negligible for any imaginable $(g - 2)_\mu$ measurement in the near future.

We thank A.D. Bukin for discussion of the correction for the trapezoidal rule. This work was supported in part by the Russian Foundation for Basic Research, project no. 02-02-16061.

## REFERENCES

1. M. N. Achasov, K. I. Beloborodov, A. V. Berdyugin, *et al.*, Preprint No. 2001-54, Inst. Yad. Fiz. Sib. Otd. Ross. Akad. Nauk (Budker Institute of Nuclear Physics, Siberian Division, Russian Academy of Sciences, Novosibirsk, 2001); http://www.inp.nsk.su/publications.
2. M. N. Achasov, A. V. Berdyugin, A. V. Bozhenok, *et al.*, Eur. Phys. J. C **12**, 25 (2000).
3. R. R. Akhmetshin, E. V. Anashkin, V. M. Aulchenko, *et al.*, Phys. Lett. B **509**, 217 (2001); hep-ex/0103043.
4. N. N. Achasov, M. S. Dubrovin, V. N. Ivanchenko, *et al.*, Yad. Fiz. **54**, 1097 (1991) [Sov. J. Nucl. Phys. **54**, 664 (1991)]; Int. J. Mod. Phys. A **7**, 3187 (1992).
5. Particle Data Group (D. E. Groom, M. Aguilar-Benítez, C. Amsler, *et al.*), Eur. Phys. J. C **15**, 1 (2000).
6. J. F. Troconiz and F. J. Yndurain, Phys. Rev. D **65**, 093001 (2002); hep-ph/0106025.
7. H. N. Brown, G. Bunce, R. M. Carey, *et al.*, Phys. Rev. Lett. **86**, 2227 (2001).
8. A. Hoefer, J. Gluza, and F. Jegerlehner, hep-ph/0107154.

JETP Letters, Vol. 75, No. 11, 2002, pp. 530–533. From Pis'ma v Zhurnal Éksperimental'noĭ i Teoreticheskoĭ Fiziki, Vol. 75, No. 11, 2002, pp. 646–650.


# On the Deconstruction of Time[1]

**Z. Berezhiani[1, 2, 3], A. Gorsky[4, 5], and I. I. Kogan[4, 6, 7, 8]**

[1] *Dipartimento di Fisica, University di L'Aquila, I-67010 Coppito AQ, Italy*
[2] *INFN, Laboratori Nazionali del Gran Sasso, I-67010 Assergi AQ, Italy*
[3] *Andronikashvili Institute of Physics, Academy of Sciences of Georgia, ul. Guramishvili 6, Tbilisi, 380077 Georgia*
[4] *Institute of Theoretical and Experimental Physics, ul. Bol'shaya Cheremushkinskaya 25, Moscow, 117259 Russia*
[5] *LPTHE, Université Paris VI, Paris, France*
[6] *Theoretical Physics, Department of Physics, Oxford University, Oxford, OX1 3NP, UK*
[7] *IHES, 91440 Bures-sur-Yvette, France*
[8] *Laboratoire de Physique Théorique, Université de Paris XI, 91405 Orsay Cédex, France*

Received April 29, 2002

In this note we discuss the possibility of getting a time rather than space in the scenario of (de)construction of a new dimension. © *2002 MAIK "Nauka/Interperiodica".*

PACS numbers: 11.10.Kk; 11.25.Mj

**1.** Recently, it was suggested in [1, 2] that a four-dimensional gauge theory with a large gauge symmetry behaves in the infrared region in a manner that is very similar to a five-dimensional gauge theory with a smaller gauge group. This leads to the idea of (de)construction of extra dimensions, i.e., that the extra dimensions do not exist at the fundamental level and emerge dynamically in the infrared limit. The basic idea of (de)construction is the following [1, 2]. One starts with a theory with a chain of gauge symmetries $G_1 \times G_2 \times \ldots G_N$, where all groups $G_i$ are identical; i.e., we have $N$ copies of the same gauge group $G$. Matter is represented by a set of scalar fields $\Phi_{i,\,i+1}$'s, each transformed as a fundamental representation with respect to symmetry $G_i$ and antifundamental with respect to the neighbor[2] $G_{i+1}$. These scalar fields $\Phi_{i,\,i+1}$ develop nonzero vacuum expectation values (VEV), and, hence, the total gauge symmetry will be broken down to a diagonal subgroup $G$. For simplicity, let us consider the case where $G = U(1)$; i.e., scalars $\Phi_{i,\,i+1}$ have charges $Q_i = 1$ and $Q_{i+1} = -1$ with respect to the neighbor groups $U(1)_i$ and $U(1)_{i+1}$. The system is described by the Lagrangian

$$\mathcal{L} = -\frac{1}{4g^2}\sum_{i=1}^{N} F_{(i)\mu\nu}F^{\mu\nu}_{(i)} - \sum_{i=1}^{N} D_\mu \Phi^\dagger_{i,\,i+1} D^\mu \Phi_{i,\,i+1} \quad (1)$$

[the signature (–, +, +, +) is chosen], where the covariant derivative is defined as $D_\mu = \partial_\mu + i\sum_i A_{(i)\mu}T^{(i)}$ and $T^{(i)}$ are the generators of gauge symmetry with respect to the group number $i$. Therefore, for a field $\Phi_{i,\,i+1}$ one gets

$$D_\mu \Phi_{i,\,i+1} = \partial_\mu \Phi_{i,\,i+1} + i(A_{(i)\mu} - A_{(i+1)\mu})\Phi_{i,\,i+1}. \quad (2)$$

When the order parameter $\Phi_{i,\,i+1}$ acquires a nonzero VEV, one has

$$\Phi_{i,\,i+1} = v\exp(i\phi_{i,\,i+1}/\sqrt{2}gv). \quad (3)$$

Neglecting in the infrared (IR) limit the kinetic energy $\partial_\mu v \partial^\mu v$, one can see that the scalar contribution to the Lagrangian is equal to

$$\frac{1}{2g^2}\sum_{i=1}^{N}(\partial_\mu \phi_{i,\,i+1} - \sqrt{2}gv(A_{(i+1)\mu} - A_{(i)\mu})) \times (\partial_\mu \phi_{i,\,i+1} - \sqrt{2}gv(A^\mu_{(i+1)} - A^\mu_{(i)})). \quad (4)$$

This term has the structure of a discrete version of $F_{\mu,5}F^{\mu,5}$, where phase $\phi_{i,\,i+1}$ is a phase of link variable for the component $A_5(x, i)$ and

$$\sqrt{2}gv(A_{(i+1)\mu} - A_{(i)\mu}) \longrightarrow \partial_5 A_\mu(x, i) + O(v^{-1})\partial_5^2 A_\mu(x, i). \quad (5)$$

The lattice spacing $a$ is related to the condensate $v$ by the relation

$$\sqrt{2}gva = 1, \quad (6)$$

so that the continuous limit corresponds to large $v$. In this model, one gets a "transverse-lattice" description of a full 4 + 1 gauge theory, where the size of extra

[1] This article was submitted by the authors in English.
[2] Alternatively, instead of the fundamental scalar fields one can consider some bilinear fermion condensates [1], but this is of little importance.

space $L$ is proportional to the number of independent gauge symmetries in the unbroken phase:

$$L = Na = N/\sqrt{2}gv. \quad (7)$$

It was shown recently that the deconstruction survives nonperturbatively in the supersymmetric case [3], and two compact dimensions, instead of one, can be constructed along this way if the full lattice of nonperturbative states is taken into account [4]. Moreover, recently attempts were made to introduce gravity into this scenario [5]. For other phenomenological applications of this approach, see [6].

**2.** Of course, this construction can be repeated for the spacetime of dimension and, starting with the $d$ + 1-dimensional spacetime, we can get $(d + 1)$ + 1-dimensional spacetime in the infrared limit. One can immediately raise the following question: is it possible to start with $d$-dimensional space and get $d$ + 1-dimensional spacetime? In other words, can we obtain time from nothing using (de)construction?

The answer to this question seems to be positive, but we have to work with the system involving the apparently tachyonic degrees of freedom. Actually, the different dependences of the vector and scalar degrees of freedom on the metric seems to be crucial for our purpose. Therefore, we explicitly restore the dependence on the metric in gauge action:

$$\mathcal{L} = -\frac{1}{4g^2}\sum_{i=1}^{N} g^{mn}g^{kl}F_{(i)mk}F_{(i)nl} - \sum_{i=1}^{N} g^{mn}D_m\Phi^{\dagger}_{i,i+1}D_n\Phi_{i,i+1} \quad (8)$$

and carefully study the metric which arises after deconstruction.

Consider first a spacetime with the metric $g_{nm}$ = diag(– + +…+) in the spirit of the example discussed in [1, 2]. For simplicity, let us consider the case $d = 3$ with $g_{nm}$ = diag(– + +). Lagrangian (8) leads to a well-defined action:

$$S = \int d^3x\sqrt{-g}\mathcal{L}. \quad (9)$$

For the choice of metric $g_{nm}$ = diag(+ – –), we have a wrong sign of the scalar part of the action (it would be ghostlike), but the gauge part is correct. The transition from the signature (– + +) to the signature (+ – –) is nothing but the transformation

$$g_{nm} \longrightarrow -g_{nm}, \quad (10)$$

and, obviously, the Lagrangian of vector fields is invariant under this transformation, while the kinetic part of the scalar Lagrangian is not. Let us note that the path integral for the theory with action (8) is defined with an oscillating exponent

$$\int DA_m(x)\prod_i D\Phi_{i,i+1}(x)\exp\{-i\int d^3x\sqrt{-g}\mathcal{L}\}. \quad (11)$$

In the low-energy limit, this path integral describes a gauge (Maxwell or Yang–Mills) theory including matter in a 3 + 1-dimensional spacetime with one extra compact spatial direction and metric $G_{\mu\nu}$ = diag(–+++).

Let us now turn to our main observation and show how the time coordinate can be generated if a metric different from $g_{nm}$ = diag(–++) is chosen before deconstruction. The most interesting possibility is to assume that our metric describes the Euclidean space; i.e., all directions have the same signature. There are formally two possibilities:

To take metric $g_E$ = diag(+ + +); i.e., all coordinates are spacelike coordinates in our original 2 + 1 spacetime (of course, there is no time now; it exists only when we have a quadratic form with an indefinite sign).

To take metric $g_L$ = diag(– – –); i.e., in our original 2 + 1 "spacetime" all coordinates are timelike coordinates, or, formally, they are spacelike, but the "kinetic" terms of $\Phi$ fields in Eq. (8) have the wrong sign.

In the first case, one can see that, starting with $g_E$, after deconstruction one gets the extra spatial coordinate and, hence, the Euclidean gauge theory in the $d = 4$ space:

$$G_E^{MN} = \delta^{MN}, \quad (12)$$

with the low-energy action

$$-iS = -i\frac{1}{4g^2}\int d^3xdy\sqrt{G_E}F_{MN}F_{MN}, \quad (13)$$

where the extra "i" amounts from the factor $\sqrt{-g}$, and it cancels with the factor "i" in the path integral (11), thus yielding an Euclidean field theory with a real path integral:

$$\int DA_M(x, y)\exp\{-S[A]\}. \quad (14)$$

Let us consider now the second choice, i.e., where we have metric $g_L$ = diag(–––). It is easy to see that, in this case, the relative signs of gauge and scalar sectors are different. If one considers a lattice regularization for the space, one can see that the scalar part corresponds to the antiferromagnetic coupling between the nearest neighbors, contrary to the ferromagnetic coupling in the space case: the state where neighbor fields are close to each other does not correspond to a minimum but to a maximum, implying the existence of the unstable mode. One can easily see that, upon repeating the same steps, we do not change anything in a gauge part (which now becomes the magnetic-field part of the action), but

because of the change of the sign of the scalar part, we effectively get an electric-field contribution.

The naive way to get the electric-field contribution $F_{0m}F^{0m} = -F_{0m}F_{0m}$ out of the Goldstone part is just to identify $\phi_{i,\,i+1}(x)$ as a scalar potential $A_0(x,\,i)$ and approximate in the expression

$$F_{0m}(x,\,i) = \partial_m\phi_{i,\,i+1}(x) - \sqrt{2}g\nu(A_{(i+1)m}(x) - A_{(i)m}(x)) \tag{15}$$

the combination $A_{(i+1)m}(x) - A_{(i)m}(x)$ as a time derivative $(dA_m/dt)\delta t$. In this view, the step of the "time lattice" is nothing but the inverse value of the condensate, $\delta t = 1/g\nu$. The higherderivative terms are suppressed by the large value of the condensate.

As a result, we get to the theory in a spacetime that has the Minkowski metric

$$G_L^{\mu\nu} = \mathrm{diag}(-,\,+,\,+,\,+). \tag{16}$$

Since the factor $\sqrt{-G}$ should appear in this case, there is no extra "i" when we go from 3 to 3 + 1 dimensions. Therefore, we derive the correct path integral (with complex phase) for the gauge theory in Lorentzian spacetime. Note also that the deconstruction effectively restores the symmetry $G_{MN} \longrightarrow -G_{MN}$, which becomes the effective low-energy symmetry.

One can be more precise and look more carefully on the "mass term" for the "*W*-bosons," which can be easily found from the action. In [1, 2], this term was immediately identified with Kalutza–Klein (KK) masses using the mode expansion of the gauge field $A(t,\,\mathbf{x},\,x_5)$. Now, since we are hunting for the time, it is natural to assume that such a term amounts from the mode expansion of $A_m(t,\,\mathbf{x})$ in $t$ variable. As far as the eigenvalues of the mass matrix have the structure $m_k = g\nu\sin(k/N)$ at large $N$, the linear spectrum of frequencies $\omega_k \propto k$ has to be somehow explained. In the KK case, it is just the consequence of the periodic or $Z_2$ orbifold boundary conditions. However, the case of time periodic conditions in the Minkowski space are not acceptable. Hence, in our case we could have only a kind of orbifold boundary conditions on the "boundary of the Universe" or free boundary conditions and infinite $N$. In principle, one can consider finite $N$, and this case will correspond to the "Universe" which originates at some moment and whose existence will be terminated at some later moment. Perhaps, this approach could be also useful for discussing periodic time, for example, the case of *AdS* spacetime.

Since the time direction emerges dynamically, we have to examine the Gauss law selecting the gauge invariant states at the quantum level. Let us compare how Gauss law and gauge invariance are realized in the KK and "time" cases. In the first case we have

$$\partial_m E_{(i)m} = \rho_i,$$
$$-\rho_i = \partial_0\phi_{i,\,i+1}(x) - \sqrt{2}g\nu(A_{(i+1)0}(x) - A_{(i)0}(x)) - \partial_0\phi_{i-1,\,i}(x) - \sqrt{2}g\nu(A_{(i)0}(x) - A_{(i-1)0}(x)). \tag{17}$$

One can easily see that, in a continuum limit, the density $\rho_i$ becomes nothing but $-\partial_5 E_5$. As a result, we get a five-dimensional Gauss law

$$\partial_m E_m + \partial_5 E_5 = 0. \tag{18}$$

A totally different story appears when we want to get time from deconstruction. In this case, we do not have an electric field to start with. One can see that the Gauss law $\partial_m E_m = 0$, which is supposed to be valid at any time moment $i$, can be written as

$$\partial_m F_{0m}(x,\,i) = \partial^2\phi_{i,\,i+1}(x) - \sqrt{2}g\nu(\partial_m A_m(x,\,i+1) - \partial_m A_m(x,\,i)) = 0. \tag{19}$$

One can choose all $\phi_{i,\,i+1}(x) = 0$ (this is the $A_0 = 0$ gauge). The Gauss law in this case reads

$$\partial_m A_m(x,\,i+1) = \partial_m A_m(x,\,i) \tag{20}$$

and corresponds to the time-independent gauge fixing.

Let us also comment on the possible relation between the quasiclassical nonperturbative configurations. It was argued in the KK supersymmetric case that the nonperturbative configurations are mapped onto each other under deconstruction [3]. In the time case, we would like to get, for instance, an instanton in the deconstructed theory. It can be obtained, indeed, considering the infinite arrow of monopoles in the $d = 3$ theory along the time direction.

**3.** Now let us briefly mention what the physical consequences of the picture proposed are. First, note that the perception of time as a chain of ordered events with no return to the past means just the fact that we measure observables in the $i$th sector only once. After we have measured it, we have to measure the next one and can never return, because the wave function in that sector is already defined. Second, it is natural to ask if a kind of appearance (or disappearance) of the time dimension in the IR (UV) limits, similar to what happens in the KK case, is possible. In the KK case, the condensate can be destroyed at large energies, yielding the effective disappearance of the fifth dimension. One can relate this to the uncertainty relation $\Delta x_5\Delta p_5 \geq 1$: when we try to localize the position in space, we bring such an uncertainty into the momentum, which causes the destruction of the condensate. If, for example, we destroy the condensate on the link $(i,\,i+1)$, it will cause the creation of two disconnected worlds. In the time case, one could also imagine the dynamical disappearance of the condensate, which would look as if time disappears. Again, if we try to destroy a condensate just on one link, it will

also cause the emergence of two disconnected worlds; but now they will be disconnected in time. Now, we have the uncertainty relation $\Delta E \Delta t \geq 1$, and because we have the time quanta $\Delta t \sim v^{-1}$, one cannot have $\Delta E \leq v$.

Our perception of time is a causally ordered sequence of measurement processes, each of which can happen only once. If time emerges in the manner as we have just described, this would mean that the observer can make a measurement for all gauge fields, but only once. In some sense, the full evolution is just a single complete measurement. This indeed sounds quite natural. When one asks what happens when we repeat a measurement, it is based on the assumption that we can measure something again later. But later means later in time, and if time itself emerges dynamically, this question simply cannot be asked. There is only *one* measurement for each sector, which means that you cannot return to the past and reobserve the things.

Among other interesting points to be questioned is the deconstruction of the $d = 2$ Yang–Mills (YM) theory. Since for $d = 2$ the YM theory is topological, only zero modes on the cylinder are relevant and all higher KK modes can be safely cut off. The theory, which amounts to the $d = 2$ YM theory after deconstruction, can be presented as $N$ copies of quantum mechanics where $N$ defines the radius of the cylinder. However, since only zero mode works, only one copy of quantum mechanics is relevant. Now, turn to the question concerning the signature of the $d = 2$ theory. Before deconstruction, the issue of the signature in quantum mechanics is subtle, since we have to deal with "world line" (time) and "target" (coordinate) simultaneously. It can be well-defined only for the relativistic particle, since the length of the world line is defined with some metric.

On the other hand, the $d = 2$ YM theory at large $N$ is equivalent to the $c = 1$ string theory; that is, what we are talking about is the deconstruction of the $c = 1$ string theory from the set of copies of quantum mechanics. Moreover, from the viewpoint of $c = 1$ string, we deconstruct the *target manifold*, since the $d = 2$ YM theory is defined on the target from the stringy point of view. How the second dimension emerges in the $c = 1$ string is known: it is the Liouville mode, while the $c = 1$ string theory can indeed be defined via matrix quantum mechanics. Hence, the issue of the resulting metric in the $d = 2$ theory is associated with the sign of the Liouville contribution to the action. Usually, it is assumed that the Liouville field plays the role of time. One more potential question concerns the deconstruction of the $(0 + 1)$ theory (quantum mechanics) from the copies of the $(0 + 0)$ (matrix model). This has something to do with the $M$(atrix) model deconstruction of $D0$ brane from the $D$ instantons.

It is known how the deconstruction procedure can be formulated in terms of branes. For instance, to get the quiver models one could take the set of $D3$ branes on orbifolds in supersymmetric case [7]; then $W$ bosons are represented by the strings connecting the pairs of $D3$ branes. When this paper was almost completed, preprint [8] appeared, where new branes localized in time direction were found. These branes are very natural objects to start with to get the new timelike coordinates in terms of the brane array leading to the group products. Since the fundamental strings can end on them, the spectrum of "masses" could be reproduced in a way similar to the KK case.

**4.** In conclusion, let us make our main statement again. Starting with action (8), it is possible to get a quantum field theory in a spacetime where either an extra spatial coordinate or extra time emerges via deconstruction. Alternatively, one can get statistical field theory.

Z.B. was supported in part by the MURST research grant "Astroparticle Physics," A.G. was supported in part by INTAS (grant no. 00-00334) and CRDF (grant no. RP2-2247), and I.I.K. was supported in part by the PPARC rolling grant no. PPA/G/O/1998/00567 and EC TMR grant HPRN no. CT-2000-00152.

## REFERENCES

1. N. Arkani-Hamed, A. G. Cohen, and H. Georgi, Phys. Rev. Lett. **86**, 4757 (2001); hep-th/0104005.
2. C. T. Hill, S. Pokorski, and J. Wang, Phys. Rev. D **64**, 105005 (2001); hep-th/0104035.
3. C. Csaki, J. Erlich, V. V. Khoze, *et al.*, hep-th/0110188.
4. N. Arkani-Hamed, A. G. Cohen, D. B. Kaplan, *et al.*, hep-th/0110146.
5. A. Sugamoto, hep-th/0104241; M. Alishahiha, Phys. Lett. B **517**, 406 (2001); hep-th/0105153; M. Bander, Phys. Rev. D **64**, 105021 (2001); hep-th/0107130.
6. H. C. Cheng, C. T. Hill, S. Pokorski, and J. Wang, Phys. Rev. D **64**, 065007 (2001); N. Arkani-Hamed, A. G. Cohen, and H. Georgi, Phys. Lett. B **513**, 232 (2001); hep-ph/0105239; C. Csaki, G. D. Kribs, and J. Terning, Phys. Rev. D **65**, 015004 (2002); hep-ph/0107266; K. Sfetsos, Nucl. Phys. B **612**, 191 (2001); hep-th/0106126; W. Skiba and D. Smith, hep-ph/0201056; N. Arkani-Hamed, A. G. Cohen, and H. Georgi, hep-th/0109082; T. Kobayashi, N. Maru, and K. Yoshioka, hep-ph/0110117.
7. M. R. Douglas and G. W. Moore, hep-th/9603167.
8. M. Gutperle and A. Strominger, hep-th/0202210.

JETP Letters, Vol. 75, No. 11, 2002, pp. 534–538. From Pis'ma v Zhurnal Éksperimental'noĭ i Teoreticheskoĭ Fiziki, Vol. 75, No. 11, 2002, pp. 651–654.


# Manifestation of the Nuclear Anapole Moment in the Thallium *M*1 Transitions[1]

**M. G. Kozlov**

*St. Petersburg Nuclear Physics Institute, Russian Academy of Sciences, Gatchina, Leningrad region, 188300 Russia*

*e-mail: mgk@MF1309.spb.edu*

Received April 29, 2002

We calculate the nuclear spin-dependent parity-nonconserving $E1$ amplitudes for the optical transition $6p_{1/2,F} \longrightarrow 6p_{3/2,F'}$ and hyperfine transition $6p_{1/2,F} \longrightarrow 6p_{1/2,F'}$ in $^{205}$Tl. The experimental limit placed upon the former amplitude by Vetter *et al.* [PRL 74, 2658 (1995)] corresponds to the anapole moment constant $\kappa_a = -0.26 \pm 0.27$. © *2002 MAIK "Nauka/Interperiodica".*

PACS numbers: 31.30.Jv; 32.80.Ys; 11.30.Er

In 1980, Flambaum and Khriplovich [1] pointed out that the nuclear spin-dependent (NSD) part of the parity-nonconserving (PNC) interaction in heavy atoms is dominated by the contribution of the nuclear anapole moment (AM) [2]. After that, AM was observed in the PNC experiment with $^{133}$Cs [3], where the measured value of the AM constant $\kappa_a$ appeared to be even larger than the theoretical prediction for the "best values" of the nuclear PNC interaction constants (see [4] and references therein). On the other hand, in the most accurate measurement of the PNC amplitudes for $6p_{1/2,F} \longrightarrow 6p_{3/2,F'}$ in $^{205}$Tl [5], the NSD amplitude was found to be consistent with zero and smaller than the theoretical predictions [4, 6].

In [6], the ratio between the NSD amplitude and the dominant nuclear spin-independent (NSI) PNC amplitude was calculated in the one-particle approximation. Here, we recalculate this ratio using the CI + MBPT method [7–9], which allows us to account for both core–valence and valence–valence correlations. We found that the correlation corrections are relatively large but do not explain the discrepancy between the measurement [5] and the theory [4]. A more accurate measurement of the NSD amplitude for the optical transition $6p_{1/2,F} \longrightarrow 6p_{3/2,F'}$ is hampered by the much larger NSI amplitude and the smallness of the hyperfine structure of the upper state. Consequently, it is easier to measure the PNC amplitude for the hyperfine transition $6p_{1/2,F} \longrightarrow 6p_{1/2,F'}$, where the NSI amplitude turns to zero, while the NSD amplitude is not suppressed [10]. Here, we find that the correlation corrections to this amplitude are 20%.

[1] This article was submitted by the author in English.

In the PNC experiments on the Tl $6p_{1/2} \longrightarrow 6p_{3/2}$ transition, the ratio

$$\mathcal{R} \equiv \mathrm{Im}(E1_{\mathrm{PNC}}/M1) \tag{1}$$

of the PNC amplitude to the magnetic amplitude was measured with an accuracy of 1% in [5] and 3% in [11]. In those experiments, the hyperfine structure of the lower level $6p_{1/2}$ was resolved. This allowed one to determine $\mathcal{R}(F)$ for two ground-state hyperfine levels, $F = 0$ and $F = 1$. For the $F = 0$ level, only the transition to $F' = 1$ of the $6p_{3/2}$ level is allowed, while for the $F = 1$ level the transitions to both upper hyperfine levels $F' = 1, 2$ are allowed. Accordingly, $\mathcal{R}(1)$ is a certain average of two transitions:

$$\mathcal{R}(0) \equiv \mathcal{R}(0, 1), \tag{2a}$$

$$\mathcal{R}(1) \equiv x^2\mathcal{R}(1, 1) + (1 - x^2)\mathcal{R}(1, 2), \tag{2b}$$

where the coefficient $x^2$ depends on the transition intensities and experimental conditions such as the line width and optical depth.

Observation of the $F$ dependence of the PNC amplitude is important because it can give information about the NSD part of the PNC interaction:

$$\begin{aligned} H_{\mathrm{PNC}} &= H_{\mathrm{NSI}} + H_{\mathrm{NSD}} \\ &= \frac{G_F}{\sqrt{2}}\left(-\frac{Q_W}{2}\gamma_5 + \frac{\kappa}{I}\boldsymbol{\alpha}\mathbf{I}\right)\rho(\mathbf{r}), \end{aligned} \tag{3}$$

where $G_F = 2.2225 \times 10^{-14}$ au is the Fermi constant of weak interaction, $Q_W$ is the nuclear weak charge, $\kappa$ is the dimensionless coupling constant, $\gamma_5$ and $\boldsymbol{\alpha} \equiv \gamma_0\boldsymbol{\gamma}$ are the Dirac matrices, $I$ is the nuclear spin ($I = \frac{1}{2}$ for both

stable $^{205}$Tl and $^{203}$Tl isotopes), and $\rho(\mathbf{r})$ is the nuclear density distribution.

There are three main contributions to the coupling constant $\kappa$ in the NSD part of PNC interaction (3):

$$\kappa = -\frac{2}{3}\kappa_a + \kappa_2 + \kappa_{Q_W}, \quad (4)$$

where the AM contribution is given by the constant $\kappa_a$ [1] and the constant $\kappa_2 = \frac{\lambda}{2}(4\sin\theta_W - 1) \approx -0.06$ corresponds to the NSD weak neutral currents.[2] The term $\kappa_{Q_W}$ is due to the interference of the NSI and hyperfine interactions. For heavy nuclei, this constant is proportional to $A^{2/3}$ [12, 13], and for Tl $\kappa_{Q_W} \approx 0.02$. Substituting these values in Eq. (4), we get

$$\kappa = -\frac{2}{3}(\kappa_a - 0.06). \quad (5)$$

Theoretical predictions for the AM constant depend on the nuclear model and vary within the range $0.1 \le \kappa_a \le 0.4$ (see [4] and references therein). On the other hand, for a given nuclear model, one can use the measured values of $\kappa_a$ to gain information on the coupling constants for the nuclear *P*-odd interaction [14–16].

In this article, we calculate the NSD amplitudes $6p_{1/2,F} \longrightarrow 6p_{3/2,F'}$ and use Eq. (5) and experimental results from [5] to place a limit on the AM constant $\kappa_a$. Following [5, 6], we use the parametrization

$$\mathcal{R}(F, F') = C(Z)[Q_W - 6\kappa\xi(F, F')], \quad (6)$$

which links the NSD amplitude to the NSI amplitude via the function $\xi(F, F')$. According to Eq. (2), one can define the function $\xi(F)$ as follows:

$$\xi(0) = \xi(0, 1), \quad (7a)$$

$$\xi(1) = x^2\xi(1, 1) + (1 - x^2)\xi(1, 2). \quad (7b)$$

An important property of the one-particle approximation is the equality $\xi(1, 1) = \xi(1, 2)$ [6], which means that $\xi(1)$ does not depend on the coefficient $x^2$ in Eqs. (2b) and (7b). Numerical values (obtained in [6]) are

$$\xi_{\rm op}(0) = 0.87, \quad \xi_{\rm op}(1) = -0.29. \quad (8)$$

In general, when the electron correlations are taken into account, $\xi(1, 1) \neq \xi(1, 2)$. Then, one has to use Eq. (6) for $\mathcal{R}(F, F')$ and calculate the function $\xi(F', F)$. After that, the experimental function $\xi(F)$ is given by Eq. (7). Consequently, the difference in the NSI and NSD amplitudes depends on the factor $x^2$.

The NSI amplitude was studied many times, the most advanced and accurate calculations being performed in [17, 18] (for earlier references, see [19]). It was shown there that the many-body corrections to the PNC amplitudes in Tl may be important. This stimulated us to recalculate the function $\xi(F, F')$. We follow here the same procedure as was used in [18]. It is based on a combination of the many-body perturbation theory for core–valence correlations and the configuration interaction for three valence electrons (CI + MBPT method) [7–9].

Most of the technical details of this calculation, such as the basis sets, configuration sets, etc., are the same as in [18], where a number of test calculations were made for the spectrum, hyperfine constants, $E1$ amplitudes, and polarizabilities. All these parameters were shown to be in good agreement with the experiment. This allowed us to estimate the accuracy of calculation of the NSI amplitude at a level better than 3%. Here, we use the same wave functions for the $6p_j$ states but neglect several smaller corrections (such as structural radiation) to the effective operators for valence electrons. The normalization correction is the same for the NDI and NSD amplitudes and does not affect the function $\xi(F', F)$.

In order to find the PNC amplitude, we solve the inhomogeneous equations

$$(E_{6p_{3/2}} - H^{\rm eff})\Psi^{(D)}_{a,m} = D_z^{\rm eff}\Psi_{6p_{1/2}m}, \quad (9)$$

$$(E_{6p_{1/2}} - H^{\rm eff})\Psi^{(D)}_{b,m} = D_z^{\rm eff}\Psi_{6p_{3/2}m}, \quad (10)$$

where $H^{\rm eff}$ is the effective Hamiltonian for valence electrons, which accounts for the core–valence correlations in the second-order many-body perturbation theory [7, 8], $D_z^{\rm eff}$ is the $z$ component of effective $E1$ amplitude in the length gauge [20], and $m$ is the magnetic quantum number. The solutions to these equations can be decomposed as a series in terms with definite angular quantum numbers $J$:

$$\Psi^{(D)}_{i,m} = \sum_J \Psi^{(D)}_{i,J,m}; \quad i = a, b. \quad (11)$$

The NSI amplitude can be found by calculating the following matrix elements:

$$E1_{\rm NSI} = (-1)^{\frac{3}{2}-m}\begin{pmatrix} \frac{3}{2} & 1 & \frac{1}{2} \\ -m & 0 & m \end{pmatrix}^{-1} \times (\langle \Psi_{6p_{3/2}}|H^{\rm eff}_{\rm NSI}|\Psi^{(D)}_{a,3/2}\rangle + \langle \Psi^{(D)}_{b,1/2}|H^{\rm eff}_{\rm NSI}|\Psi_{6p_{1/2}}\rangle), \quad (12)$$

where we omitted the index $m$ in the matrix elements and took advantage of the fact that $H^{\rm eff}_{\rm NSI}$ is diagonal in quantum number $J$. The NSD part of PNC interaction (3)

[2] Note that the radiative corrections can change $\kappa_2$ rather noticeably.

Calculated values of $\xi(F, F')$ in different approximations: configuration interaction (CI) for the three valence electrons and the CI + MBPT method; *a* and *b* correspond to the two contributions in Eqs. (12) and (13)

| $F, F'$ | CI | | | CI + MBPT | | |
|---|---|---|---|---|---|---|
| | *a* | *b* | total | *a* | *b* | total |
| 0, 1 | 1.09 | 1.29 | 1.20 | 1.08 | 1.12 | 1.10 |
| 1, 1 | −0.498 | −0.513 | −0.506 | −0.500 | −0.431 | −0.462 |
| 1, 2 | −0.337 | −0.413 | −0.378 | −0.331 | −0.361 | −0.348 |

can change this quantum number, and the corresponding amplitudes have a more complicated form:

$$E1_{\mathrm{NSD}} = \sum_{J=1/2}^{5/2} C(J, F, F') \times \left(\langle \Psi_{6p_{3/2}} | H^{\mathrm{eff}}_{\mathrm{NSD}} | \Psi^{(D)}_{a,J} \rangle + \langle \Psi^{(D)}_{b,J} | H^{\mathrm{eff}}_{\mathrm{NSD}} | \Psi_{6p_{1/2}} \rangle\right), \quad (13)$$

where the constants $C(J, F, F')$ are certain combinations of the 6*j* coefficients (see [21] for detail).

All wave functions in Eqs. (12) and (13) are many-electron ones. In the one-particle approximation, these expressions are simplified, and both NSI and NSD parts of the PNC amplitude have the form

$$E1_{\mathrm{PNC}} = \sum_n \frac{\langle 6p_{3/2}\|D\|ns_{1/2}\rangle\langle ns_{1/2}|H_{\mathrm{PNC}}|6p_{1/2}\rangle}{\varepsilon_{6p_{1/2}} - \varepsilon_{ns_{1/2}}}. \quad (14)$$

Here, the sum runs over the occupied ($n = 1, \ldots, 6$) and vacant ($n > 6$) states. The contribution of the occupied states with $n \le 5$ is very small, while $n = 6$ contributes almost as much as the whole sum over the vacant states. The term $n = 6$ corresponds to the amplitudes with index *b* in Eqs. (12) and (13). It can be seen that all intermediate states in Eq. (14) have $J = 1/2$. This leads to the equality $\xi(1, 1) = \xi(1, 2)$, which is incorrect for the more general case of Eq. (13). The many-body corrections are the strongest for the weak $F = 1 \longrightarrow F' = 1$ amplitude, which affects the value of $\xi(1, 1)$.

Our results for the function $\xi(F, F')$ are given in the table. We found them from the calculated amplitudes (12) and (13) using two approximations. At first, we used the configuration interaction method for the three valence electrons with conventional operators. Then, we used the second-order many-body perturbation theory to construct the effective Hamiltonian $H^{\mathrm{eff}}$ and the random phase approximation for the effective operators $D^{\mathrm{eff}}_z$ and $H^{\mathrm{eff}}_{\mathrm{PNC}}$.

It follows from the comparison of the table with one-particle approximation (8) that the correlation effects enhance the NSD amplitudes. For the weakest $F = 1 \longrightarrow F' = 1$ amplitude, the correlation correction exceeds 50%. For two other amplitudes, the correlations are less important but still account for 20–25% enhancement. The valence correlations are larger for the amplitudes *b*. A dominant contribution to these amplitudes corresponds to the intermediate states from the $6s6p^2$ configuration, where the correlations between two *p* electrons are very strong. In contrast, the main contributions to the amplitudes *a* correspond to the configurations $6s^2np$, where the correlations are much weaker.

We showed above that the correlation corrections to the NSD amplitudes are rather large. Moreover, our values of $\xi(1, 1)$ and $\xi(1, 2)$ noticeably differ from each other. This leads to the dependence of the experimentally observed amplitude (Eq. 2b) on $x^2$. The value of this parameter depends on the experimental conditions. In the linear regime, $x^2$ and $1 - x^2$ are proportional to the corresponding line intensities. This gives $x^2 = \frac{1}{6}$ [19]. The actual experiment [5] was done in the nonlinear regime, where the light was completely absorbed at the line center and the PNC signal was detected only at the wings. In these conditions, one can expect that $\frac{1}{6} \le x^2 \le \frac{1}{2}$. Below, we analyze each of the limiting cases.

If we substitute the values from the table into Eq. (7b), we get

$$\xi(0) = 1.10; \qquad \xi(1) = \begin{cases} -0.367, & x^2 = 1/6, \\ -0.405, & x^2 = 1/2. \end{cases} \quad (15)$$

The NSI amplitude can be found as a weighted average

$$\mathcal{R}_{\mathrm{NSI}} = \frac{\xi(0)\mathcal{R}(1) - \xi(1)\mathcal{R}(0)}{\xi(0) - \xi(1)}. \quad (16)$$

The experimental difference between $\mathcal{R}(1)$ and $\mathcal{R}(0)$ is only about 1%. Because of this, both values of $\xi(1)$ in Eq. (15) lead to the same value $\mathcal{R}_{\mathrm{NSI}} = -14.68 \times 10^{-8}$, in agreement with the result from [5].

The difference $\Delta\mathcal{R} \equiv \mathcal{R}(1) - \mathcal{R}(0)$ can be written as

$$\Delta\mathcal{R} = 6\kappa\frac{\xi(0) - \xi(1)}{Q_W}\mathcal{R}_{\mathrm{NSI}}, \quad (17)$$

$$\Delta\mathcal{R} = -4(\kappa_a + 0.06)\frac{\xi(0) - \xi(1)}{Q_W}\mathcal{R}_{\mathrm{NSI}}, \quad (18)$$

where we use relation (5) between $\kappa$ and $\kappa_a$. The table and Eq. (15) give $\xi(0) - \xi(1) = 1.49 \pm 0.02$, and, substituting the standard model value $Q_W = -116.7$ [22], we get

$$\Delta\mathcal{R} = (0.051 \pm 0.001)(\kappa_a + 0.06)\mathcal{R}_{\rm NSI}, \qquad (19)$$

where the error sign corresponds to two values of $x^2$ in Eq. (15) and does not take into account the theoretical error caused by the neglect of higher orders in the many-body perturbation theory. The latter was estimated in [18] for the NSI amplitude at a level close to 3%. Here, we neglect the structural radiation corrections and some other corrections which can contribute on a one-percent level, so we estimate the actual accuracy of Eq. (19) at about 5%. On this level, the uncertainty in the experimental conditions described by the parameter $x^2$ is negligible.

Using the experimental values from [5],

$$\mathcal{R}_{\rm NSI} = (-14.68 \pm 0.06 \pm 0.16) \times 10^{-8}, \qquad (20)$$

$$\Delta\mathcal{R} = (0.15 \pm 0.13 \pm 0.15) \times 10^{-8}, \qquad (21)$$

we get the following result for the AM constant:

$$\kappa_a = -0.26 \pm 0.27. \qquad (22)$$

In an independent measurement [11] of the PNC effects in Tl, a very close central value for the parameter $\Delta\mathcal{R}$ was obtained, though with an uncertainty that was three times larger. If we use Eq. (8) instead of Eq. (15), we get $\kappa_a = -0.32 \pm 0.35$. This means that the correlations account for 30% of the corrections and lead to a smaller absolute value of the AM constant. Note that in [5] the approximate values $\xi(0) = 1$ and $\xi(1) = -\frac{1}{3}$ were used instead of the more accurate one-particle values (8), and the relation $\kappa = -\frac{2}{3}\kappa_a$ was used instead of Eq. (5).

It was first recognized by Novikov and Khriplovich [10] that the NSD operator also leads to the $E1$ amplitude between the hyperfine sublevels of the same electronic state. The ground-state hyperfine transition is the most interesting in this respect. The corresponding amplitudes were calculated in the one-particle approximation for Cs and Tl [10] and for K [23]. The only many-body calculation was performed recently for Fr [21]. It is straightforward to recast Eq. (13) for this case, and all the calculations are similar to those for the optical transition. The result in au is

$$\langle 6p_{1/2}, 1 \| E1_{\rm NSD} \| 6p_{1/2}, 0 \rangle = 2.11 \times 10^{-11} i\kappa, \qquad (23)$$

where we use the same level of approximation as above and add the normalization correction [18]. In the one-particle approximation, the $M1$ amplitude for this transition is equal to $-\alpha/2\sqrt{3}$. The correlations change this value only at a subpercent level, and we can safely use it to calculate $\mathcal{R}$:

$$\mathcal{R}_{\rm hf}(6p_{1/2}) = -1.00 \times 10^{-8}\kappa = 0.67 \times 10^{-8}(\kappa_a + 0.06). \qquad (24)$$

Comparison of this value with the one obtained in [10] shows that the correlations increase the result by approximately 20%. Result (24) can also be compared with the $F = 4 \longrightarrow F' = 5$ transition in the $^{211}$Fr $7s$ ground state, where $\mathcal{R} = 3.9 \times 10^{-9}\kappa$ [21]. Although the $M1$ amplitude for the hyperfine transition in Tl is significantly smaller than in Fr, it would be much easier to do the experiment with stable Tl than with radioactive Fr. Note that for lighter Cs $\mathcal{R}$ is an order of magnitude smaller.

We see that the electron correlations account for the substantial corrections to the AM amplitudes but do not explain the difference between the experiment [5] and the prediction of nuclear theory that $\kappa_a = 0.25 \pm 0.15$ [4]. The experimental accuracy for the NSD amplitude of the $6p_{1/2} \longrightarrow 6p_{3/2}$ transition is not high, because this amplitude is much smaller, than the NSI amplitude. Therefore, it may be very interesting to measure the hyperfine amplitude (23), where the PNC effects are completely determined by the NSD part of the weak interaction. Note also that the hyperfine transition frequencies for two natural isotopes $^{203}$Tl and $^{205}$Tl differ by 1% and can be easily resolved. This enables one to measure the AM constants for each of the isotopes.

I am grateful to V.V. Flambaum, I.B. Khriplovich, and S.G. Porsev for valuable discussions. This work was supported by the Russian Foundation for Basic Research, project no. 02-02-16387.

## REFERENCES

1. V. V. Flambaum and I. B. Khriplovich, Zh. Éksp. Teor. Fiz. **79**, 1656 (1980) [Sov. Phys. JETP **52**, 835 (1980)].
2. Y. B. Zel'dovich, Zh. Éksp. Teor. Fiz. **33**, 1531 (1957) [Sov. Phys. JETP **6**, 1184 (1958)].
3. C. S. Wood, S. C. Bennett, D. Cho, *et al.*, Science **275**, 1759 (1997).
4. V. F. Dmitriev and I. B. Khriplovich, nucl-th/0201041.
5. P. A. Vetter, D. M. Meekhof, P. M. Magumder, *et al.*, Phys. Rev. Lett. **74**, 2658 (1995).
6. I. B. Khriplovich, Phys. Lett. A **197**, 316 (1995).
7. V. A. Dzuba, V. V. Flambaum, and M. G. Kozlov, Pis'ma Zh. Éksp. Teor. Fiz. **63**, 844 (1996) [JETP Lett. **63**, 882 (1996)].
8. V. A. Dzuba, V. V. Flambaum, and M. G. Kozlov, Phys. Rev. A **54**, 3948 (1996).
9. V. A. Dzuba, M. G. Kozlov, S. G. Porsev, and V. V. Flambaum, Zh. Éksp. Teor. Fiz. **114**, 1636 (1998) [JETP **87**, 885 (1998)].
10. V. N. Novikov and I. B. Khriplovich, Pis'ma Zh. Éksp. Teor. Fiz. **22**, 162 (1975) [JETP Lett. **22**, 74 (1975)].

11. N. H. Edwards, S. J. Phipp, P. E. G. Baird, and S. Nakayama, Phys. Rev. Lett. **74**, 2654 (1995).
12. V. V. Flambaum and I. B. Khriplovich, Zh. Éksp. Teor. Fiz. **89**, 1505 (1985) [Sov. Phys. JETP **62**, 872 (1985)].
13. C. Bouchiat and C. A. Piketty, Phys. Lett. B **269**, 195 (1991); Erratum: **274**, 526 (1992).
14. V. V. Flambaum and D. W. Murray, Phys. Rev. C **56**, 1641 (1997).
15. W. C. Haxton, C.-P. Liu, and M. J. Ramsay-Musolf, Phys. Rev. Lett. **86**, 5247 (2001).
16. W. C. Haxton and C. E. Wieman, Annu. Rev. Nucl. Part. Sci. **51**, 261 (2001); nucl-th/0104026.
17. V. A. Dzuba, V. V. Flambaum, P. G. Silvestrov, and O. P. Sushkov, J. Phys. B **20**, 3297 (1987).
18. M. G. Kozlov, S. G. Porsev, and W. R. Johnson, Phys. Rev. A **64**, 052107 (2001).
19. I. B. Khriplovich, *Parity Non-conservation in Atomic Phenomena* (Gordon and Breach, New York, 1991).
20. S. G. Porsev, Y. G. Rakhlina, and M. G. Kozlov, Phys. Rev. A **60**, 2781 (1999).
21. S. G. Porsev and M. G. Kozlov, Phys. Rev. A **64**, 064101 (2001).
22. D. E. Groom *et al.*, Eur. Phys. J. C **15**, 1 (2000).
23. V. G. Gorshkov, V. F. Ezhov, M. G. Kozlov, and A. I. Mikhailov, Yad. Fiz. **48**, 1363 (1988) [Sov. J. Nucl. Phys. **48**, 867 (1988)].

JETP Letters, Vol. 75, No. 11, 2002, pp. 539–542. Translated from Pis'ma v Zhurnal Éksperimental'noĭ i Teoreticheskoĭ Fiziki, Vol. 75, No. 11, 2002, pp. 655–659.


# On the Collapse of Wave Packets in a Medium with Normal Group Velocity Dispersion

**N. A. Zharova,* A. G. Litvak, and V. A. Mironov**

*Institute of Applied Physics, Russian Academy of Sciences, ul. Ul'yanova 46, Nizhni Novgorod, 603600 Russia*

** e-mail: zhani@appl.sci-nnov.ru*

Received April 5, 2002; in final form, April 25, 2002

A solution to the problem of realizing the collapse of three-dimensional wave packets in nonlinear media with normal group velocity dispersion is proposed. Wave packets with pronounced hyperbolic topology are shown to collapse; i.e., the field increases infinitely near the system axis. In particular, wave collapse of the tubular axisymmetric packets occurs through the concentration of the compressed ring field distribution at the axis. The collapse is shown to stabilize due to the saturation of nonlinearity or nonlinear dissipation, which restrict the field increase and lead to the packet splitting in the transverse direction. *© 2002 MAIK "Nauka/Interperiodica".*

PACS numbers: 42.25.Bs; 42.65.-k

As a rule, the group velocity dispersion of a laser pulse in condensed media is normal (the derivative $\partial v_{gr}/\partial\omega < 0$ is negative). For this reason, the dynamics of laser radiation self-action is described by a modified equation for the amplitudes of wave-packet envelope [1]. In dimensionless variables, the corresponding equation is a nonlinear Schrödinger equation (NSE) with a hyperbolic spatial operator [1–9]:

$$i\frac{\partial\psi}{\partial z} + \Delta_\perp\psi - \frac{\partial^2\psi}{\partial\tau^2} + |\psi|^2\psi = 0. \qquad (1)$$

Here, $\psi$ is the complex amplitude $E = E_{NL}\psi(z, x, y, \tau)\exp(i\omega t - ikz)$ of the electromagnetic-field envelope of a wave propagating along the $z$ axis with group velocity $v_{gr} = (dk/d\omega)^{-1}$; $E_{NL}$ is the characteristic nonlinear field; $\tau = (t - z/v_{gr})k^{3/2}c^2/(\omega|\partial v_{gr}/\partial\omega|^{1/2})$; the dimensionless evolution variable $z$ and the dimensionless transverse coordinates $x$ and $y$ are related to the corresponding dimensional variables $z_e$, $x_{tr}$, and $y_{tr}$ by $z = kz_e/2$ and $(x, y) = k(x_{tr}, y_{tr})$; $k$ is the wave number; and $\Delta_\perp = \partial^2/\partial x^2 + \partial^2/\partial y^2$.

Equation (1) is extensively used to describe the self-action of wave fields (upper-hybrid, cyclotron, etc.) in a magnetized plasma [2, 9–11].

Equation (1), as well as the standard NSE with an elliptic operator, has a number of integrals, among which the energy integral

$$I = \int|\psi|^2 d\mathbf{r}d\tau \qquad (2)$$

and Hamiltonian

$$H = \int(|\nabla_\perp\psi|^2 - |\psi_\tau|^2 - |\psi|^4/2)d\mathbf{r}d\tau \qquad (3)$$

are the most important. The Hamiltonian $H$ of the system accounts for the specific features of the wave-field self-action in Eq. (1). These features are associated with the competition between the processes in the longitudinal and transverse directions. In contrast to the elliptic NSE, the qualitative analyses of the self-action dynamics in the aberration-free approximation and the use of the method of moments did not provide any strong evidence for the occurrence of collapse in the system, but they also did not exclude this possibility [2, 8–10]. Numerical study of the processes has confirmed that the infinite transverse compression of the wave packet is hindered primarily by the packet instability, which leads to the pulse splitting in the transverse direction. At the same time, it is evident that there is a class of field distributions specific to the hyperbolic NSE for which the diffraction and dispersion processes compensate each other ($|\nabla_\perp\psi|^2 \simeq |\psi_\tau|^2$). For such distributions, the role of the nonlinear processes increases, as is seen from Eq. (3). Analytic and numerical studies of the evolution of two-dimensional ($\Delta_\perp = \partial^2/\partial x^2$) horseshoe field distributions corroborate this conclusion [13]. An even more pronounced enhancement of nonlinear effects can reasonably be expected in the three-dimensional case. Evidently, collapse occurs if the self-focusing compression toward the system axis proceeds faster than the splitting instability develops.

In this paper, we consider the evolution of axisymmetric wave structures and study analytically the dynamics of the three-dimensional horseshoe initial wave-field distributions. Under certain simplifying assumptions, we demonstrate that the wave-field distribution of this type narrows and shifts to the system axis ($z$ axis). In the self-similar "fall-to-center" process, the field amplitude tends to infinity; i.e., collapse occurs.

Numerical calculations of the dynamics are presented for a more realistic field distribution occurring in a tubular wave beam evolving toward the self-similar regime.

**1.** We note first that Eq. (1) for the function depending on the self-similar variable $\eta = \sqrt{r^2 - \tau^2}$ has the form

$$i\frac{\partial\psi}{\partial z} + \frac{1}{\eta^2}\frac{\partial}{\partial\eta}\eta^2\frac{\partial\psi}{\partial\eta} + |\psi|^2\psi = 0. \quad (4)$$

This equation describes the spherically symmetric collapse [13, 14]. This collapse is distributed and differs from the well-known self-focusing regime of axisymmetric beams by the fact that the resulting singularity is extended in $z$. In order to use the result obtained in [13, 14], we note that, in the case under consideration, the field is localized along the hyperbolas $\eta_0^2 = r^2 - \tau^2$. Therefore, the singularity arises at the "point" representing the cone surface $|\tau| = r$. The dynamics of the corresponding self-similar field distribution $\psi = \psi(z, \sqrt{r^2 - \tau^2})$ inside the cone ($|\tau| > r$) is described by Eq. (4), though with defocusing nonlinearity, i.e., with the minus sign of the nonlinear term.

It is convenient to analyze the evolution of the initial distributions localized near the hyperboloids $\eta^2 = r^2 - \tau^2$ in the new variables

$$\zeta = (r^2 - \tau^2)/4, \quad \tau = \tau. \quad (5)$$

This transformation makes it possible to investigate the evolution of the $\tau$-even wave-field distribution both in the region of focusing nonlinearity (outside the cone, $|\tau| < r$; i.e., $\zeta > 0$) and in the defocusing region, where the dispersion prevails over the diffraction (inside the cone, $|\tau| > r$; i.e., $\zeta < 0$). For definiteness, we consider the self-action dynamics in the half-space $0 < \tau < \infty$, $0 < r < \infty$ ($0 < \tau < \infty$, $-\infty < \zeta < \infty$ in new variables). It is convenient to transform Eq. (1) and introduce some simplifications using the variational approach. In variables (5), the action with the Lagrangian density has the form

$$S = \int\Big(\frac{i}{2}(\psi\psi_z^* - \psi^*\psi_z) + \zeta\Big|\frac{\partial\psi}{\partial\zeta}\Big|^2 - \Big|\frac{\partial\psi}{\partial\tau}\Big|^2 + \frac{\tau}{2}(\psi_\zeta^*\psi_\tau + \psi_\zeta\psi_\tau^*) - \frac{|\psi|^4}{2}\Big)d\zeta d\tau. \quad (6)$$

We assume first that the wave beam retains its Gaussian shape along $\tau$ in the course of evolution,

$$\psi = \frac{u(\zeta, z)}{\sqrt{b}}\exp\Big(-\frac{\tau^2}{2b^2}\Big), \quad (7)$$

and carry out corresponding simplifications for the Lagrangian density. Using the expression for the reduced action, one can derive the Euler equation describing the wave-field evolution along the hyperbolas:

$$i\frac{\partial u}{\partial z} + \frac{\partial}{\partial\zeta}\zeta\frac{\partial u}{\partial z} + \frac{|u|^2 u}{2b\sqrt{2}} = 0. \quad (8)$$

It can be seen that this approach enables one to explicitly separate the main singularity associated with the compensation of diffraction by the normal dispersion at the cone surface $r = |z|$. In the region $\zeta > 0$, the dispersion term in Eq. (8) is positive and wave-field self-focusing is possible. For $\zeta < 0$, the dispersion term is negative, and Eq. (8) describes self-defocusing. At the boundary where the self-action changes its character ($\zeta = 0$), the dispersion term vanishes.

Using the integrals of the set of Eqs. (2) and (3), the equation of motion for the wave-field center of mass $\rho(z) = \int\zeta|u|^2 d\zeta/I$ can be written in the form

$$d^2\rho/dz^2 = 2H/I, \quad (9)$$

where

$$H = \int\Big(\zeta\Big|\frac{\partial u}{\partial\zeta}\Big|^2 - \frac{u^4}{2b\sqrt{2}}\Big)d\zeta$$

in new variables (5). In the most interesting case of negative Hamiltonian ($H < 0$), the center of mass of a wave packet concentrated in the focusing region ($\rho \geq 0$) "accelerates" toward the boundary separating different self-action regimes, intersects the boundary, and occurs in the defocusing region ($\rho < 0$), where it continues moving with the same acceleration.

Let us minimize action (6) on the class of probe functions (7) which are localized near the center of mass and have the form

$$u(\zeta, t) = \frac{u_0}{\sqrt{a}}\exp\Big(-\frac{(\zeta - \rho)^2}{2a^2} + i\phi(\zeta - \rho)^2\Big). \quad (10)$$

Substituting Eq. (10) into Eq. (6) and integrating with respect to $\zeta$, we obtain the reduced action and the equation of motion

$$\rho a_{zz} - a_z\rho_z = \frac{\rho^3}{a^3} - \frac{\rho^2 u_0^2}{4a^2 b}, \quad (11)$$

which describes the change in the characteristic size $a(z)$ of the region of wave-field localization during the course of system evolution.

Near the boundary where the dispersion changes sign ($\zeta \simeq 0$), the approximate solution to Eqs. (9) and (11) with $H < 0$ has the form

$$\rho \approx 2(\rho_0|H|/I)^{1/2}(z_0 - z), \quad (12)$$

$$a \approx \frac{1}{8}\Big(\frac{u_0^2}{b}\Big)^{1/2}\Big(\frac{\rho_0}{a_0}\Big)^{1/6}(z_0 - z), \quad (13)$$

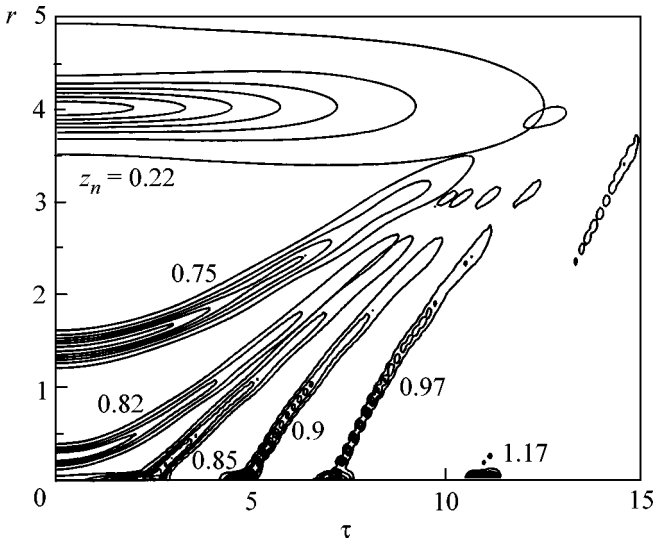


**Fig. 1.** Contour map of the $|\psi(r, \tau, z = z_n)|$ field for the indicated $z_n$ values. The evolution of the axisymmetric hollow beam along the propagation path $z$ for the dissipative collapse stabilization at $\delta = 2 \times 10^{-8}$.

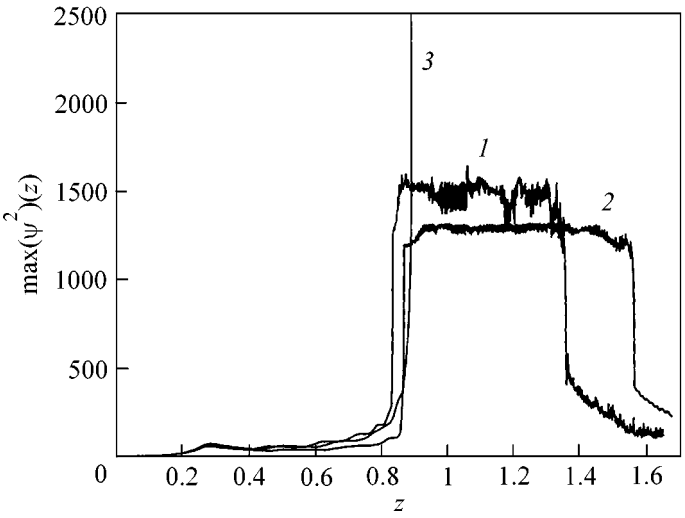


**Fig. 2.** The squared maximum field amplitude $|\psi|^2$ vs. $z$. Lines *1* and *2* correspond to the dissipative collapse stabilization at $\delta = 2 \times 10^{-8}$ and $1.8 \times 10^{-5}$, respectively. Line *3* describes the dynamics of a conservative system with nonlinearity-saturation field $\psi_s = 20$.

where $\rho_0$ is the initial position of the center of mass, and the evolution coordinate $z = z_0 = (\rho_0 I/|H|)^{1/2}$ corresponds to the intersection of the center of mass and the boundary $\zeta = 0$. Therefore, as the center of mass approaches the boundary separating two different self-action regimes (focusing changes to defocusing), the field amplitude tends to infinity as

$$\psi(\zeta \longrightarrow 0, z \longrightarrow z_0) \approx (z_0 - z)^{-1/2}. \qquad (14)$$

**2.** The self-action mechanism described above is confirmed by the numerical study of the dynamics of initial Gaussian distributions localized near the hyperbolas $r^2 - \tau^2 = a_r^2$. To study the collapse stabilization and the further evolution of the system, we used the generally accepted methods for regularizing initial Eq. (1). These methods are based on taking into account the saturation of nonlinearity or nonlinear radiation absorption in strong fields:

$$i\frac{\partial\psi}{\partial z} + \frac{1}{r}\frac{\partial}{\partial r}r\frac{\partial\psi}{\partial r} - \frac{\partial^2\psi}{\partial\tau^2} + \left(\frac{|\psi|^2}{1 + |\psi|^2/\psi_s^2} + i\delta|\psi|^8\right)\psi = 0, \qquad (15)$$

where $\psi_s$ is the nonlinearity saturation field and $\delta$ is the parameter of nonlinear dissipation. Using Eq. (15), we consider the evolution of the initial distribution of the form

$$\psi = \psi_0 r^4/a_r^5 \exp[-r^2/2a_r^2 - \tau^2/2a_\tau^2], \qquad (16)$$

which models the field structure of a tubular spatially-limited electromagnetic pulse. One can expect that distribution (16) at the initial stage of evolution should transform into the horseshoe distribution of type (7). This process can be treated as a bend instability of a uniform wave beam [9]. It is well known that the $\tau$-uniform tubular beams with a supercritical intensity are compressed in the transverse direction and self-focused toward the $\tau$ axis. Therefore, one can expect that the central part ($\tau \approx 0$) of the nonuniform (with respect to $\tau$) distribution (16) will be focused on the axis ($r = 0$) faster than its peripheral part ($\tau \sim a_\tau$).

Numerical calculations confirm this prediction. For definiteness, we first consider a nonconservative case using Eq. (15) with the saturation field $\psi_s \longrightarrow \infty$ and then present the additional results relating to the conservative collapse stabilization ($\delta = 0$). The calculations were carried out with the parameters $a_r = 2$ and $a_z = 12$.

Figure 1 shows the results of the numerical calculations. It can be seen that the wave-beam self-focusing without a change in the characteristic radius of the hollow field distribution (16) takes a rather long time. At the next stage, a horseshoe structure is formed, and this process is accompanied by the development of splitting instability. In contrast to the two-dimensional case [13, 14], this splitting is immaterial and stabilized by the shift of the horseshoe distribution to the system axis. In the course of the "fall-to-center" process, the pulse splits into two parts. The maximum field amplitude in the focal region remains virtually constant during a rather prolonged wave-field evolution (see Fig. 2). In this case, the strong-field regions travel distances far exceeding the pulse longitudinal length without a noticeable change in the spatial structure. The nonlin-

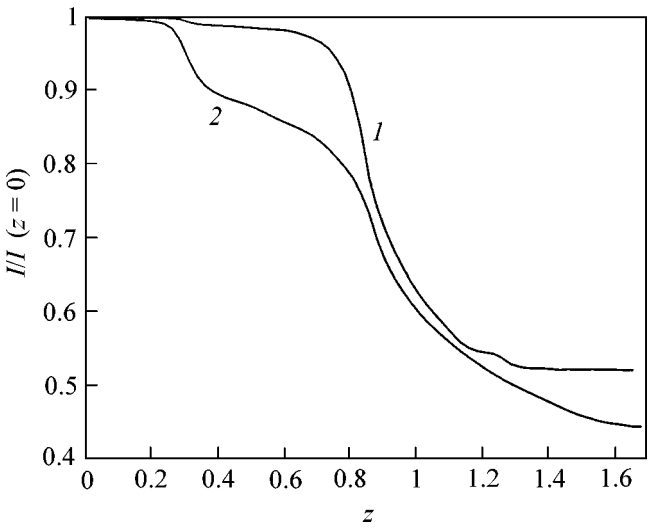


**Fig. 3.** Dissipation of wave-packet energy in the course of collapse. The parameters for lines *1* and *2* correspond to lines *1* and *2* in Fig. 2.

ear energy absorption for the packet passing through the collapse region (see Figs. 2, 3) is about 50%.

In the conservative case, the "fall-to-center" pattern is quite similar. The only difference is the appearance of reflection from the region of singularity formation. For the chosen parameters, the distribution of field amplitude has a sharp maximum on the axis, and the maximum value markedly exceeds the corresponding value in the dissipative case (see Fig. 2). The time it takes to form the strong-field region also somewhat increases (Fig. 2).

On the whole, the modeling suggests that the smearing of horseshoe distribution in the transverse direction has virtually no effect on the dynamics of singularity formation. However, it is clear that, in the fall-to-center regime, the peripheral wave-packet part reaches the system axis at a later time and maintains the intense field during the entire interaction time. In this sense, the type of collapse considered above should be assigned to the prolonged collapses.

We have considered a new scenario of the self-action dynamics of an axisymmetric wave packet in the system described by the nonlinear Schrödinger equation with a hyperbolic spatial operator. We have found the class of initial wave-field distributions whose evolution illustrates the specific features of Eq. (1). For these initial conditions, the self-focusing compression prevails over the dispersion wave-field smearing. The self-focusing narrows the tubular wave packets in the transverse direction, forms a horseshoe structure, shifts the wave field to the system axis, and, finally, creates a collapse regime (due to the cylindrical symmetry of the problem). This collapse is quite similar to the spherically symmetric process in the NSE with the elliptic spatial operator. The specificity of collapse is that the wave-packet splitting at the center of the system is accompanied by the formation of two strong-field regions ("hot" points) moving in the opposite directions.

The use of such traveling focuses hold much promise, e.g., for the creation of channels in condensed media and artificial photonic crystals with a view to the future application of these structures in the acceleration of charged particles and radiation frequency conversion.

This work was supported by the Russian Foundation for Basic Research, project nos. 02-02-17277 and 01-02-17388.

## REFERENCES

1. A. G. Litvak and V. I. Talanov, Izv. Vyssh. Uchebn. Zaved., Radiofiz. **10**, 539 (1967).
2. N. A. Zharova, A. G. Litvak, T. A. Petrova, *et al.*, Pis'ma Zh. Éksp. Teor. Fiz. **44**, 12 (1986) [JETP Lett. **44**, 13 (1986)]; N. A. Zharova, A. G. Litvak, T. A. Petrova, *et al.*, Izv. Vyssh. Uchebn. Zaved., Radiofiz. **29**, 1137 (1986).
3. J. E. Rothenberg, Opt. Lett. **17**, 583 (1992).
4. P. Chernev and V. Petrov, Opt. Lett. **17**, 172 (1992); Opt. Commun. **87**, 28 (1992).
5. G. G. Luther, A. C. Newell, and J. V. Moloney, Physica A (Amsterdam) **49**, 4085 (1994); G. G. Luther, A. C. Newell, J. V. Moloney, *et al.*, Opt. Lett. **19**, 789 (1994); **19**, 862 (1994).
6. J. E. Ranka, R. W. Schrimer, and A. L. Gaeta, Phys. Rev. Lett. **77**, 3783 (1996).
7. A. A. Zozulya *et al.*, Phys. Rev. Lett. **82**, 1430 (1999); A. A. Zozulya *et al.*, Phys. Rev. A **58**, 3303 (1998).
8. L. Berge and J. J. Rasmussen, Phys. Plasmas **3**, 824 (1996); L. Berge, J. J. Rasmussen, E. A. Kuznetsov, *et al.*, J. Opt. Soc. Am. B **20**, 1879 (1996); L. Berge, E. A. Kuznetsov, and J. J. Rasmussen, Phys. Rev. E **53**, R1340 (1996); G. Fibich, V. M. Malkin, and G. C. Papanicolaou, Phys. Rev. A **52**, 4218 (1995).
9. K. Germaschewski, R. Grauer, L. Berge, *et al.*, Physica D (Amsterdam) **151**, 175 (1991).
10. A. G. Litvak, T. A. Petrova, A. M. Sergeev, and A. D. Yunakovskiĭ, Fiz. Plazmy **9**, 495 (1983) [Sov. J. Plasma Phys. **9**, 287 (1983)]; A. G. Litvak, A. M. Sergeev, and N. A. Shakhova, Pis'ma Zh. Tekh. Fiz. **5**, 862 (1979) [Sov. Tech. Phys. Lett. **5**, 33 (1979)].
11. J. R. Myra and C. S. Liu, Phys. Fluids **23**, 2258 (1980).
12. A. G. Litvak, V. A. Mironov, and É. M. Sher, Zh. Éksp. Teor. Fiz. **118** (6), 1463 (2000) [JETP **91**, 1268 (2000)]; A. G. Litvak, V. A. Mironov, and E. V. Sher, Phys. Rev. E **61**, 891 (2000).
13. S. N. Vlasov, L. V. Piskunova, and V. I. Talanov, Zh. Éksp. Teor. Fiz. **95**, 1945 (1989) [Sov. Phys. JETP **68**, 1125 (1989)]; S. N. Vlasov, Izv. Vyssh. Uchebn. Zaved., Radiofiz. **42**, 468 (1999).
14. V. E. Zakharov, N. E. Kosmatov, and V. F. Shvets, Pis'ma Zh. Éksp. Teor. Fiz. **49**, 431 (1989) [JETP Lett. **49**, 492 (1989)]; V. M. Malkin, Pis'ma Zh. Éksp. Teor. Fiz. **48**, 603 (1988) [JETP Lett. **48**, 653 (1988)].

*Translated by R. Tyapaev*

JETP Letters, Vol. 75, No. 11, 2002, pp. 543–546. Translated from Pis'ma v Zhurnal Éksperimental'noĭ i Teoreticheskoĭ Fiziki, Vol. 75, No. 11, 2002, pp. 660–663.


# Parametric Reversal of Nonlinear Acoustic Waves

**A. P. Brysev*, V. G. Mikhalevich, and V. N. Strel'tsov**

*Wave Research Center, Institute of General Physics, Russian Academy of Sciences, Moscow, 119991 Russia*

** e-mail: brysev@orc.ru*

Received April 29, 2002

A mechanism of parametric reversal of the ultrasonic field from a quasi-monochromatic radiator situated in a nonlinear acoustic medium is proposed and analyzed. The mechanism is based on the phonon–plasmon interaction in semiconductors with a high concentration of electron traps, when a sample is irradiated by a periodic sequence of short laser pulses. The spectrum of output signal and, correspondingly, the temporal profile of the spatially reversed wave are investigated as functions of the intensity and duration of pumping pulses. It is shown that the choice of pumping parameters allows one to control the spectrum of reversed wave and, in particular, closely reproduce the spatiotemporal structure of the original wave. The frequency matching of the nonlinear ultrasonic wave harmonics and the pump Fourier frequencies occurs automatically at a certain pulse repetition rate in this scheme. © *2002 MAIK "Nauka/Interperiodica".*

PACS numbers: 43.25.Jh; 63.20.-e

The problem of the wave-phase conjugation (WPC) of ultrasonic beams is one of the topical problems of physical acoustics. The interaction of acoustic vibrations with the collective nonphonon modes in solids in external varying force fields is the most efficient mechanism of acoustic WPC [1]. An external field modulating the parameters of a labile nonacoustic subsystem induces the time modulation of the effective sound constants in a medium and, therefore, the generation of a reversed sound wave.

The supercritical WPC regime for a monochromatic ultrasonic wave in the presence of phonon–magnon interaction has now been experimentally realized for a magnetostriction ceramic in an alternating magnetic field with an amplification coefficient higher than 80 dB [1].

In the physically and practically interesting case of intense ultrasonic beam reversal, the reversed wave is substantially nonlinear, and the complete reversal, which is treated as the recovery of spatiotemporal distribution of the acoustic wave on a source, implies the synchronized WPC of all its harmonics that are formed upon the propagation of an incident wave through a nonlinear acoustic medium. In this respect, acoustics differs from optics, where the reversal problem amounts to the reversal of monochromatic waves.

At present, the WPC of nonlinear waves cannot be realized using multichannel analog–digital systems [2]. The use of parametric physical mechanisms for this purpose obviously requires coherent broadband modulating pump sources. For the pumping of a sample by a magnetic or electric field, the fabrication of such sources is difficult.

In this work, a mechanism of parametric reversal of the ultrasonic field from a quasi-monochromatic radiator situated in a nonlinear acoustic medium is proposed and analyzed. The mechanism is based on the phonon–plasmon interaction in semiconductors with a high concentration of electron traps when a sample is irradiated by a periodic sequence of short laser pulses. The spectrum of output signal and, correspondingly, the temporal profile of the spatially reversed wave are investigated as functions of the intensity and duration of the pumping pulses. It is shown that the appropriately chosen pumping parameters allow one to control the spectrum of reversed wave and, in particular, closely reproduce the spatiotemporal structure of the original wave. The frequency matching of the nonlinear ultrasonic wave harmonics and the WPC-pumping frequencies occurs automatically at a certain pulse repetition rate in the scheme considered.

In [3, 4], the WPC mechanism was proposed and studied in detail for monochromatic (with frequency $\omega$) ultrasonic beams in the presence of phonon–plasmon interaction in semiconductors in which the concentration of conduction electrons is modulated due to the irradiation by a sequence (with period $T = \pi/\omega$) of short (with duration $\tau_i$) laser pulses. For short relaxation times $\tau_{rel}$ corresponding to a high electron-trap concentration in the practically realizable conditions, this mechanism ensures the WPC of an intense acoustic wave, with initial frequency $\omega$ propagating in a medium with ordinary acoustic nonlinearity.

Let a nonlinear transverse acoustic wave with frequency $\omega$ and displacement

$$U^+(0) = \sum U_S^+(0)\exp(is\omega t)$$

0021-3640/02/7511-0543$22.00 

be incident onto the entrance of a plane-parallel semiconductor WPC layer with thickness $l$.[1] We assume that the phonon–electron coupling is due to the piezoelectric effect and the transformation coefficient of acoustic harmonics in the system with intrinsic acoustic nonlinearity is smaller than the coefficient of parametric transformation. Then, for the semiconductor crystal structure and the propagation geometry accepted in [4], the complete set of equations for the acoustic displacement $U$, density $n$ of electron oscillations in a Langmuir wave (assuming that $m_e < m_p$, where $m_e$ and $m_p$ are the effective masses of electrons and holes, respectively, we ignore the hole component in plasma), internal electric field $E$, and electron velocity $V$ has the form

$$\frac{\partial N}{\partial t} + \frac{N - n_0}{\tau_{\text{rel}}} = \gamma I(t); \quad \frac{\partial n}{\partial t} + \frac{n}{r_{\text{rel}}} + N\frac{\partial V}{\partial z} = 0;$$
$$\frac{\partial V}{\partial t} + \nu V = -\frac{e}{m_e}E; \qquad (1)$$
$$\rho\frac{\partial^2 U}{\partial t^2} = C\frac{\partial^2 U}{\partial z^2} - \bar{e}\frac{\partial E}{\partial z}; \quad \varepsilon\frac{\partial E}{\partial z} + \bar{e}\frac{\partial^2 U}{\partial z^2} = -4\pi en.$$

Here, $\rho$ is the semiconductor density; $C$, $\bar{e}$, and $\varepsilon$ are the elastic modulus, piezoelectric modulus, and dielectric constant of the sample, respectively; $\nu$ is the electron scattering frequency; $N$ is the equilibrium electron density in the conduction band in an external laser field with intensity $I(t)$; $\gamma$ is the coefficient of light absorption; and $n_0$ is the dark electron density.

According to the above, $I(t)$ can be expanded in the Fourier series:

$$I(t) = I_0 + \sum_{s\neq 0} I_s e^{2is\omega t}.$$

In the one-dimensional approximation and the steady-state regime, the total acoustic field in the medium is obtained from Eqs. (1) as

$$U = 0.5\left[\sum_s U_s^+(z)\exp[-is(\omega t - kz)] + \sum_s U_s^-(z)\exp[-is(\omega t + kz)] + \text{c.c.}\right].$$

Here, $U(z)$ are slowly changing amplitudes; $\omega = kV_s$, where $V_s$ is the speed of sound in the medium; and $k$ is the wave number. Then, similar to [3, 4], we obtain the following system of independent pair equations for the components $U_s^+$ under $\omega\tau_{\text{rel}} < 1$ and $n_0 < N$:

$$\frac{dU_s^{+*}}{d\bar{z}} = -isq(I_s/I_0)^2\frac{1}{(\varepsilon+q)^2 - q^2(I_s/I_0)^4}U_s^-,$$
$$\frac{dU_s^-}{d\bar{z}} = -isq(I_s/I_0)^2\frac{1}{(\varepsilon+q)^2 - q^2(I_s/I_0)^4}U_s^{+*}. \qquad (2)$$

Here, $q = \omega_{p0}^2\tau_{\text{rel}}/\nu$, where $\omega_{p0}^2 = 4\pi e^2\gamma\tau_{\text{rel}}I_0/m_e$ is the plasma frequency determined by the constant component of $I(t)$, and

$$\bar{z} = z\frac{4\pi\bar{e}^2k}{2\rho V_s^2}$$

is the dimensionless variable. By solving Eqs. (2), one obtains the output component $U_s^-(0)$ of the acoustic-field amplitude in the general form

$$U_s^-(0) = -iU_s^{+*}(0)\tan\left[\frac{sq(I_s/I_0)^2}{(\varepsilon+q)^2 - q^2(I_s/I_0)^4}L\right],$$

where $L$ is the dimensionless thickness of the WPC layer. Thus, $U_s^-$ is conjugate to the input component $U_s^+$, signifying the spatial reversal (WPC) of the component, and the transformation coefficient is determined by the pumping intensity ($q$ value) and the ratios of its Fourier amplitudes. The phase matching of the reversed-wave components corresponds to their matching in the incident wave.

Let us discuss two most interesting cases that demonstrate the general regularities of the process.

(i) Meander pumping:

$$\frac{I_s}{I_0} = \frac{1}{s}\frac{\sin(s\omega\tau_i)}{\omega\tau_i}.$$

It is easy to see that, for sufficiently short pumping pulses such that $N_{\text{eff}}\omega\tau_i < 1$, where $N_{\text{eff}}$ is the effective number of harmonics in the input ultrasonic wave, and for moderate pumping levels, $q \leq \varepsilon$, we have

$$U_s^-(0) = -iU_s^{+*}(0)\tan(sL/3\varepsilon).$$

Figure 1 shows the normalized temporal profiles of the input and output reversed waves for $q \approx \varepsilon$ and various $\omega\tau_i$ values. The Fourier components $U_s(0)$ are approximated by the conventional Bessel–Fubini distribution. Figure 1a demonstrates that an increase in the transformation coefficient with frequency leads to an increase in the relative contribution of higher harmonics. For this reason, the reversed wave is distorted stronger than the incident wave. An increase in the laser pulse duration at a constant pumping level $q \approx \varepsilon$ leads to a decrease in the transformation coefficient of amplitude

[1] It is assumed that the discontinuity in the wave does not appear.

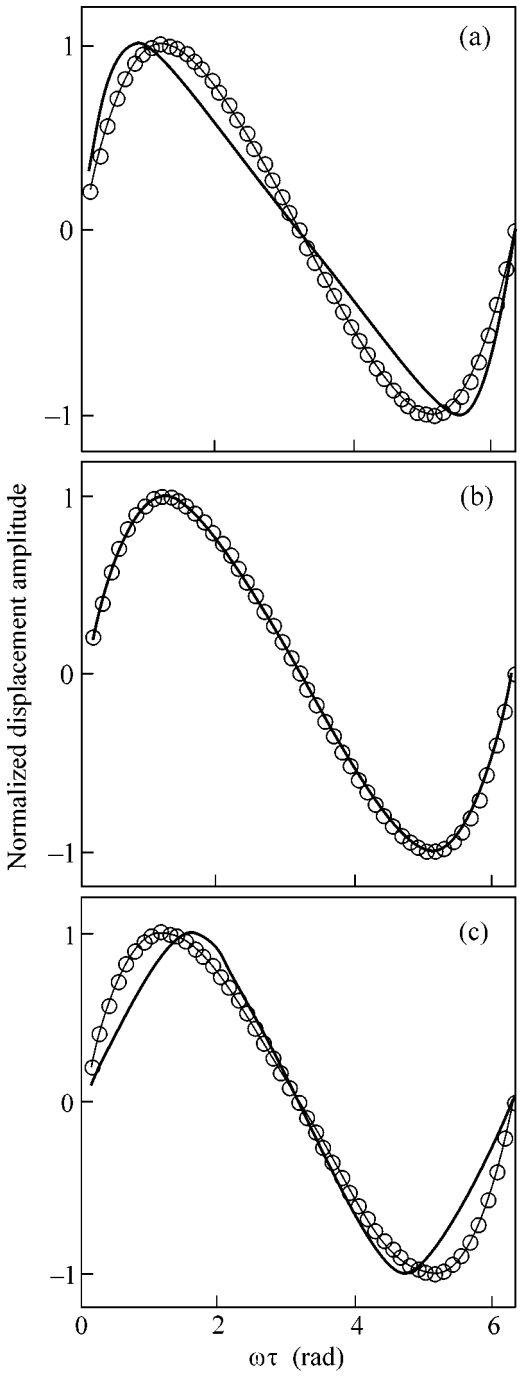


**Fig. 1.** Normalized temporal profiles of the (line with circles) incident wave and (solid line) reversed wave upon pumping by a sequence of meander laser pulses ($q \approx \varepsilon$) for (a) $\omega\tau_i \ll 1$, (b) $\omega\tau_i = 0.9$, and (c) $\omega\tau_i \approx \pi/2$.

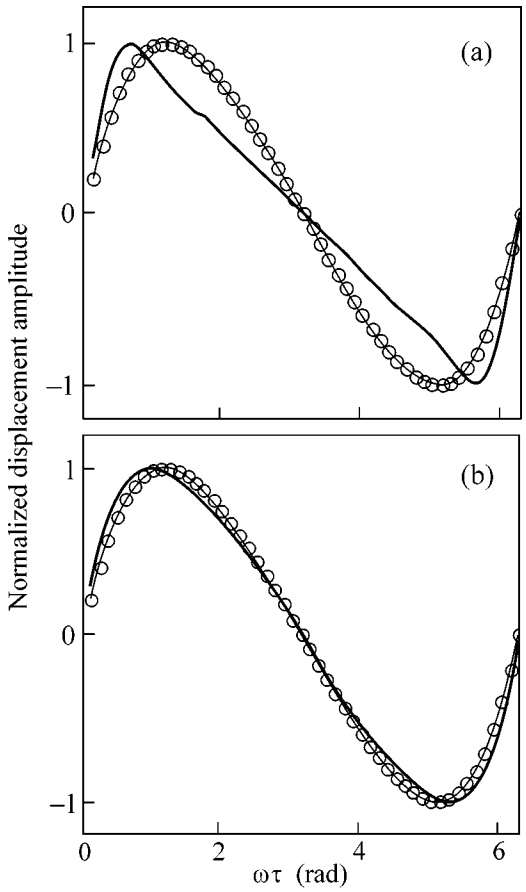


**Fig. 2.** The same as in Fig. 1 but for pumping by the pulses formed upon laser mode locking with frequency shift 2ω for (a) $q \approx \varepsilon/2$ and $N/2N_L = 1$ and (b) $q \gg \varepsilon/2$ and $N/2N_L = 0.33$.

$U_s$ for higher harmonics and, therefore, to the equalization of the transformation coefficients of acoustic harmonics and the ensuing rise in the degree of reproducing the spatiotemporal profile of the incident wave (see Fig. 1b). A complete reproduction, with allowance for the nonlinear wave transformation upon the back passage, evidently corresponds to a value of ~1 for the coefficient of harmonic transformation, which is controlled by the length of active transformation zone at a given pumping level. Figure 1c corresponds to the case where $\omega\tau_i \approx \pi/2$ and only even harmonics are transformed, leading to the wave-profile deformation shown in the figure.

Note that for the layer thickness $l \sim 0.3$ cm, $q \approx \varepsilon \approx 10$, $\tau_{rel} \sim 10^{-9}$ s, $\omega \sim 10^8$ rad, light absorption coefficient $\gamma \sim 10^1$ cm$^{-1}$, and typical values of the remaining semiconductor parameters apply; 100% conversion of the incident wave into the reversed wave is achieved for the pump intensity $I \sim 10$ W/cm$^2$.

(ii) Pumping by pulses formed upon laser mode locking with frequency shift 2ω. If the amplitudes and phases are the same for different locked modes, then

$$I(t) = I_L\left[\sum_{s=0}^{2N_L}(2N_L - s)\exp(2is\omega t) + \sum_{s=-1}^{-2N_L}(2N_L + s)\exp(2is\omega t)\right],$$

where $N_L$ is the number of locked modes and $I_L = |E_s|^2$. One then has for the components of reversed wave

$$U_s^-(0) = -iU_s^{+*}(0)\tan\left[\frac{sq(1-s/2N_L)^2}{(\varepsilon+q)^2 - q^2(1-s/2N_L)^4}L\right].$$

Figure 2a shows the input and output profiles of the reversed and incident waves, respectively, for $q \approx \varepsilon/2$ and $N_{\text{eff}}/2N_L \approx 1$. In the opposite case of intense pumping, i.e., for $q \gg \varepsilon/2$, the transformation has the form shown in Fig. 2b, where the temporal profile of the incident wave is well reproduced.

In conclusion, we note that the suggested mechanism of nonlinear wave reversal allows the efficient control of the spectral structure of an acoustic beam by self-focusing on a source, which is of interest for various applications, particularly at the powerful acoustic action. The desired incident harmonics can be selectively reversed by appropriately choosing the repetition rate of laser pulses. The physical pattern of the phenomenon will obviously be retained in the supercritical reversal regime as well.

This work was supported by the U.S. Civilian Research and Development Foundation for the Independent States of the Former Soviet Union (grant no. RP2-2367-MO-02), the Russian Foundation for Basic Research (project nos. 00-15-96636, 01-02-16242, and 02-02-16916), and the Russian–French program PAI-RUSSIER (grant no. 04585TK).

## REFERENCES

1. A. P. Brysev, L. M. Krutyanskiĭ, and V. L. Preobrazhenskiĭ, Usp. Fiz. Nauk **168**, 877 (1998) [Phys. Usp. **41**, 793 (1998)].
2. M. Tanter, J.-L. Thomas, F. Coulouvrat, *et al.*, Phys. Rev. E **64**, 016602 (2001).
3. V. N. Strel'tsov, Kvantovaya Élektron. (Moscow) **13**, 2144 (1986).
4. A. P. Brysev and V. N. Strel'tsov, Akust. Zh. **32**, 564 (1986) [Sov. Phys. Acoust. **32**, 358 (1986)].

*Translated by R. Tyapaev*

*JETP Letters, Vol. 75, No. 11, 2002, pp. 547–551. Translated from Pis'ma v Zhurnal Éksperimental'noĭ i Teoreticheskoĭ Fiziki, Vol. 75, No. 11, 2002, pp. 664–668.*


# Statistics of Long-Wavelength Fluctuations and the Expansion Rate of Richtmyer–Meshkov Turbulence Zone

**N. A. Inogamov**

*Landau Institute for Theoretical Physics, Russian Academy of Sciences, ul. Kosygina 2, Moscow, 117334 Russia*

Received April 22, 2002

The important problem of Richtmyer–Meshkov turbulence (RMT) is solved. Much work has been devoted to the experimental, numerical (direct numerical simulation), and semiphenomenological (turbulent diffusion and bubble envelope models) analysis of RMT. All of them were of approximate character. They considered the evolution of a mixing layer, and its average thickness $h(t)$ was found. Then, the approximate value of the most important exponent $\theta$ ($h \propto t^{\theta}$) was judged from the slope of the $h(t)$ curve in the ln$t$–ln$h$ coordinates. In this work, the theoretical approach for the exact determination of $\theta$ is developed. *© 2002 MAIK "Nauka/Interperiodica".*

PACS numbers: 47.20.Ma; 47.27.Cn

**1. Current status.** The necessity of studying turbulent mixing arises in many physical problems (astrophysics, physics of explosion, inertial nuclear fusion, convection, etc.) [1–5]. Mixing is caused by the Richtmyer–Meshkov (RM), Rayleigh–Taylor (RT), and Kelvin–Helmholtz (KH) instabilities. In the case of RM turbulence (RMT), the mixing front at the self-similarity stage moves in a heavy liquid following the law $h_+ = [\alpha_+^{RT}/(1+\mu)]g_A t^{\theta^{RT}}$, where $\theta^{RT} = 2$, $\mu = \rho_l/\rho_h < 1$ is the density ratio, $g_A = (1-\mu)g$ is the Archimedes acceleration, and $\alpha_+^{RT} \approx 0.05$ [1–5]. The surface $z = h_+(t)$ bounds the mixing layer from above. In the case of KH turbulence and $\mu = 1$, the mixed layer is bounded by the fronts $h_\pm = \pm\alpha_+^{KH} u t^{\theta^{KH}}$, where $\theta^{KH} = 1$, $u$ is the difference in liquid velocities, and $\alpha_+^{KH} \approx 0.07$ [6, 7]. In the case of RMT, the mixing front $z = h_+(t)$ asymptotically extends in a heavy liquid following the power law

$$h_+ \propto t^{\theta_+^{RM}} \tag{1}$$

with exponent $\theta_+^{RM}$. This exponent is the most important quantitative RMT characteristic.

It is deemed that RM turbulence is more complex than RT and KH turbulences. In the RT and KH cases, a "simple" inversion cascade occurs [1–5]. A clear understanding of the reasons underlying the enlargement cascade follows from the triad of (i) random periodic large-scale structures, (ii) subharmonic instability (or periodicity instability), and (iii) enlargement sequence [4, 5]. The exponents $\theta^{RT}$ and $\theta^{KH}$ can easily be found from dimensionality considerations ($gt^2$ and $ut$ are proportional to the length). The coefficients $\alpha_+^{RT}$ and $\alpha_+^{KH}$ cannot be calculated analytically. They are to be approximately determined from the experiment. These coefficients depend on a combination of the complex nonlinear, statistical, and dissipative processes.

The current general point of view on RM mixing is as follows. It is thought that the exponent $\theta_+^{RM}$, similar to the coefficients $\alpha_+^{RT}$ and $\alpha_+^{KH}$, cannot be calculated analytically. The "energetic" consideration is conjectured, according to which the relationship

$$\alpha_+^{RM} = 2/3 - \Delta\theta_{\text{diss}} \tag{2}$$

is fulfilled. The exponent 2/3 appears due to the energy conservation [3, 8–14] ($E = \rho v^2 h/2 \sim \rho h^3/t^2$; hence, $h \propto t^{2/3}$). This exponent is derived from energy balance considerations in the problem of a powerful explosion at a flat boundary between two gases with different densities $\rho_l$ and $\rho_h$ [15]. Of interest is how the asymptotic behavior in the problem of a powerful explosion transforms at $\mu \longrightarrow 0$ to the asymptotic expression in the short impact problem [16]. The "shift" $\Delta\theta_{\text{diss}} > 0$ is usually related to the energy loss caused by the small-scale (e.g., Kolmogorov) dissipation [10, 12, 13].

Thus, the quantities $\alpha_+^{RT}$, $\alpha_+^{KH}$, and $\theta_+^{RM}$ are the fundamental quantitative characteristics of RT, KH, and RM mixing, respectively. Much work is under way to refine these quantities (see, e.g., bibliography in the review section of [14]). With RMT, (i) the theoretical estimate gives $\theta_+^{RM} = 2/7$ [17, 9, 18]; (ii) the empirical

model of turbulent diffusion gives $\theta_+^{RM} \approx 0.315$ and 0.295 [9]; (iii) the empirical model of a bubble chain or envelope gives $\theta_+^{RM} \approx 0.40$ [19]; (iv) the experiment [3, 14] gives $\theta_+^{RM} = 0.25 \pm 0.05$; and (v) direct numerical simulation [10] gives (with some stipulations; see [10], p. 737) $\theta_+^{RM} \approx 0.30$. One can see that the scatter is rather broad. The role of geometry (2D or 3D) remains to be clarified. Equation (2) relating the desired exponent to the heat release on the short-wavelength viscous scale remains the ideological basis of the investigation.

Below, an alternative theory is proposed. The exponent is determined rigorously. The expansion of the turbulence zone is accompanied by the enlargement of the dominant structure. The expansion dynamics follows from the law of impulse generation due to the long-wavelength fluctuations. Their amplitude is determined statistically. It is found that the layer expansion is due to the statistics of the long-wavelength harmonics rather than the short-wavelength viscous friction. The exponents $\theta_+^{RM}$ for the 2D and 3D cases are different.

**2. Short-scale perturbations and impulsive acceleration.** RM instability develops after the passage of a shock wave (SW) through the perturbed boundary $\eta$ between two contacting gases [3–5, 9–14, 18–24]. Before the interaction with the boundary, the SW plane is parallel to the $z = 0$ plane. The unperturbed boundary is the straight line $z = \eta_{\text{unpert}}(x) \equiv 0$ (2D) or the plane $z = \eta_{\text{unpert}}(x, y) \equiv 0$ (3D). Let, for definiteness, the heavy gas be situated "atop" at $z > \eta$. Before SW, the substances are at rest. The perturbed boundary before SW is a wavy curve $\eta_{2D} = \eta(x)$ (2D) or wavy surface $\eta_{3D} = \eta(x, y)$ (3D).

**2.1. Random periodic curves and surfaces.** The initial perturbation has the characteristic scale $\lambda_0$ in the $z = 0$ plane and is a random periodic function (RPF). One should "start" with the initial data that are (i) random and (ii) "localized" in the wavenumber space (the scale does not exceed a certain value, i.e., has no additional long-wavelength perturbations). The goal is to study the evolution up to large times $t \gg t_0 = \lambda_0/w_0$, where $w_0$ is the characteristic velocity on the $\lambda_0$ scale after the passage of SW. At these times, the desired power-law regime (1) prevails. The spectral and statistical properties of the 2D RPF $\eta_{2D}$ are described in [4, 5, 25]. In the 3D case, the "relief" $\eta_{3D}$ is a random "lattice" (chain in 2D) of "hills" and "pits," with $\bar{\eta}_{3D} = (2\pi)^{-2}\int_0^{2\pi}\int_0^{2\pi}\eta_{3D}dxdy = 0$. Let the functions $\eta_{2D}$ and $\eta_{3D}$ be specified in "boxes" of width $2\pi$ with periodic continuations on both sides. Clearly, $\lambda_0 \ll 2\pi$ (there are many hills in the box).

Let $l_i$ be the distance from the top of the $i$th hill to the nearest top. Index $i$ runs over all tops. Consider the $l_i$ statistics. One has $\bar{l}_i \sim \lambda_0$ for the mean and $\sqrt{\overline{(l_i - \bar{l}_i)^2}} \sim \lambda_0$ for the standard deviation. Hence, the random is on the order of mean. That is why these functions are called random periodic functions.

**2.2. Spectral representation.** Let us study the spectra of the RPFs $\eta_{2D}$ and $\eta_{3D}$. One has

$$\eta_{2D} = \sum_n (\eta_n^{(1)} C_{nx} + \eta_n^{(2)} S_{nx}),$$
$$\eta_n^{(1)} = \frac{1}{\pi}\int_0^{2\pi} \eta_{2D} C_{nx} dx, \ \ldots, \ C_{nx} = \cos nx, \tag{3}$$

$$\eta_{3D} = \sum_n \sum_m (\eta_{nm}^{(1)} C_{nx} C_{my} + \eta_{nm}^{(2)} C_{nx} S_{my} + \eta_{nm}^{(3)} S_{nx} C_{my} + \eta_{nm}^{(4)} S_{nx} S_{my}), \tag{4}$$

$$\eta_{nm}^{(1)} = \frac{1}{\pi^2}\int_0^{2\pi}\int_0^{2\pi} \eta_{3D} C_{nx} C_{my} dxdy,$$
$$\eta_{nm}^{(2)} = \frac{1}{\pi^2}\int_0^{2\pi}\int_0^{2\pi} \eta_{3D} C_{nx} S_{my} \ldots. \tag{5}$$

The wavenumber $n_0 = 2\pi/\lambda_0$ corresponds to the length $\lambda_0$. In the 2D (3D) case, there are $\sim n_0 \gg 1$ ($\sim n_0^2 \gg 1$) hills on the interval $2\pi$ (in the square $2\pi \times 2\pi$).

Consider the long-wavelength asymptotic behavior of spectra (3)–(5), $n \ll n_0$. Let us divide the integrals $\eta_n^{(1, 2)}$ over the interval $2\pi$ in Eq. (3) and the integrals $\eta_{nm}^{(1, 2, 3, 4)}$ over the square $2\pi \times 2\pi$ in Eq. (5) into the sums of integrals over halfwaves. The wavelengths of harmonics $n$, $m$ are, respectively, $\lambda_n = 2\pi/n$ and $\lambda_m = 2\pi/m$. Consider, for example, the Fourier amplitude $\eta_n^{(2)}$. Let us divide the interval $[0, 2\pi]$ into subintervals by points $x_i = \lambda_n i/2$, $i = 0, 1, \ldots, 2n$, $x_{2n} = l_n n = 2\pi$. Write

$$\eta_n^{(2)} = \frac{1}{\pi}\int_0^{2\pi} \eta_{2D}(x) S_{nx} dx$$
$$= \frac{1}{\pi}\sum_{j=0}^{n-1}\int_{x_{2j}}^{x_{2j+1}} \ldots + \frac{1}{\pi}\sum_{j=0}^{n-1}\int_{x_{2j+1}}^{x_{2j+2}} \ldots. \tag{6}$$

In Eq. (6), the first sum comes from the positive halfwaves of the function $\sin nx$, and the second sum comes from the negative halfwaves. In the 3D case, the square $2\pi \times 2\pi$ is divided into small squares corresponding to the positive and negative sections of the functions $C_{nx}C_{my}$, $C_{nx}S_{my}$, $S_{nx}C_{my}$, and $S_{nx}S_{my}$.

The terms in the sums in Eq. (6) correspond to the halfwaves $\lambda_n/2$. Each halfwave involves many hills and pits of the RPF $\eta_{2D}(x)$, because $\lambda_n \gg \lambda_0$. The average of the individual term $I = \int_{\lambda_n/2} \dots$ over the halfwave is zero. Due to the stochastic behavior of the RPF, $I$ fluctuates about its mean with the standard deviation

$$\sqrt{\overline{I^2}} \sim \sqrt{\lambda_n/\lambda_0}(1/\pi)(\bar{\eta}_{2D}\lambda_0),$$
$$\bar{\eta}_{2D} = \sqrt{(2\pi)^{-1}\int_0^{2\pi}[\eta_{2D}(x)]^2 dx}, \quad (7)$$

where $\eta_{2D}$ is the standard deviation of the function $\bar{\eta}_{2D}$, and the multiplier $\bar{\eta}_{2D}\lambda_0$ gives the estimate of the integral $\left|\int_{\lambda_0}\eta_{2D}dx\right|$ for a single hill/pit pair.

The mean amplitude of sum (6) is zero. The standard deviation of the sum (6) of random terms $I$ (7) is equal to

$$\sqrt{\overline{(\eta_n^{(2)})^2}} \sim \sqrt{\frac{2\pi}{\lambda_n}}\sqrt{\frac{\lambda_n}{\lambda_0}}\frac{1}{\pi}(\bar{\eta}_{2D}\lambda_0)$$
$$= \sqrt{\frac{2\pi}{\lambda_0}}\bar{\eta}_{2D}\frac{\lambda_0}{\pi} \sim \frac{\bar{\eta}_{2D}}{\sqrt{n_0}}. \quad (8)$$

The factor $\sqrt{2\pi/\lambda_n}$ in Eq. (8) appears as a result of adding together the random terms (7). One can see that the wavelength $\lambda_n$ in Eq. (8) cancels out, so that the $n$ dependence vanishes. Similarly, the mean amplitude of $\eta_{nm}^{(1,2,3,4)}$ (5) in the 3D geometry is zero. The standard deviation for the fluctuations of these amplitudes is independent of the numbers $n$ and $m$ and equal to

$$\sqrt{\overline{(\eta_{nm}^{(1,2,3,4)})^2}} \sim \sqrt{\frac{(2\pi)^2}{\lambda_N^2}}\sqrt{\frac{\lambda_N^2}{\lambda_0^2}}\frac{1}{\pi^2}(\bar{\eta}_{3D}\lambda_0^2) \sim \frac{\bar{\eta}_{3D}}{n_0}, \quad (9)$$
$$N = N_{nm} = \sqrt{n^2+m^2}.$$

One can show that the amplitudes $\eta_n$ or $\eta_{nm}$ of the neighboring harmonics $n$ and $n+1$ or $n$, $m$ and $n$, $m+1$ fluctuate independently. This indicates that the phases of these harmonics do not correlate.

**2.3. Shock, setting in motion, and the Richtmyer formula.** Let us consider the interesting case of small perturbations ($|(d/dx)\eta_{2D}| \ll 1$, $|(\eta_{3D})_x|$, $|(\eta_{3D})_y| \ll 1$), where the Richtmyer formula applies,

$$w_n = F\mathrm{At}n\eta_n w_{sw},$$
$$w_{nm} = F\mathrm{At}N_{nm}\eta_{nm}w_{sw}, \quad (10)$$
$$\mathrm{At} = \frac{1-\mu}{1+\mu},$$

In Eq. (10), $w_{sw}$ is the velocity of the unperturbed boundary behind the SW; $\eta_n$ and $\eta_{nm}$ are the amplitudes of boundary perturbation harmonics behind the SW; At is the Atwood number behind the SW; and $F$ is the coefficient depending, in the case of ideal gases, on their adiabatic exponents, the ratio of their sound velocities, and on the Mach number of the incident SW (in the incompressible case, $F = 1$). In the chosen system of coordinates $x$, $y$, $z$ and velocities $u$, $v$, $w$, the horizontal velocities are $u$, $v$ and the vertical velocity is $w$. Much work (see, e.g., [26] and reviews [4, 5]) has been devoted to the linear theory of RM instability in a compressible medium. The main purpose of those studies was to determine the function $F$.

The SW "converts" harmonics $\eta_n$ into harmonics $w_n$. A short (compared to the RMT development time) process of boundary acceleration upon its crossing by the SW ("shock") leaves a vortex "wake" at the boundary [4, 5, 23, 24], which affects the near-surface velocity field. Equation (10) gives a linear relationship between harmonics $\eta_n$ and $w_n$. An important point is that the coefficient $F$ is uniform in scales (independent of $n$). The initial velocity spectrum can be found from Eq. (10) and from what was said in section 2.2. It determines the subsequent evolution. It turns out that, in the most important long-wavelength region of the spectrum $0 < n < \sim n_0$, the amplitudes $w_n$ ($w_{nm}$) are linear in the wavenumber $n$ ($N_{nm}$) and the phases of the harmonics are random.

**2.4. Velocity field "grid" in the depth and power-law velocity decrease on moving away from the boundary.** It is known [4, 5] that, for small angles ($|\eta_x| \ll 1$), the compressibility can be ignored after the substance starts to move. The point is that, due to the factor $n\eta_n$, the velocities in Eq. (10) are smaller than the sound velocity ($c_s \sim w_{sw}$). Consequently, one can use the approximation of incompressible liquid. In addition, the vorticity is concentrated at the boundary, because, in the linear approximation in perturbations $\eta$, the SW cannot create vorticity in the bulk. When determining the initial velocity field, the boundary can approximately be considered flat. Under these assumptions, the potential can easily be found from the Laplace equation $\Delta\varphi = 0$ and the vertical velocity $w(x, y, z = 0, t = 0)$ at the boundary. All velocity components and the dependence of velocity on the vertical coordinate $z$, e.g., $w(x, y, z, t = 0)$, can subsequently be determined. One has

$$w(x, y, z, 0)$$
$$= \sum_n\sum_m (w_{nm}^{(1)}C_{nx}C_{my} + w_{nm}^{(2)}C_{nx}S_{my} + \dots)\exp(-N_{nm}|z|). \quad (11)$$

At $m = 0$, one arrives at the 2D formula. Because of the ellipticity of the Laplacian, the velocity of the harmonic with wavelength $\lambda$ exponentially decreases at depth $\sim\lambda$.

Let us consider the dependence of velocity (11) on the $z$ coordinate. At the distance $z^*$ from the boundary,

the harmonics with wavelengths $\lambda^* \sim z^*$, $n^* = 2\pi/\lambda^*$ dominate. Indeed, the small-scale ($n \gg n^*$) harmonics decay exponentially, while the large-scale harmonics, as will be seen below, have small amplitudes. For this reason, to determine the velocity $w^* = w(x, y, z^*, 0)$, it is necessary to sum out in Eq. (11) a portion corresponding to the numbers $n_{lw} < n < n_{sw}$, where $n_{lw} = n^*/q$, $n_{sw} = n^*q$, and $q \sim 1$; for instance, $q = 2$. An important fact is that the phases of the neighboring terms are random. One has $\overline{w^*} = 0$,

$$\sqrt{\overline{(w^*)^2}} \sim \sqrt{n^*} w_{n^*} \sim (n^*)^{3/2} w_{n0}/n_0 \sim (\lambda_0/\lambda^*)^{3/2} w_0 \sim w_0 \lambda_0^{3/2}/(z^*)^{3/2}, \quad (12)$$

$$\sqrt{\overline{(w^*)^2}} \sim N^* w(n^*, m^*) \sim (N^*)^2 w(n_0, m_0)/N_0 \sim (\lambda_0/\lambda^*)^2 w_0 \sim w_0 \lambda_0^2/(z^*)^2. \quad (13)$$

Equations (12) and (13) correspond to the 2D and 3D cases, respectively; $w(n, m) \equiv w_{nm}$. These equations involve the amplitude $w_n$ of the $n$th harmonic, the amplitude $w_{n0}$ of the $n_0$th harmonic, and the velocity $w_0$ of the $\lambda_0$-scale perturbations.

When deriving these formulas, (i) Eq. (10) was used to express the amplitude $w_{n^*}$ through the amplitude $\eta_{n^*}$; (ii) $\eta_{n^*} \sim \eta_{n0}$ were taken from Eqs. (8) and (9); (iii) Eq. (10) was used to return from $\eta_{n0}$ to $w_{n0}$; (iv) the amplitude $w_{n0}$ was expressed through the standard deviation of velocities $w_0$ on the scale $\lambda_0$, and the wavenumbers $n^*$ and $n_0$ were replaced by the wavelengths; and (v) the relation $\lambda^* \sim z^*$ was used.

One can see that, due to the long-wavelength statistics, the velocity fluctuations slowly decrease following the power law (rather than exponentially fast on the scale $\sim\lambda_0$) upon moving away from the boundary.

**2.5. Grid enlargement and inversion cascade.** The statistics of velocity (11) is given by Eqs. (12) and (13). Let us consider the alternation of the domains where the function $w(x, y, z, 0)$ is either positive or negative. One can see that these domains are meshes with size $\sim z$ along the vertical and horizontal axes. The mesh size increases with increasing $z$. The curve (2D) or the surface (3D), where the velocity changes sign, form a grid with enlarging meshes. It is formed in the course of a short SW-induced acceleration of the randomly perturbed boundary.

Let us determine the exponent $\theta_+^{RM}$. The mixing layer expands according to the velocity field (11). According to Eqs. (12) and (13), the passage through the mesh $z^*$ takes time $t^* \sim z^*/w^* \sim (z^*)^{5/2}$ in 2D and $\sim(z^*)^3$ in 3D. For this reason, small meshes are exhausted first, after which the successively larger meshes disappear. This is the inversion cascade. For the expansion velocity, one has $dh_+/dt \sim w \sim w_0\lambda_0^{3/2}/z^{3/2} \sim w_0\lambda_0^{3/2}/h_+^{3/2}$ in 2D and $dh_+/dt \sim w_0\lambda_0^2/h_+^2$ in 3D. This brings about formulas

$$h_+ \sim \lambda_0^{3/5}(w_0 t)^{2/5}, \quad \theta_+^{RM} = 2/5; \qquad h_+ \sim \lambda_0^{2/3}(w_0 t)^{1/3}, \quad \theta_+^{RM} = 1/3, \quad (14)$$

for the 2D and 3D cases, respectively.

**3. Mixing of the vorticity random distribution.** Above, the RMT behind the SW front was studied. It arises in shock tubes [10, 20–24, 26] or upon impulsive acceleration of the incompressible liquid (incompressible RM instability or impulsive RT instability) [3, 9–14, 19, 27]. It is difficult to calculate numerically the asymptotic behavior of RMT (to determine $\theta_+^{RM}$) in the statement with SW or impulsive acceleration. One has to track the fast SW together with the slow RMT. Moreover, the fast motion of the substance as a whole over the Euler grid [$w_0 \ll w_{sw}$ (10)] impedes the detailed resolution of the RM vortices (it is desirable to "subtract" $w_{sw}$). In the case of impulsive acceleration, a code is needed for the description of the incompressible liquid, whereas one ordinarily uses gas-dynamic codes.

In this connection, it seems reasonable to use gas-dynamic code for a small Mach number (see, e.g., [10, 25]) and with the initial near-surface velocity field created by the random vorticity distribution over the flat interface. We will show that the laws given by Eq. (14) hold for this formulation as well. They are determined by the long-wavelength wing of the pressure, acceleration, and impulse fluctuation spectra.

Let us consider the initial data. For the sake of brevity, we omit the expressions for the 2D and 3D potentials. The vertical velocity field is specified by the amplitudes $w_{nm}$ in Eq. (11) (the generalization to the 2D geometry is straightforward). It must be random and localized near the scale $\lambda_0 = 2\pi/n_0$ in the space of horizontal wavevectors. With these requirements, one obtains a long-wavelength "gap" $w_n = 0$ ($w_{nm} = 0$) for $n < n_0$ ($N_{nm} < n_0$) at $t = 0$. The harmonics $w_n$ ($w_{nm}$) with $n > n_0$ have random phases. The characteristic velocity is $w_0 \sim \sqrt{n_0} w_{n0}$ ($\sim n_0 w(n_0, m_0)$), where $w_{n0}$ is the average amplitude of harmonics with $n > n_0$ and $n \sim n_0$.

To elucidate the mechanism of generation of the long-wavelength fluctuations by means of bubble pressure, we consider the periodic case. In this case, the initial spectrum contains only a single harmonic $w_{n0}$ ($w(n_0, n_0)$). Let $\mu = 0$. Due to the development of RMT, a periodic chain (2D) or lattice (3D) of bubbles arises [4, 5, 27]. The pressures $p_\infty$ in the depth of the heavy liquid is different from the pressure at the boundary. Specifically, $p_{cb} < p_\infty$ and $\Delta p(t) = p_\infty - p_{cb} \sim \rho[w(t)]^2$, where $w$ is the velocity of bubble penetration into the heavy liquid [4, 5, 27]. At a certain distance from the bubble tops, the regions of positive and negative verti-

cal velocity have the form of vertical strips of width $\lambda_0/2$. The periodic case was taken to analyze pressure.

Let us return to the random array of 2D or 3D bubbles. The pressure $p(x, y, z^*, t)$ at the distance $z^*$ from the bubble tops varies along the horizontal coordinates. This is due to the statistical pressure fluctuations caused by the presence of the groups of dissimilar bubbles. One group contains about $z^*/\lambda_0$ (2D) or $\sim(z^*/\lambda_0)^2$ (3D) bubbles. The variability step is on the order of $z^*$. During the lifetime $t_0 \sim \lambda_0/w_0$ of a bubble with size $\lambda_0$, the pressure variability produces the spatially variable distribution of liquid impulses. The difference in the vertical velocities $w_\lambda$ in a mesh with size $\lambda \gg \lambda_0$ along the vertical and horizontal axes can be found from the force balance

$$(\rho w_0^2 \lambda_0)\sqrt{\lambda/\lambda_0}(\lambda_0/w_0) \sim \rho w_\lambda \lambda^2,\ w_\lambda \sim (\lambda_0/\lambda)^{3/2}, \quad (15)$$

$$\begin{gathered}(\rho w_0^2 \lambda_0^2)\sqrt{(\lambda/\lambda_0)^2}(\lambda_0/w_0) \sim \rho w_\lambda \lambda^3, \\ w_\lambda \sim (\lambda_0/\lambda)^2.\end{gathered} \quad (16)$$

In Eqs. (15) and (16), the quantity in the first parentheses is a force associated with one bubble; the root determines the amplitude of statistical fluctuations; and the quantity in the second parentheses is the time $t_0$. The right-hand side of the estimate is the mesh impulse $\lambda \times \lambda$ ($\lambda \times \lambda \times \lambda$) acquired during the acceleration time $t_0$.

One can see again (cf. 2.5) that a grid with enlarging meshes and power velocity-decay law is formed. At $t = 0$, the decay is exponential at the depth $\sim\lambda_0$ because of the initial long-wavelength gap. The gap ($t = 0$) is "blurred" in a time equal to the time $t_0$ of one vortex "rotation." By writing $dh_+/dt \sim w_\lambda$ and $h_+ \sim \lambda$, one again obtains the laws given by Eqs. (14).

This work was supported by the Russian Foundation for Basic Research, project no. 02-02-17499.

## REFERENCES


1. *Proceedings of the 2nd International Workshop Laboratory Astrophysics with Intense Lasers*, Astrophys. J., Suppl. Ser. **127** (2) (2000).
2. É. I. Asinovskiĭ, V. A. Zeĭgarnik, E. F. Lebedev, *et al.*, in *Pulse Magnetonydrodynamic Converters of Chemical Energy to Electric*, Ed. by A. E. Sheĭndlin and V. E. Fortov (Énergoatomizdat, Moscow, 1997).
3. G. Dimonte, Phys. Plasmas **7** (6), 2255 (2000).
4. N. A. Inogamov, A. Yu. Dem'yanov, and É. E. Son, *Hydrodynamics of Mixing* (Mosk. Fiz.-Tekh. Inst., Moscow, 1999).
5. N. A. Inogamov, Astrophys. Space Phys. Rev. **10** (2), 1 (1999).
6. F. K. Browand and B. O. Latigo, Phys. Fluids **22** (6), 1011 (1979).
7. L. D. Landau and E. M. Lifshitz, *Course of Theoretical Physics*, Vol. 6: *Fluid Mechanics* (Nauka, Moscow, 1986; Pergamon, New York, 1987).
8. G. I. Barenblatt, in *Nonlinear Dynamics and Turbulence*, Ed. by G. I. Barenblatt, G. Loos, and D. D. Joseph (Pitman, Boston, 1983).
9. V. E. Neuvazhaev and V. G. Yakovlev, Vopr. At. Nauki Tekh., Ser. Teor. Prikl. Fiz., No. 1, 28 (1988).
10. D. L. Youngs, Laser Part. Beams **12** (4), 725 (1994).
11. C. Cherfills and K. O. Mikaelian, Phys. Fluids **8**, 522 (1996).
12. J. D. Ramshaw, Phys. Rev. E **58** (5), 5834 (1998).
13. Y. Zhou, Phys. Fluids **13** (2), 538 (2001).
14. G. Dimonte and M. Schneider, Phys. Fluids **12** (2), 304 (2000).
15. R. I. Nigmatulin, Vestn. Mosk. Univ., Ser. 1: Mat., Mekh., No. 1, 83 (1965).
16. Ya. B. Zel'dovich and Yu. P. Raizer, *Physics of Shock Waves and High-Temperature Hydrodynamic Phenomena* (Nauka, Moscow, 1966, 2nd ed.; Academic, New York, 1966).
17. S. Z. Belen'kiĭ and E. S. Fradkin, Tr. Fiz. Inst. Akad. Nauk SSSR **29**, 207 (1965).
18. V. E. Neuvazhaev, in *Dynamics of Multiphase Systems: Proceedings of International Conference on Multiphase Systems, ICMS 2000, Ufa, Russia, 2000*, Ed. by M. Ilgamov, I. Akhatov, and S. Urmancheev, p. 87.
19. U. Alon, J. Hecht, D. Ofer, and D. Shvarts, Phys. Rev. Lett. **74**, 534 (1995).
20. V. A. Andronov, S. M. Bakhrakh, E. E. Meshkov, *et al.*, Zh. Éksp. Teor. Fiz. **71**, 806 (1976) [Sov. Phys. JETP **44**, 424 (1976)].
21. Yu. A. Kucherenko, S. I. Balabin, R. Cherret, and J. F. Haas, Laser Part. Beams **15**, 25 (1997).
22. S. G. Zaĭtsev, E. V. Lazareva, V. V. Chernukha, and V. M. Belyaev, Dokl. Akad. Nauk SSSR **283** (1), 94 (1985) [Sov. Phys. Dokl. **30**, 579 (1985)].
23. R. Samtaney and N. J. Zabusky, Phys. Fluids A **5**, 1285 (1993).
24. N. J. Zabusky, Annu. Rev. Fluid Mech. **31**, 495 (1999).
25. N. A. Inogamov, A. M. Oparin, A. Yu. Dem'yanov, *et al.*, Zh. Éksp. Teor. Fiz. **119**, 822 (2001) [JETP **92**, 715 (2001)].
26. J. G. Wouchuk and K. Nishihara, Phys. Plasmas **3**, 3761 (1996).
27. N. A. Inogamov, M. Tricottet, A. M. Oparin, and S. Bouquet, submitted to Phys. Lett. A (2002); physics/0104084.


*Translated by V. Sakun*

JETP Letters, Vol. 75, No. 11, 2002, pp. 552–555. Translated from Pis'ma v Zhurnal Éksperimental'noĭ i Teoreticheskoĭ Fiziki, Vol. 75, No. 11, 2002, pp. 669–672.


# Interference of Spin Splittings in Magneto-Oscillation Phenomena in Two-Dimensional Systems

**S. A. Tarasenko* and N. S. Averkiev**

*Ioffe Physicotechnical Institute, Russian Academy of Sciences, Politekhnicheskaya ul. 26, St. Petersburg, 194021 Russia*

**e-mail: tarasenko@coherent.ioffe.rssi.ru*

Received April 10, 2002; in final form, April 30, 2002

The spin splitting caused by the terms linear in wavevector in the effective Hamiltonian containing can give rise to the new magneto-oscillation phenomena in two-dimensional systems. It is shown that the joint action of the spin-dependent contributions due to the heterostructure asymmetry and to the lack of inversion center in the bulk material suppresses beats that arise in the magneto-oscillation phenomena in the presence of the terms of only one of these types. © *2002 MAIK "Nauka/Interperiodica".*

PACS numbers: 73.21.Fg; 73.50.Jt

Thermodynamic and kinetic coefficients such as heat capacity, magnetic susceptibility, conductivity, etc. oscillate in systems with a degenerate electron gas exposed to a quantizing magnetic field at low temperatures. Such a behavior of these coefficients is due to the appearance of the Landau levels, which successively intersect the Fermi level as the magnetic field increases. Measurements of the conductivity oscillations (Shubnikov–de Haas effect) and the oscillations of magnetic susceptibility (de Haas–van Alphen effect) are among the most efficient methods of structure characterization and determination of the carrier concentrations and relaxation times.

Quantum phenomena are highly sensitive to the fine structure of the carrier energy spectrum, so that even a small spin splitting may qualitatively modify the oscillation pattern. The terms linear in wavevector **k** in the effective Hamiltonian remove the degeneracy in the carrier spectrum. In a magnetic field, the spin splitting at the Fermi surface gives rise to the oscillations with close frequencies, i.e., to beats [1]. Such a behavior of the Shubnikov–de Haas effect was observed in two-dimensional systems with a hole channel at the silicon surface [2], with the electron gas in quantum wells based on narrow-band [3, 4] and wide-band [5] semiconductors, and in other structures. The zero-field spin splittings at the Fermi level were determined from the analysis of experimental data.

In the general case, the terms linear in **k** appear because the symmetry of heterostructures is lower than the symmetry of bulk materials. In the quantum wells grown on the basis of semiconductors with zinc blende lattice in the [001] orientation, there are two types of linear contributions to the effective electron Hamiltonian. First, they originate from the cubic terms in the Hamiltonian of a bulk material without inversion center. Averaging these cubic terms along the quantization axis in the case of low subband filling with carriers gives rise to the terms linear in **k** (BIA terms), where **k** is the wavevector in the electron gas plane [6]. Furthermore, a linear contribution can be caused by the intrinsic heterostructure asymmetry which is unrelated to the crystal lattice (Rashba terms) [1]. The relative intensities of these contributions to the effective Hamiltonian of a two-dimensional electron gas can change on passing from narrow-band to wide-band semiconductors [7]. Moreover, one can control the degree of heterostructure asymmetry, e.g., by applying an electric field perpendicular to the quantum well plane. Inasmuch as the physical nature and symmetry of the BIA terms are different from those of the Rashba terms, the direct addition of their contributions to the spin splitting would be incorrect.

In this work, we demonstrate that the BIA and Rashba contributions interfere in the magneto-oscillation phenomena. The presence of only one type of linear terms gives rise to the beats. However, if the intensities of both contributions are equal, the oscillations occur only at a single frequency and the beats disappear, although the Hamiltonian contains linear terms. The suppression of beats should take place in all magneto-oscillation phenomena. We take the Shubnikov–de Haas effect as an example to examine the interference of the BIA and Rashba contributions in detail. The magnetoresistance tensor will be calculated for zero temperature taking into account either only one contribution or both terms with the same intensity. The Zeeman splitting of electronic levels will be disregarded in this work, because it is small compared to the spacing between the Landau levels in the majority of semiconductor structures based on the III-V compounds in a

magnetic field perpendicular to the plane of electron gas.

Qualitatively, the disappearance of beats can be understood by analyzing the electronic spectrum in a zero magnetic field. In the absence of magnetic field, the effective Hamiltonian has the form

$$\hat{H} = \frac{\hbar^2 k^2}{2m^*} + \hat{H}_{BIA} + \hat{H}_R, \quad (1)$$

where $k = |\mathbf{k}|$ and $m^*$ is the effective mass. For a quantum well grown along the [001] direction, the spin-dependent BIA and Rashba contributions to the Hamiltonian of a two-dimensional electron gas can conveniently be written in the crystal system of coordinates ($x \parallel [1\bar{1}0]$, $y \parallel [110]$, $z \parallel [001]$):

$$\hat{H}_{BIA} = \alpha(\hat{\sigma}_x k_y + \hat{\sigma}_y k_x),$$
$$\hat{H}_R = \beta(\hat{\sigma}_x k_y - \hat{\sigma}_y k_x), \quad (2)$$

where $\hat{\sigma}_x$ and $\hat{\sigma}_y$ are the Pauli matrices.

In the presence of only one type of terms linear in $\mathbf{k}$, e.g., the BIA terms, the electronic spectrum is isotropic and consists of two different spin subbands (Fig. 1a):

$$E_\pm(k) = \frac{\hbar^2 k^2}{2m^*} \pm \alpha k. \quad (3)$$

If both contributions are essential, the spectrum becomes more complicated, and the energy becomes dependent on the direction of wavevector $\mathbf{k}$ [8]. However, the spectrum is simplified if the BIA and Rashba terms have the same intensity, i.e., if $|\alpha| = |\beta|$. In this case, the spectrum consists of two identical paraboloids shifted relative to each other in the $\mathbf{k}$ space. For example, if $\alpha = \beta$ (Fig. 1b), the paraboloids are shifted along $k_y$ and characterized by the spin states with $|\pm 1/2\rangle$ projections onto the $x$ axis. Accordingly, the electronic spectrum has the form

$$E_\pm(\mathbf{k}) = \frac{\hbar^2}{2m^*}[k_x^2 + (k_y \pm k_0)^2] - \frac{m^*\gamma^2}{2\hbar^2}, \quad (4)$$

where $k_0 = \gamma m^*/\hbar^2$ and $\gamma = 2\alpha = 2\beta$.

The magneto-oscillation frequencies of kinetic coefficients depend on the Fermi surface. In the presence of only one type of linear terms (Fig. 1a), the Fermi surfaces of two spin subbands are different because of the spin splitting $2\alpha k_F$, where $\hbar k_F$ is the Fermi momentum. The subbands are responsible for the oscillations with close frequencies, giving rise to beats. In the case that the intensities of the BIA and Rashba contributions are identical (Fig. 1b), the spin subbands are equivalent and the oscillations have the same frequency, and the beats do not arise.

In the regime of small Shubnikov–de Haas oscillations and electron scattering by short-range defects, the conductivity tensor can be represented as the sum of

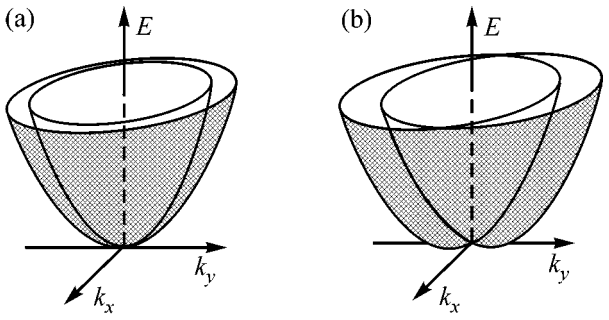


**Fig. 1.** Electronic energy spectrum in zero magnetic field for the case where (a) only one type of linear terms and (b) both contributions with equal intensities ($\alpha = \beta$) are taken into account.

classical magnetoresistance and the oscillating contribution,

$$\sigma_{xx} = \frac{Ne^2\tau/m^*}{1+(\omega_c\tau)^2}\left\{1 + \frac{2(\omega_c\tau)^2}{1+(\omega_c\tau)^2}\delta\right\},$$
$$\sigma_{xy} = -\frac{Ne^2\omega_c\tau^2/m^*}{1+(\omega_c\tau)^2}\left\{1 - \frac{1+3(\omega_c\tau)^2}{[1+(\omega_c\tau)^2](\omega_c\tau)^2}\delta\right\}, \quad (5)$$

where $N$ is the two-dimensional electron concentration, $\tau$ is the momentum relaxation time, $\omega_c = eB/m^*c$ is the cyclotron frequency, $B$ is the magnetic field, $e$ is the elementary charge, and $c$ is the velocity of light. The explicit expression for the quantity $\delta$ oscillating in a magnetic field depends on the Fermi surface. In two-dimensional systems with a simple band, $\delta$ has only one harmonic [9, 10].

The calculation shows that, in the presence of only one type of terms linear in $\mathbf{k}$, the oscillating quantity has the form

$$\delta = 2\exp\left(-\frac{\pi}{\omega_c\tau}\right)\cos\left(2\pi\frac{E_F}{\hbar\omega_c}\right)\cos\left(2\pi\frac{\alpha k_F}{\hbar\omega_c}\right), \quad (6)$$

where $E_F$ is the Fermi energy measured from the subband bottom in the absence of the linear terms. The dependence of $\delta$ on magnetic field has the form of beats, because $E_F \gg \alpha k_F$.

In the case that the intensities of the BIA and Rashba terms are equal, the oscillations, as in the absence of spin splitting, contain only one harmonic,

$$\delta = -2\exp\left(-\frac{\pi}{\omega_c\tau}\right)\cos\left(2\pi\frac{E_F'}{\hbar\omega_c}\right), \quad (7)$$

where $E_F' = E_F + m^*\gamma^2/(2\hbar^2)$ is the Fermi level measured from the bottom of the subbands.

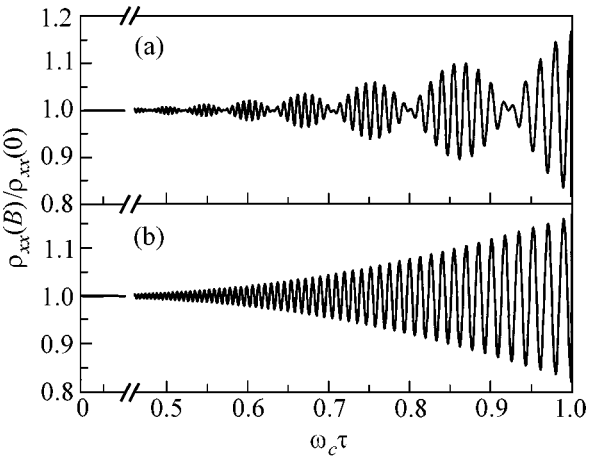


**Fig. 2.** Magnetic-field dependence of the resistivity $\rho_{xx}$ in the regime of Shubnikov–de Haas oscillations in the presence of (a) only one type of linear terms, $E_F\tau/\hbar = 50$ and $\alpha k_F/\hbar = 3$, and (b) both contributions with equal intensities and $E_F'\tau/\hbar = 50$.

Figure 2 displays the magnetic-field dependence of the resistivity

$$\rho_{xx} = \frac{\sigma_{xx}}{\sigma_{xx}^2 + \sigma_{xy}^2}.$$

If only one type of linear terms dominates (Fig. 2a), the spectrum of Shubnikov–de Haas oscillations contains two harmonics with close frequencies, and the field dependence of resistivity appears as beats. The frequency difference is determined by the spin splitting $2\alpha k_F$ at the Fermi level. In the case of identical intensities of the BIA and Rashba terms, $|\alpha| = |\beta|$ (Fig. 2b), the oscillations of both spin subbands have the same frequency and the beats are not observed.

In this work, a consistent theory of magneto-oscillation effects is developed using the Green's function method taking into account the terms linear in **k**. In the two-dimensional systems, small oscillations are observed in classical magnetic fields, $\omega_c\tau \le 1$, while the quantity $\exp(-\pi/\omega_c\tau)$ serves as a parameter determining the oscillation amplitude [9, 10]. We assume that the inequality $E_F\tau/\hbar \gg 1$ providing good conductivity is fulfilled. In the self-consistent Born approximation, one-particle electronic Green's function for electron scattering by the short-range defects has the form

$$\hat{G}_\varepsilon(\mathbf{r}, \mathbf{r}') = \sum_{nk_ys} \frac{\Psi_{nk_ys}(\mathbf{r})\Psi^\dagger_{nk_ys}(\mathbf{r}')}{\varepsilon + E_F - E_{ns} - X_\varepsilon}, \quad (8)$$

where $\Psi_{nk_ys}(\mathbf{r})$ are the spinor electron wave functions in a magnetic field $\mathbf{B} \parallel z$ with the Landau-gauge vector potential $\mathbf{A} = (0, Bx, 0)$; $E_{ns}$ are the electronic levels; $X_\varepsilon$ is the self-energy part of the Green's function; and $n$, $k_y$, and $s = \pm$ are the quantum numbers. Green's function (8) is a $2 \times 2$ matrix in the spin space.

In the presence of only one type of linear terms, the orbital and spin states are mixed (see [11]). At $\alpha k_F \gg \hbar\omega_c$, the electron energies near the Fermi level are

$$E_{n\pm} = \hbar\omega_c(n+1) \pm \alpha\sqrt{2(n+1)}/\lambda_B. \quad (9)$$

It is precisely the splitting $2\alpha\sqrt{2(n+1)}/\lambda_B$ in the spectrum (9) which gives rise to the beats in the magneto-oscillation phenomena.

If $|\alpha| = |\beta|$, then the wave functions are the products of the spin and orbital functions, and the electronic spectrum is determined by the expression

$$E_{n\pm} = \hbar\omega_c(n+1/2) - m^*\gamma^2/2\hbar^2. \quad (10)$$

In this case, the spectrum is not split, for which reason the oscillations due to the spin subbands have the same frequency and, hence, there will be no beats.

For the scattering from the short-range potentials, the self-energy part of the Green's function does not depend on $n$ [9] and, in both cases considered, on $s$ and satisfies the equation

$$X_\varepsilon = \frac{\hbar\omega_c}{\pi}\frac{\hbar}{4\tau}\sum_{ns}\frac{1}{\varepsilon + E_F - E_{ns} - X_\varepsilon}. \quad (11)$$

In the presence of only one type of linear terms, Eq. (11) has, to first order in parameter $\exp(-\pi/\omega_c\tau)$, the solution

$$X_\varepsilon = -\frac{i\hbar}{2\tau}\left[1 + 2\exp\left(-\frac{\pi}{\omega_c\tau}\right) \times \exp\left(2\pi i\frac{\varepsilon + E_F}{\hbar\omega_c}\mathrm{sgn}\varepsilon\right)\cos\left(2\pi\frac{\alpha k_F}{\hbar\omega_c}\right)\right]\mathrm{sgn}\varepsilon. \quad (12)$$

The multiplier $\cos(2\pi\alpha k_F/\hbar\omega_c)$ in the self-energy part (12) appears due to the level splitting. It is responsible for the beats in the magneto-oscillation phenomena, e.g., in the Shubnikov–de Haas effect.

If $|\alpha| = |\beta|$, then the self-energy part contains no such term:

$$X_\varepsilon = -\frac{i\hbar}{2\tau}\left[1 - 2\exp\left(-\frac{\pi}{\omega_c\tau}\right) \times \exp\left(2\pi i\frac{\varepsilon + E_F'}{\hbar\omega_c}\mathrm{sgn}\varepsilon\right)\right]\mathrm{sgn}\varepsilon. \quad (13)$$

The Green's function allows the calculation of various kinetic and thermodynamic coefficients. Using the standard methods [12, 13], one can deduce expressions (5)–(7) for the conductivity tensor in the regime of Shubnikov–de Haas oscillations. The remaining components are related by the expressions $\sigma_{xx} = \sigma_{yy}$ and $\sigma_{yx} = -\sigma_{xy}$.

The interference of the spin-dependent contributions caused by the heterostructure asymmetry and the lack of inversion center in the bulk material was considered in [8], where the anisotropy of electronic spectrum was taken as an example. Such an anisotropy was experimentally observed in the Raman studies of the GaAs/AlGaAs structures [14]. The fact that the terms linear in **k** nonadditively add together in the case of weak localization was predicted in [15] and observed in the measurements of anomalous magnetoresistance in [16]. It was shown in [17] that the joint action of both spin-dependent contributions gives rise to the anisotropy of relaxation times in the quantum well plane. It has been demonstrated in this work that the interference of the BIA and Rashba terms linear in **k** qualitatively alters the pattern of magneto-oscillation phenomena in two-dimensional systems.

This work was supported by the Russian Foundation for Basic Research, INTAS, the program of the Presidium of the Russian Academy of Sciences "Low-Dimensional Quantum Structures," and programs of the Ministry of Industry, Science, and Technologies of the Russian Federation.

## REFERENCES

1. Yu. A. Bychkov and É. I. Rashba, Pis'ma Zh. Éksp. Teor. Fiz. **39**, 66 (1984) [JETP Lett. **39**, 78 (1984)]; Yu. A. Bychkov and É. I. Rashba, J. Phys. C **17**, 6039 (1984).
2. S. I. Dorozhkin and E. B. Ol'shanetskiĭ, Pis'ma Zh. Éksp. Teor. Fiz. **46**, 399 (1987) [JETP Lett. **46**, 502 (1987)].
3. J. Luo, H. Munekata, F. F. Fang, and P. J. Stiles, Phys. Rev. B **38**, 10142 (1988); J. Luo, H. Munekata, F. F. Fang, and P. J. Stiles, Phys. Rev. B **41**, 7685 (1990).
4. B. Das, D. C. Miller, S. Datta, *et al.*, Phys. Rev. B **39**, 1411 (1989); B. Das, S. Datta, and R. Reifenberger, Phys. Rev. B **41**, 8278 (1990).
5. P. Ramvall, B. Kowalski, and P. Omling, Phys. Rev. B **55**, 7160 (1997).
6. M. I. D'yakonov and V. Yu. Kachorovskiĭ, Fiz. Tekh. Poluprovodn. (Leningrad) **20**, 178 (1986) [Sov. Phys. Semicond. **20**, 110 (1986)].
7. G. Lommer, F. Malcher, and U. Rössler, Phys. Rev. Lett. **60**, 728 (1988).
8. E. A. de Andrada e Silva, Phys. Rev. B **46**, 1921 (1992).
9. T. Ando, J. Phys. Soc. Jpn. **37**, 1233 (1974).
10. A. Isihara and L. Smrčka, J. Phys. C **19**, 6777 (1986).
11. É. I. Rashba, Fiz. Tverd. Tela (Leningrad) **2**, 1224 (1960) [Sov. Phys. Solid State **2**, 1109 (1960)].
12. N. S. Averkiev, L. E. Golub, S. A. Tarasenko, and M. Willander, J. Phys.: Condens. Matter **13**, 2517 (2001).
13. S. A. Tarasenko, Fiz. Tverd. Tela (St. Petersburg) **44**, (2002) (in press) [Phys. Solid State **44**, (2002) (in press)].
14. B. Jusserand, D. Richards, G. Allan, *et al.*, Phys. Rev. B **51**, 4707 (1995).
15. F. G. Pikus and G. E. Pikus, Phys. Rev. B **51**, 16928 (1995).
16. W. Knap, C. Skierbiszewski, A. Zduniak, *et al.*, Phys. Rev. B **53**, 3912 (1996).
17. N. S. Averkiev and L. E. Golub, Phys. Rev. B **60**, 15582 (1999).

*Translated by V. Sakun*

JETP Letters, Vol. 75, No. 11, 2002, pp. 556–558. Translated from Pis'ma v Zhurnal Éksperimental'noĭ i Teoreticheskoĭ Fiziki, Vol. 75, No. 11, 2002, pp. 673–675.


# Excess Noise Peaks in Porous Silicon-Based Diode Structures

**E. S. Demidov, N. E. Demidova, V. V. Karzanov, and V. N. Shabanov**

*Lobachevsky State University, Nizhni Novgorod, 603600 Russia*

*e-mail: demidov@phys.unn.runnet.ru*

Received April 19, 2002

Results of an experimental observation of the voltage oscillations associated with a discrete tunneling of holes in porous silicon at room temperature are presented. The noise characteristics of diode structures with a porous silicon interlayer formed on heavily boron-doped silicon single crystals are studied. Peaks of excessive noise are observed at frequencies of ~1 MHz, at which single-electron oscillations should be expected. The peak noise power is found to increase with current according to the ~2.5 power law and, at a current density of 0.15 A/cm$^2$, to exceed the noise power of the receiver by three to four orders of magnitude. The complex shape of the noise spectrum and its extension to the higher frequency region with increasing current are explained by the three-dimensionality of the system of nanometer-sized silicon grains embedded in insulating silicon dioxide of porous silicon. © *2002 MAIK "Nauka/Interperiodica".*

PACS numbers: 73.40.Sx; 73.40.Gk

Porous silicon (PS) as a representative of nanometer-sized 1D and 0D heterostructures is most extensively studied in connection with its luminescence properties and the possibilities of its application in optoelectronics [1, 2]. At the same time, certain prerequisites and preliminary experiments suggest that PS can be a suitable object for studying the discrete tunneling of electrons or holes and for the development of a new generation of nanoelectronics, namely, single-particle electronics. According to our earlier publication [3], the topology of pores and the partial oxidation of PS lead to the formation of an anisotropic material with strings of nanometer-sized silicon grains embedded in insulating silicon dioxide. The predominant presence of two solid phases, Si and $SiO_2$, in PS (apart from air) were experimentally demonstrated in [4]. Because of the small capacitance between the grains, a manifestation of the Coulomb blockade of the electron or hole tunneling along the strings is possible. From our previous experiments [3], it was found that, at room temperature, the current–voltage characteristics of diode structures with PS interlayers formed on $p^+$ Si crystals (boron doped *p*-type silicon with conductivities of 0.01 and 0.005 Ω cm) exhibit steps in current. The steps were attributed to the discrete tunneling of holes. In this paper, we continue the aforementioned investigation. According to the theory of discrete tunneling [5], because of the noncommutativity of the charge and current operators, the voltage across the tunneling junction that contains a conducting grain in the insulating gap between metal plates oscillates with the frequency

$$f = I_1/e, \quad (1)$$

where $I_1$ is the current per grain through the structure and $e$ is the electron charge. If (as in [3]) we assume that the distance between the grain strings in PS is about 10 nm, then, in a diode structure with a PS interlayer and with a junction cross section of 0.6 mm$^2$, a current $I$ = 1 mA should give rise to voltage oscillations with a frequency of about 1 MHz. In our experiment, we tried to detect single-electron voltage oscillations at frequencies of ~ 1 MHz.

We studied diode structures with PS interlayers, namely, the metal(In)–PS($p^+$ Si)–metal(In) structures, which were fabricated by an express technology that was simpler than in [3] and uses *p*-type silicon single crystals with even higher boron doping levels (boron-doped *p*-type silicon with a conductivity of 0.001 Ω cm). The PS layers were formed by the conventional method [1] consisting in an anodic dissolution of silicon at the surface of plates with the (110) orientation in a solution formed by equal volumes of 48% HF and ethanol $C_2H_5OH$; the current density was 10 mA/cm$^2$ and the duration of the process was 10 min. After etching, the samples were rinsed in deionized water and in ethanol and then dried in air. The metallic indium contact with PS had an area of 0.5–0.7 mm$^2$. The other indium contact was on the part of the silicon sample surface that was free from PS. Because of the use of heavily doped silicon, the series resistance introduced by such contacts with solid silicon into the diode structure was much smaller than the resistance of porous silicon.

The current–voltage characteristics were recorded point by point, with a direct current or in a periodic mode with a frequency of 100 Hz, by a TR-4805 curve tracer. To observe the voltage oscillations in the diode structures, we used conventional equipment for the noise measurements in two-terminal radioelectronic devices. The current in the diode structure was set by a controlled stabilized voltage source with a series resis-

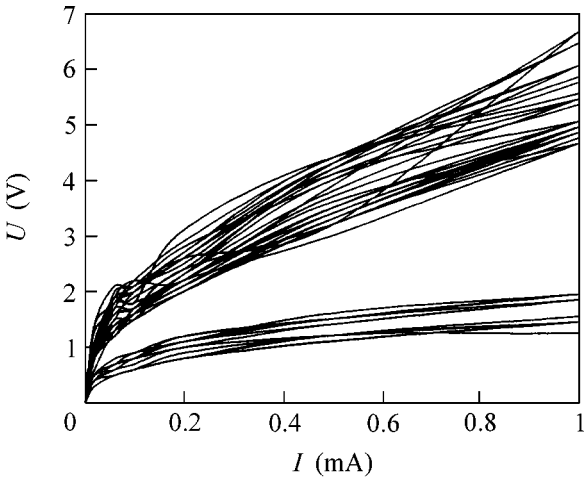


**Fig. 1.** Current–voltage characteristics of a diode structure with a porous silicon interlayer. The lower family of curves corresponds to the forward branch, and the upper family of curves, to the reverse branch. The upward shift of the curves in both cases is related to the oxidative aging of porous silicon.

tance of 4.7 kΩ. The alternating voltage across the diode structure was measured by a superheterodyne receiver of the L2-7 impedance meter with an input resistance of 4.7 kΩ, a passband $\Delta f = 6$ kHz, and a linear detector at the output. The equipment was calibrated by a G4-158 oscillator. The noise measurements were performed point by point in the frequency range from 0.4 to 10 MHz. The intrinsic noise factor of the receiver in this frequency range did not exceed 5 dB.

The procedure of measuring the electric characteristics of the diode structures with PS was complicated by the fact that the current–voltage characteristics of these structures considerably vary during their storage in air because of the oxidation of PS. The oxidation was evidenced by the growth of the voltage across the structure at a fixed current of either polarity. The fastest changes occurred within several hours after the formation of PS. On the following day, the process slowed down. Therefore, the noise characteristics of the structures were measured starting from the second day, and the measurements continued for three days. In addition, within 24 h after the fabrication of PS, for currents greater than 0.3 mA, the effect of charge accumulation in PS was observed. This effect manifested itself in the hysteresis of the current–voltage characteristics when the latter were recorded point by point. The hysteresis was absent in the *I–U* characteristics recorded by the curve tracer with a sweep period of 100 Hz. In this case, the characteristics were smooth and anhysteretic, but changed in shape with time. When negative polarity occurred at the contact of indium with PS, the current through the diode structure decreased approximately by a factor of 2 within 1.5–2 min, whereas in the case of positive polarity, it increased by a factor of 3–5 within 3–5 min, depending on the maximal current value.

Figure 1 shows the static current–voltage characteristics of one of the diode structures with PS, and Figs. 2 and 3 present the noise spectra for the same structure at fixed frequencies. The spectra were obtained with increasing current by the equilibrium voltage values at fixed values of *I* at which the noise measurements were performed. From Fig. 1, one can see that the current–voltage characteristics are nonlinear and nonsymmetric with respect to the current direction. The higher conductivity is observed when a positive voltage is applied to the silicon substrate and the holes are injected from the $p^+$ Si substrate into PS. The *I–U* curve branches corresponding to this polarity will be arbitrarily called the forward branches. The opposite polarity corresponds to the reverse branches. The regions with negative differential resistance appear in Fig. 1 only in the case of a slow current variation, and they are caused by the aforementioned effect of charge accumulation. In the records obtained with a period of 10 ms, no negative slopes are observed in the *I–U* curves. The *I–U* dynamics will be discussed in more detail in the following paper.

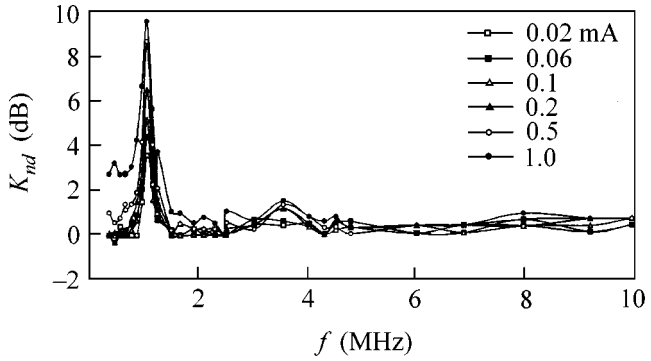


**Fig. 2.** Frequency dependence of the noise factor $K_{nd}$ of a diode structure with a porous silicon interlayer in the forward direction at different currents.

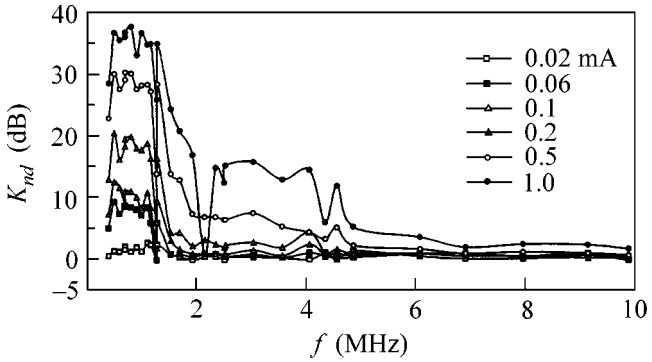


**Fig. 3.** Same as in Fig. 2 for the reverse current direction.

Figures 2 and 3 present the families of spectral dependences of the conditional noise factor $K_{nd}$ for the forward and reverse directions of the bias voltage, respectively, at several fixed current values. The noise factor is called conditional, because it is determined as $20\log(U_{nd}/U_{ns})$, where $U_{nd}$ is the time-averaged (over 10 s) voltage at the detector output with the diode structure connected to the measuring system, and $U_{ns}$ is a similar quantity obtained for the system with the disconnected diode structure. To determine the true noise factor, it is necessary to take into account the differential resistance of the diode structure. According to Fig. 1, the differential resistance strongly depends on the current for both polarities of the bias voltage.

As one can see from Figs. 2 and 3, when a current flows through a diode structure with a PS interlayer, a nonuniform noise spectrum manifests itself in the frequency range 0.4–10 MHz. For the forward direction, a sharp peak of oscillations is observed with its maximum near a frequency of 1.1 MHz at a current of 1 mA, and the amplitude of this peak is an order of magnitude higher than the noise power of the receiver. If we assume that, according to Fig. 1, the differential resistance of the diode at this current is about 200–300 Ω, i.e., an order of magnitude smaller than the input resistance of the receiver, the true noise power of the diode structure proves to be three orders of magnitude higher than the receiver noise power and is characterized by a maximal noise factor of about 30 dB. In the reverse direction, according to Fig. 1, at currents of about 0.5–1 mA, the diode structure has a differential resistance close to the input resistance of the receiver, and the conditional noise factor coincides with the true one within several decibels. In this case, the noise maximum also occurs at frequencies near 1 MHz. In this frequency band at a current of 1 mA, the noise power amplitude exceeds the noise power of the receiver by four orders of magnitude. The spectral characteristic exhibits a fine structure, which is reproduced at different currents. For currents $I = 0.5$–$1$ mA, an excessive noise band appears at frequencies up to 5 MHz. The estimated dependence of the excessive noise power of the diode structure on the current shows that the maximal power increases with current approximately by the power law and is proportional to $I^{2.5}$.

The excessive noise peaks observed occurred in the region of 1 MHz, i.e., at frequencies at which, according to Eq. (1), a current of 1 mA should be accompanied by single-electron voltage oscillations related to the discrete tunneling of electrons. However, a simple linear increase in the oscillation frequency with increasing current as in Eq. (1) is not observed in the experiment. As the current increases, a more complex extension of the spectrum to the higher frequency region can be seen in Fig. 3. According to [3], this can possibly be related to the three-dimensionality of the system of grain strings in PS with hundreds of grains across the PS layer thickness. The astonishingly stable peak observed at 1.1 MHz in the case of the forward bias in Fig. 2 and the reproducible fine structure of the peaks near 1 MHz in the case of the reverse bias in Fig. 3 for currents varying by a factor of 50 testify to the intrinsic resonance properties of PS. The inductive contribution is presumably caused by the phase lag of the current through grains with respect to the grain charge variation, as this phase lag is characteristic of discrete tunneling.

This work was supported by INTAS grant no. 000-0064.

## REFERENCES

1. O. Bisi, S. Ossicini, and L. Pavesi, Surf. Sci. Rep. **38**, 1 (2000).
2. Z. F. Krasil'nik, in *Proceedings of the V Russia Conference on Physics of Semiconductors, 2001*, Vol. 1, p. 15.
3. E. S. Demidov, V. V. Karzanov, and V. G. Shengurov, Pis'ma Zh. Éksp. Teor. Fiz. **67**, 794 (1998) [JETP Lett. **67**, 839 (1998)].
4. M. I. Strashnikova, V. L. Voznyĭ, V. Ya. Reznichenko, and V. Ya. Gaĭvoronskiĭ, Zh. Éksp. Teor. Fiz. **120**, 409 (2001) [JETP **93**, 363 (2001)].
5. D. V. Averin and K. K. Likharev, Zh. Éksp. Teor. Fiz. **90**, 733 (1986) [Sov. Phys. JETP **63**, 427 (1986)].

*Translated by E. Golyamina*

JETP Letters, Vol. 75, No. 11, 2002, pp. 559–562. Translated from Pis'ma v Zhurnal Éksperimental'noĭ i Teoreticheskoĭ Fiziki, Vol. 75, No. 11, 2002, pp. 676–679.


# Energy Spectrum of Quantum Wells in PbTe/PbEuTe-Based Structures from Photoluminescence Data

**I. I. Zasavitskiĭ*, E. V. Bushuev*, E. A. Andrada-e-Silva**, and E. Abramof****

** Lebedev Physical Institute, Russian Academy of Sciences, Moscow, 119991 Russia*

*** Instituto Nacional de Pesquisas Espaciais– NPE, 12201 Sao Jose dos Campos, SP, Brazil*

*e-mail: zasavit@sci.lebedev.ru*

Received April 22, 2002

It is shown that the energies of radiative transitions between the ground states of electrons and holes for high-quality deep PbTe quantum wells at low temperatures are described well within the framework of the two-band model with regard to the nonparabolicity, strong anisotropy, and multivalley character of the band structure and also uniaxial deformation, that is present in the heterostructure. For a two-dimensional system, the temperature coefficient of the variation of the forbidden band gap decreases with decreasing well width, which is explained by a weakening of the electron–phonon interaction. © *2002 MAIK "Nauka/Interperiodica".*

PACS numbers: 73.21.Fg; 78.55.Hx

A number of works are devoted to the size quantization effect on the energy spectrum of quantum well structures based on IV–VI semiconductors [1–6]. Optical absorption, giving information on high-lying quantum states, was primarily studied in quantum-sized PbTe/PbEuTe-based structures. The uniaxial deformation effect was also taken into account in interpreting the results within the framework of both six-band [5] and simpler [1–3, 6] models. However, the values of deformation potential constants used by various authors differed from each other several times, which leaves open the question of the value of these constants.

This work is devoted to studying the size quantization and temperature effects on the energy spectrum of PbTe/PbEuTe-based quantum-well structures in which $E_g$ for the PbEuTe barrier reaches values of ~ 0.5 eV, and $E_g$ for PbTe, which serves as a quantum well, comprises 0.189 eV in the bulk material at 4 K. The calculated spectrum was compared with the data obtained from photoluminescence (PL) spectra, which gives accurate information on the band edges. The energies of radiative transitions between the ground states in the conduction and valence bands are described well within the framework of the two-band model with regard to the nonparabolicity, strong anisotropy, and multivalley character of PbTe and also to the uniaxial deformation present in quantum wells. In addition, a decrease in the $dE_g/dT$ coefficient with decreasing well width was observed in the two-dimensional system.

PbTe/PbEuTe-based heterostructures were grown on freshly cleaved (111)$BaF_2$ substrates by molecular beam epitaxy [7]. In order to remove the consequences of the strong mismatch of the lattice constant with the substrate ($\Delta a/a$~ 4.5%), a thick (~4 μm) $Pb_{1-x}Eu_xTe$ ($x \approx 0.06$) buffer layer was grown initially. Then, a PbTe-based quantum well of differing width (from 2.3 to 18 nm) and a $Pb_{1-x}Eu_xTe$ barrier ~50 nm thick of the same composition as the buffer layer were grown. In this sequence, 50 high-quality quantum wells were grown. The quality was checked on a high-resolution X-ray diffractometer, with the use of which up to ten Bragg satellites were observed. The structure period, well width, and the value of mechanical strains $\varepsilon_{\|}$ due to the mismatch of the lattice constants between the well and the barrier ($\Delta a/a$ ~ 0.3%) were determined from X-ray measurements [6]. Isomorphic growth is observed, because the well widths used are smaller than the critical thickness. The value of $E_g$ for the barrier was determined from optical absorption spectra.

PL spectra were measured at 4.2 and 77.4 K. A YAG pulsed laser ($h\nu$ = 1.17 eV) was used for excitation. A grating IR monochromator, a Ge:Au-based radiation detector, and a V9-5 stroboscopic voltage transducer were used for the analysis of emission spectra, which allowed us to work with an energy resolution of <0.5 meV. Note that this resolution is several times better than the corresponding resolution for low-lying states in the optical absorption spectra. The excitation level reached relatively high values (up to $10^5$ W/cm$^2$).

As a rule, the emission spectrum consisted of one induced emission line whose halfwidth was 1–3 meV, depending on the sample. For high-quality epitaxial IV–VI layers, radiative transitions proceed with quasi-momentum conservation, and the induced emission line arises on the sharp low-energy side of the spontaneous emission line [8]. Thus, the position of the induced emission line to a high accuracy corresponds to the band edge. The correction for $E_g$ due to many-body interactions in the crystal is small (~1 meV at $n, p \leq$

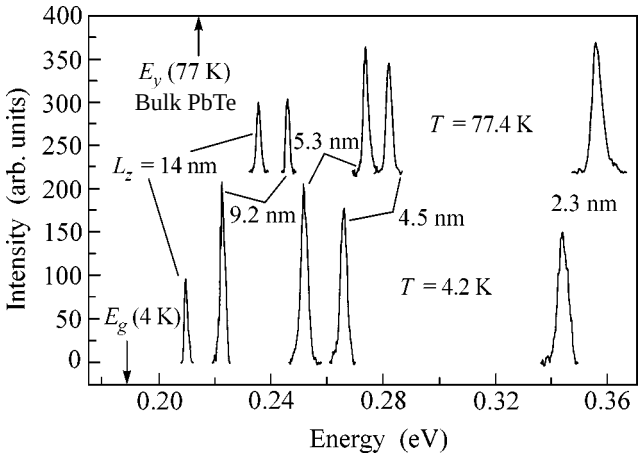


**Fig. 1.** Emission spectra of structures with PbTe/PbEuTe-based quantum wells as functions of the well width at temperatures of 4 and 77 K.

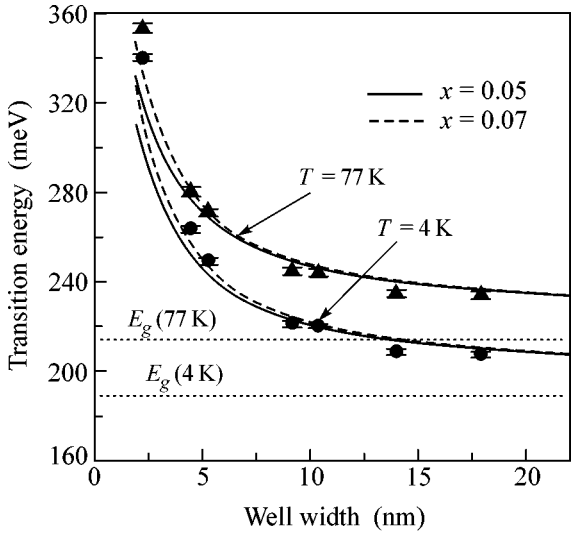


**Fig. 2.** Dependence of the radiative transition energies on the well width at temperatures of 4 and 77 K. Curves correspond to the calculation of optical transition in the main valley at average deformation $\varepsilon = 2.5 \times 10^{-3}$. Dotted lines correspond to $E_g$ for a thick (2 μm) epitaxial PbTe layer.

$10^{17}$ cm$^{-3}$ [9]) because of the small effective mass and the high dielectric constant in IV–VI semiconductors. Optical absorption gives an overestimated (by several meV) value of the transition energy because of the finite concentration of charge carriers in IV–VI semiconductors, which leads to the band filling effect.

Because of quantization, the energy of radiative transition increased with decreasing well width at both temperatures (Fig. 1). The increase in emission intensity with decreasing well width also engages our attention. This increase is due to the increase of electron confinement for nonequilibrium charge carriers.

For the preferred crystallographic direction [111] determined by the orientation of the $BaF_2$ substrate, four equivalent valleys in PbTe are divided into one main valley with longitudinal effective mass and three oblique valleys with effective mass close to a transverse mass. Because the anisotropy coefficient is large ($K \approx 10$), size-quantization levels in oblique valleys go markedly deep into the band; therefore, radiative transitions proceed in the main valley. In addition to the intervalley splitting, there is a deformation shift toward the high-energy side, which for the main valley is approximately four times larger than for oblique valleys. However, with the well width used in this work, $L_z < 20$ nm, the size-quantization shift plays a determining part in the position of lower levels [3].

The energies of optical transitions in quantum wells were calculated analytically in the framework of the two-band model with the mirror symmetry of nonparabolic bands and in the envelope function approximation [10]. It was assumed that the discontinuities of the conduction and valence bands are equal ($\Delta E_c = \Delta E_v$), and deep quantum wells have a rectangular shape in accordance with the X-ray data. The energy change due to the uniaxial deformation $\varepsilon_\perp$ directed perpendicular to the heterostructure was calculated by the equations

$$\delta E_l = (0.92D_d - 1.08D_u)\varepsilon_\perp \text{ for the main valley,}$$

$$\delta E_o = (0.92D_d + 0.77D_u)\varepsilon_\perp \text{ for oblique valleys, and}$$

$$\varepsilon_\perp = -1.08\varepsilon_\parallel.$$

Here, the numerical coefficients take into account elastic constants, which weakly depend on temperature. The constants of optical deformation potentials $D_d$ = 4.3 eV and $D_u$ = –2.8 eV were taken from [3]. Then, at $\varepsilon_\perp = 3 \times 10^{-3}$, we obtain $\delta E_l/\delta E_o \approx 4$, and the value $\delta E_l \approx$ 20 meV represents a significant (~10%) shift for a narrow-gap semiconductor.

The optical transition energies at two temperatures are shown in Fig. 2 as functions of the well width. It is evident that the PL data are in good agreement with the calculated curves for transitions in the main valley. This agreement is achieved only by taking into account the measured deformation and using the constants of deformation potentials determined in [3]. It was also taken into account that the deformation depends on the well width, decreasing by 20% when the well width increases up to 20 nm. For smoothness, the calculated curves in Fig. 2 are given for a certain average value of deformation $\varepsilon = 2.5 \times 10^{-3}$, though a comparison with the experiment was performed for each sample with regard to the deformation measured in it and the barrier height. Because the wells are relatively deep, the calculated curve for the ground state is virtually independent of the variation of the europium content in the barriers within the range $0.05 \le x \le 0.07$.

Thus, the energies determined from the luminescence data for the optical transitions between the ground states of electrons and holes in deep PbTe quantum wells are in good agreement with the results of calculations within the framework of the two-band model [10], though more sophisticated calculations within the six-band model are necessary for the high-lying states [5]. This result, in combination with the mechanical strains measured in the PbTe/PbEuTe heterostructures, allows the conclusion that the constants of the optical deformation potentials found are most reliable. Note that we also used this approach to advantage for interpreting the results of low-temperature PL in deep strained PbSe/PbSrSe-based quantum wells, for which the position of size-quantization levels assumed in [3] was recently confirmed by measuring absorption spectra [11].

The temperature dependence of the forbidden band gap $E_g$ is determined by the coefficient $dE_g/dT$, which is positive for IV–VI semiconductors. In the case of the bulk PbTe crystal, it equals $+4.5 \times 10^{-4}$ eV/K in the temperature range 50–300 K. Here, the contribution due to the variation of the lattice constant with temperature comprises $3\alpha B(dE_g/dP)_T = +1.7 \times 10^{-4}$ eV/K, where $\alpha$ is the linear thermal expansion coefficient, $B$ is the bulk modulus of elasticity, and $(dE_g/dP)_T$ is the pressure coefficient. Hence, the remaining part (about 60%) is due to the electron–phonon interaction. At low (<50 K) temperatures, the $dE_g/dT$ coefficient decreases, tending to zero, because the electron–phonon interaction decreases, and $\alpha \longrightarrow 0$ in accordance with the Nernst heat theorem.

The calculation of the $dE_g/dT$ coefficient for low-dimensional systems is absent. The experiment shows that this coefficient decreases with the size of the quantum-sized object. In particular, it was shown in [12] based on absorption spectra of PbS and PbSe quantum dots that the $dE_g/dT$ coefficient drops to zero and even changes its sign when the size of quantum dots decreases. In this work, an analogous effect was observed in the absorption and PL spectra of the two-dimensional PbTe/PbEuTe system. However, the accuracy of measuring the $dE_g/dT$ coefficient by absorption spectra is relatively low, especially at low temperatures, where this coefficient nonlinearly goes to zero, which possibly leads to the sign reversal. Therefore, we determined the difference $\Delta E_g = E_g(77\text{ K}) - E_g(4\text{ K})$ from PL spectra. Here, $E_g$ implies the energy of the radiative transition between the electron and hole ground states. For PbTe, this approach is also important because the quantum yield of emission in this material decreases at elevated temperatures because of intervalley Auger recombination. It is evident in Fig. 3 that the difference $\Delta E_g$ strongly decreases with decreasing well width (more than two times for a well with the width $L_z$= 2.3 nm as compared to the bulk crystal); however, its sign remains unchanged. Thus, the $dE_g/dT$ coefficient for the two-dimensional PbTe/PbEuTe system also decreases as the well width decreases as low as 2.3 nm but does not change its sign.

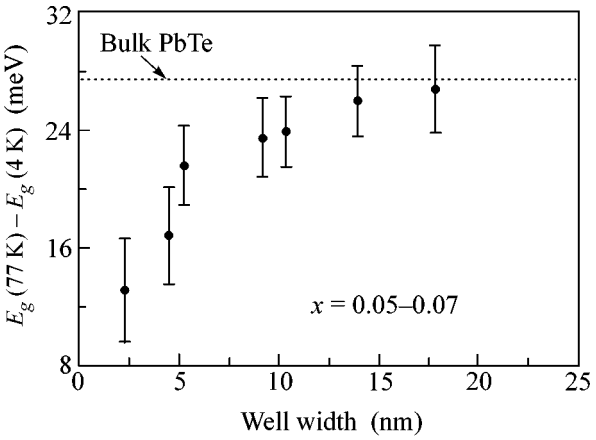


**Fig. 3.** Difference $\Delta E_g = E_g(77\text{ K}) - E_g(4\text{ K})$ as a function of the PbTe well width. The dotted line indicates the value of this difference for the bulk material.

Because the contribution due to the temperature variation of the lattice constant weakly depends on the well width, the experimental result points to a change in the contribution to $dE_g/dT$ due to the electron–phonon interaction. Confined 2D phonons and interface phonons propagating along the quantum well plane arise in the two-dimensional system. Although the role of interface phonons increases as the well width decreases, their contribution to the electron–phonon interaction is relatively low. Long-wavelength phonon modes propagating perpendicular to the well plane do not exist in the case of 2D phonons. Therefore, polar interaction in an ionic 2D crystal decreases. Hence, the observed decrease in $\Delta E_g$ with decreasing well width points to a weakening of the electron–phonon interaction in the 2D system in agreement with the results of calculations (see [13] and references therein).

Thus, the energies of radiative transitions between the ground states in the conduction and valence bands in high-quality PbTe/PbEuTe systems with deep quantum wells are described well within the framework of the two-band model with regard to nonparabolicity, strong anisotropy, and the multivalley character of the band structure. With regard to the measured mechanical strains, this allowed the optical deformation potentials to be reliably determined for PbTe. It was found that the $dE_g/dT$ coefficient in the 2D system decreases with decreasing well width, which is explained by a weakening of the electron–phonon interaction.

## REFERENCES

1. D. L. Partin, IEEE J. Quantum Electron. **24**, 1716 (1988).

2. A. Ishida, Y. Sase, and H. Fujiyasu, Appl. Surf. Sci. **33/34**, 868 (1988).
3. M. V. Valeiko, I. I. Zasavitskii, A. V. Matveenko, *et al.*, Superlattices Microstruct. **9**, 195 (1991).
4. G. Springholz, M. Kriechbaum, W. Hofmann, *et al.*, Superlattices Microstruct. **13**, 25 (1993).
5. S. Yuan, G. Springholz, G. Bauer, *et al.*, Phys. Rev. B **49**, 5476 (1994).
6. E. Abramof, E. A. de Andrada e Silva, S. O. Ferreira, *et al.*, Phys. Rev. B **63**, 085304 (2001).
7. E. Abramof, P. H. O. Rappl, A. Y. Ueta, *et al.*, J. Appl. Phys. **88**, 725 (2000).
8. D. M. Gureev, O. I. Davarashvili, I. I. Zasavitskiĭ, *et al.*, Fiz. Tekh. Poluprovodn. (Leningrad) **9**, 1902 (1975) [Sov. Phys. Semicond. **9**, 1251 (1975)].
9. R. Rupprecht and H. Pascher, Phys. Rev. B **50**, 16931 (1994).
10. E. A. de Andrada e Silva, Phys. Rev. B **60**, 8859 (1999).
11. H. Z. Wu, N. Dai, M. B. Johnson, *et al.*, Appl. Phys. Lett. **78**, 2199 (2001).
12. A. Olkhovets, R.-C. Hsu, A. Lipovskii, *et al.*, Phys. Rev. Lett. **81**, 3539 (1998).
13. N. Sawaki, J. Phys. C **19**, 4965 (1986).

*Translated by A. Bagatur'yants*

JETP Letters, Vol. 75, No. 11, 2002, pp. 563–565. Translated from Pis'ma v Zhurnal Éksperimental'noĭ i Teoreticheskoĭ Fiziki, Vol. 75, No. 11, 2002, pp. 680–683.


# Conductivity of $C_{60}$ Fullerene Crystals under Dynamic Compression up to 200 kbar

**Yu. A. Osip'yan[1], V. E. Fortov[2], K. L. Kagan[2], V. V. Kveder[1], V. I. Kulakov[1], A. N. Kur'yanchik[2], R. K. Nikolaev[1], V. I. Postnov[2], and N. S. Sidorov[1]**

[1] *Institute of Solid State Physics, Russian Academy of Sciences, Chernogolovka, Moscow region, 142432 Russia*

[2] *Institute of Problems of Chemical Physics, Russian Academy of Sciences, Chernogolovka, Moscow region, 142432 Russia*

Received April 22, 2002

The conductivity $\sigma$ of $C_{60}$ fullerene crystals is measured under quasi-isentropic loading by a spread shock wave to a pressure of 200 kbar at the initial temperatures 293 and 77 K. A sharp increase in $\sigma$ by seven to eight orders of magnitude is detected: from $10^{-6}$–$10^{-7}$ $\Omega^{-1}$ cm$^{-1}$ at normal conditions to 5 $\Omega^{-1}$ cm$^{-1}$ under pressure from 100 to 200 kbar. The conductivity of samples under pressure decreases with decreasing temperature, which is characteristic of semiconductors. On pressure release, $\sigma$ regains its initial value. © *2002 MAIK "Nauka/Interperiodica".*

PACS numbers: 72.80.Rj; 71.30.+h; 62.50.+p

In the crystalline state, $C_{60}$ fullerene is a semiconductor with an energy gap $E_g$ of about 2.1 eV and with rather narrow valence and conduction bands (about 0.5 eV each). The excitonic optical absorption edge corresponds to an energy of about 1.7 eV (i.e., the binding energy of singlet excitons is about 0.4 eV) [1]. The $C_{60}$ molecules are mainly bound by the Van der Waals forces, and the compressibility of $C_{60}$ crystals under hydrostatic pressure is very high. Under a pressure of 50 kbar, the relative variation of the crystal volume $\Delta V/V_0$ reaches 20%, and at 200 kbar it exceeds 30% [2]. One would expect that the valence and conduction band widths, which exponentially depend on the intermolecular distance, will rapidly increase under hydrostatic pressure. This process should be accompanied by a decrease in the energy gap, and, at some pressure, the crystal can transform to the metal state.

An analysis of numerous data on the changes of the optical absorption spectra of $C_{60}$ crystals under hydrostatic pressure (see, e.g., [3, 4]) shows that the energy gap decreases rapidly with increasing pressure. However, different experiments yield noticeably different values for the slope of the pressure dependence of energy gap $dE_g/dP$: from –10 to –3 meV/kbar. Therefore, estimates of the pressure corresponding to the transition to the metal state show a considerable scatter (200–700 kbar). Moreover, it is still unclear whether the transition of $C_{60}$ crystals to the metal state is possible before the collapse of the $C_{60}$ molecules or their polymerization.

The wide scatter of experimental data can be caused by several factors. First, high pressures may lead to the polymerization of $C_{60}$ molecules (the formation of covalent bonds between the molecules) [5]. Polymerization is a rather slow, thermally activated process additionally depending on the relative orientation of molecules, and it can be present to a variable extent in different experiments thus affecting the data for $dE_g/dP$.

Second, most hydrostatic experiments use a pressure-transmitting medium (such as liquid xenon, alcohol mixtures, etc.). Because of the large diameter of $C_{60}$ molecules and their almost spherical shape, the $C_{60}$ crystal structure is characterized by the presence of large intermolecular voids, which can be easily filled with the molecules of the pressure-transmitting medium. The latter process can strongly affect the electron band structure of the samples.

The aforementioned problems can be avoided in experiments with a shock action [6, 7]. Special dynamic experiments allow one to obtain fairly smooth quasi-isentropic loading conditions with minimal heating of the medium. Earlier [8], a method was proposed for recording the phase transformations under such a compression by measuring the resistivity $R$ of thin samples. In these measurements, the characteristic time of the pressure increase to the maximal value was ~1 μs, which was many orders of magnitude greater than the thermodynamic equilibrium time but much smaller than the time characterizing the diffusion processes.

The idea of the method is as follows. The sample under study is placed between two plates made of glass or fused quartz. One plate is in contact with a metal screen. The dynamic loading occurs from the side of the screen, which is struck by a metal striker accelerated by explosion products to a velocity of ~2 km/s. Because of the anomalous compressibility of glass and

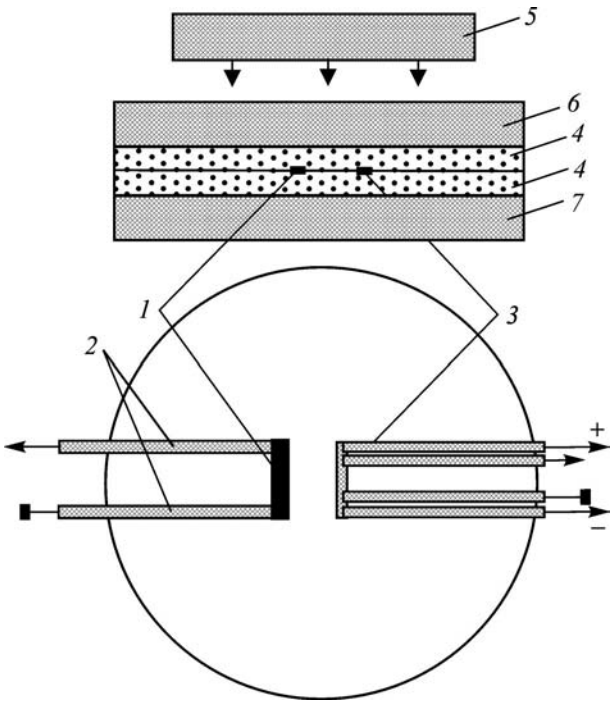


**Fig. 1.** Schematic diagram of the experiment: (*1*) a $C_{60}$ sample, (*2*) electric leads to the sample (copper foil strips), (*3*) a manganin pressure sensor, (*4*) quartz plates (5 mm), (*5*) an aluminum striker, (*6*) a copper screen (6 mm), and (*7*) a rear copper screen.

fused quartz below the elastic limit and by virtue of the thermodynamic laws governing the transition to the plastic state in these materials, no shock wave can exist in them at pressures below ~120 kbar [9]. The shock wave is spread as it travels from the boundary between the quartz plate and the metal screen and transforms to a continuous wave of isentropic compression, which makes it possible to considerably reduce the irreversible shock-wave heating of the sample. As a result, in the conditions of the dynamic experiment, the sample under study is loaded smoothly without a shock. This method had been successfully used earlier in studying the "dielectrization" of lithium and sodium [10, 11].

Using the dynamic compression method described above, we studied the conductance of crystalline samples of a $C_{60}$ fullerene with a density of 1.67 g/cm$^3$ under a pressure of up to 200 kbar.

The dynamic experiment is schematically represented in Fig. 1. The fullerite sample *1* had the form of a rectangular plate with dimensions $8 \times 3 \times 1.5$ mm. Copper foil leads *2* were attached to the sample by a conducting adhesive. The sample and the manganin pressure sensor *3* were separated from the quartz surfaces by a teflon film 0.1 mm thick. The quartz plates *4* were 5 mm thick. The assembly was loaded by an aluminum striker *5* through a 6-mm-thick copper screen *6*, the striker being accelerated to a velocity of 2 km/s by a special explosion device. The rear copper screen *7* was necessary for the generation of a reflected shock wave and a pressure increase to 200 kbar. The experiments were carried out at the initial room temperature $T = 293$ K and also by cooling the measuring cell to the temperature of liquid nitrogen $T = 77$ K. The recording device was a Tektronix-744A digital oscilloscope with a passband of 500 MHz.

Solid samples of $C_{60}$ were fabricated by the method developed at the Institute of Solid State Physics of the Russian Academy of Sciences. A 10-g portion of chromatographically cleaned fullerene powder 99.98% pure was placed in a quartz ampoule 30 mm in diameter and 500 mm in length. One end of the ampoule was made of flat polished quartz. The ampoule was evacuated to a pressure of $10^{-6}$ Torr and heated to 300°C. Under a constant pumping during 8–10 h, the fullerene powder was cleaned from traces of organic solvents and volatile impurities. After this procedure, at the flat end of the ampoule, a fullerene polycrystal was grown by resublimation in a temperature gradient (the sublimation temperature was 650°C, the crystallization temperature was 600°C, and the time of growth of a 1-mm-thick layer was 72 h). The resulting flat polycrystal was cut into samples. X-ray examination (a D-500 Siemens apparatus) showed that the samples correspond to the fcc phase of $C_{60}$ with the lattice constant $a = 14.192 \pm 0.004$ Å.

The resistivity was measured against the background of the resistances $R_{sh} = 10$–$10\,000\ \Omega$ shunting the sample, as in [12]. Because of the small sample thickness, it was possible to assume that, at every instant, the sample was compressed to the pressure $P$ that was measured by a manganin-foil pressure sensor positioned in the same plane. With this assumption, the dependence of $R$ on $P$ could be obtained from the results of a single experiment by analogy with one cycle of pressure growth and drop in static systems.

The oscillogram of one of the experiments (without cooling the assembly) is presented in Fig. 2. In the first pressure wave with the amplitude up to 100 kbar, the conductance of the sample $1/R$ increases from its initial value about $10^{-7}\ \Omega^{-1}$ to a value of about $10^{-2}\ \Omega^{-1}$. With the arrival of the reflected wave whose maximal amplitude is 200 kbar, the conductance of the sample sharply (within approximately 100 ns) increases to $0.35\ \Omega^{-1}$. When the load is removed, the conductance drops to its initial value. The pressure dependence of conductance observed for a $C_{60}$ sample cooled to 77 K is qualitatively the same, with the only difference that the value of $1/R$ in the second pressure wave is much smaller: about $2 \times 10^{-3}\ \Omega^{-1}$.

Knowing the geometric dimensions of the sample and assuming that the shock compressibility of crystalline $C_{60}$ is close to the compressibility of compacted graphite with a density of 1.77 g/cm$^3$ [13], it is possible to estimate the conductivity $\sigma$ of the sample under the shock compression. It was found that, when the initial

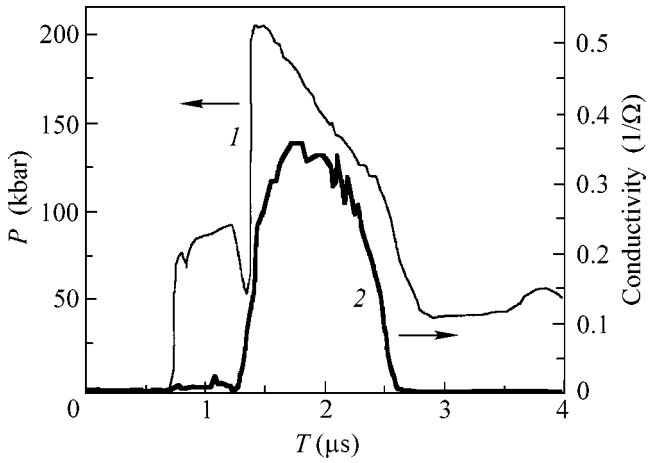


**Fig. 2.** Time dependences of (*1*) the pressure and (*2*) the conductivity of a $C_{60}$ sample under compression by a spread shock wave.

temperature of a $C_{60}$ sample was 293 K, its conductivity $\sigma$ under pressure up to 200 kbar reached 5 $\Omega^{-1}$ cm$^{-1}$. For a sample cooled to 77 K before loading, the conductivity $\sigma$ observed under a similar dynamic compression was almost two orders of magnitude less: 0.07 $\Omega^{-1}$ cm$^{-1}$. This kind of temperature dependence of the conductivity is characteristic of semiconductors. Note that, in the first case, $\sigma$ increases with pressure by seven to eight orders of magnitude with respect to the initial conductivity equal to $10^{-6}$–$10^{-7}$ $\Omega^{-1}$ cm$^{-1}$. One should also note the reversible character of the conductivity variation (see Fig. 2), which testifies that the samples regain their properties after the dynamic load is removed. This assumption was tested in special experiments in which $C_{60}$ samples placed in flat metal storage ampoules [14] were subjected to shock-wave action. The geometry of the devices was identical to the geometry of the measuring cell shown in Fig. 1. The X-ray phase analysis showed that the stored samples had a single-phase $C_{60}$ structure with a somewhat smaller lattice constant $a$ = 14.145 ± 0.004 Å.

The results of our study testify to a sharp decrease in the band gap of $C_{60}$ crystals under pressure. However, the experimental temperature dependence of conductivity under pressure indicates that the band gap does not decrease as low as zero, and the samples compressed to 200 kbar remain semiconducting. This fact qualitatively agrees with the data on the effect of static pressure on crystalline $C_{60}$ [15]. However, quantitatively, the value of $\sigma$ observed in our experiments in the dynamic compression conditions is two orders of magnitude greater than the conductivity observed at room temperature under a static pressure of 200 kbar. The difference between our experiments and the static ones is presumably caused by the dynamic heating of the samples in our experiments: in the case of the isentropic compression to 200 kbar, the temperature range of this heating is 100–200°C. It is also possible that the quantitative difference is partially caused by such processes as the polymerization of the $C_{60}$ molecules and the diffusion of impurities into the sample, which occur in the static experiments.

This work was supported in part by the Russian Foundation for Basic Research (project no. 00-02-17528).

## REFERENCES

1. A. N. Izotov, V. V. Kveder, Yu. A. Osip'yan, *et al.*, Zh. Éksp. Teor. Fiz. **114**, 2211 (1998) [JETP **87**, 1205 (1998)].
2. S. J. Duclos, K. Brister, R. C. Haddon, *et al.*, Nature **351**, 380 (1991).
3. K. P. Meletov, V. K. Dolganov, O. V. Zharikov, *et al.*, J. Phys. I **2**, 2097 (1992).
4. F. Moshary, N. H. Chen, I. F. Silvera, *et al.*, Phys. Rev. Lett. **69**, 466 (1992).
5. I. O. Bashkin, V. I. Rashchupkin, A. F. Gurov, *et al.*, J. Phys.: Condens. Matter **6**, 7491 (1994).
6. L. V. Al'tshuler, Prikl. Mekh. Tekh. Fiz. **6**, 93 (1978).
7. Ya. B. Zel'dovich and Yu. P. Raizer, *Physics of Shock Waves and High-Temperature Hydrodynamic Phenomena* (Nauka, Moscow, 1966, 2nd ed.; Academic, New York, 1966).
8. V. I. Postnov, S. S. Nabatov, A. A. Shcherban', and V. V. Yakushev, Zh. Tekh. Fiz. **57**, 1181 (1987) [Sov. Phys. Tech. Phys. **32**, 694 (1987)].
9. G. I. Kanel' and A. M. Molodets, Zh. Tekh. Fiz. **46**, 398 (1976) [Sov. Phys. Tech. Phys. **21**, 226 (1976)].
10. V. E. Fortov, V. V. Yakushev, K. L. Kagan, *et al.*, Pis'ma Zh. Éksp. Teor. Fiz. **70**, 620 (1999) [JETP Lett. **70**, 628 (1999)].
11. V. E. Fortov, V. V. Yakushev, K. L. Kagan, *et al.*, Pis'ma Zh. Éksp. Teor. Fiz. **74**, 458 (2001) [JETP Lett. **74**, 418 (2001)].
12. V. E. Fortov, A. S. Kotosonov, V. I. Postnov, *et al.*, Dokl. Akad. Nauk **357**, 761 (1997) [Phys. Dokl. **42**, 673 (1997)].
13. M. V. Zhernokletov, V. N. Zubarev, R. F. Trunin, and V. E. Fortov, *Experimental Data on Impact Compressibility and Adiabatic Expansion of Condensed Substances under High Energy Density* (Chernogolovka, 1996).
14. G. A. Adadurov, Usp. Khim. **55**, 555 (1986).
15. B. Sundqvist, Adv. Phys. **48**, 1 (1999).

*Translated by E. Golyamina*

JETP Letters, Vol. 75, No. 11, 2002, pp. 566–569. Translated from Pis'ma v Zhurnal Éksperimental'noĭ i Teoreticheskoĭ Fiziki, Vol. 75, No. 11, 2002, pp. 684–688.


# Superconductivity Signs at 110 K on Boride Inclusion Phases $TiB_k$ in the Titanium Matrix

**V. V. Volkov, K. G. Myakishev, P. P. Bezverkhii, V. G. Martynets, and E. V. Matizen**

*Institute of Inorganic Chemistry, Siberian Division, Russian Academy of Sciences, pr. Akademika Lavrent'eva 3, Novosibirsk, 630090 Russia*

*e-mail: matizen@casper.che.nsk.su.*

Received April 24, 2002

An experimental check of theoretically predicted high-temperature superconductivity in titanium borides $TiB_k$ is done. These predictions, published as a theoretical phase diagram, concerned the possibility of the existence of high-$T_c$ $TiB_k$ phases with compositions $1.43 < k < 2.57$. In titanium samples coated by diffuse surface boride layers of depth-variable composition $TiB_k$, there is a jump in the electrical resistance versus temperature dependence $R(T)$ at 110 K. This proves the presence of superconducting inclusion phases in the layers. Diffuse boride layers were applied to metallic titanium by exposing its surface to a $B_2H_6 + H_2$ gas mixtures at 610–700°C followed by vacuum annealing. The composition of boride layers was studied by mass spectrometry. © *2002 MAIK "Nauka/Interperiodica".*

PACS numbers: 74.10.+v; 74.70.Ad

The discovery of medium-temperature superconductivity for magnesium diboride $MgB_2$ ($T_c = 39$ K [1]), which has comparatively simple composition and structure, stipulated a search for nonoxide superconducting materials, including metal borides and related compounds [2]. Note that it was as early as in 1989 that high-temperature superconductivity was predicted in binary titanium boride phases $TiB_k$ in which $k$ is not necessarily an integer [3–5]. Later, these predictions were replicated in systematizing works [6, 7]. However, no experimental checks of such predictions have yet been published. Therefore, we undertook a provisional experimental check, and here we report the results.

Most experimental evidence is in favor of low superconducting transition temperatures in borides. The systematization of data concerning low-temperature superconductivity in binary transition-metal borides at below 1 K [8] showed that the phases of composition $MB_2$, where M = Ni, Zr, Hf, V, Ta, Cr, or Mo (the $AlB_2$ structural type, Fig. 1d), have no superconductivity down to 0.42 K. For $TiB_2$, transition temperatures of $T_c < 1.26$–1.9 K were reported [9]. No superconducting transition was observed down to 0.42 K in $MB_6$ (M = Sr, Ca, Ba), MB (M = Mo, Nb, Cr), $W_2B_5$, $Cr_5B_3$, $UB_2$, $UB_4$, or $UB_{12}$. The superconducting properties of $MB_6$ and mixed systems of the $(Y,La)B_6$ type were reported [10, 11]. For $YB_6$, $T_c = 6.0$ K; for the $(Y_{0.5}La_{0.5})B_6$ mixed phase, $T_c = 1.6$ K. Mixed hexaborides $(YYb)B_6$, $(YCa)B_6$, and $(YTh)B_6$ show a notable decrease in $T_c$ compared to the $T_c$ of pure $YB_6$. Therefore, in $MB_2$ (except for the aforementioned $MgB_2$) and $MB_6$ compounds and in several binary borides, superconductivity exists only at low temperatures.

Some ternary borides also show superconductivity [12, 13]. Examples are $LuRh_4B_4$ (11.5 K), $LuRuB_2$ (10.0 K), $LuRhB_4$ (11.3 K), $Y(Rh_{0.85}Ru_{0.15})_4B_4$ (9.4 K), and $(Lu_{0.5}Th_{0.5})Os_3B_2$ (4.1 K).

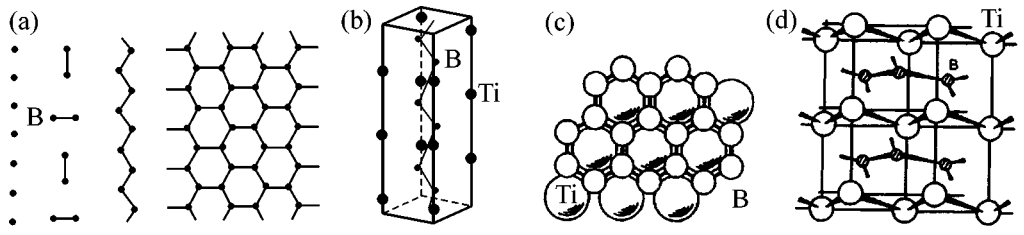


**Fig. 1.** Structures of some borides. (a) Idealized models of boron linking in metal borides: isolated boron atoms, boron atom pairs, zigzag chains in MB, and hexagonal chains in $MB_2$. (b) Atom arrangement in TiB. (c) A hexagonal layer in the structure of a metal diboride ($MB_2$) characteristic of $TiB_2$ and $MgB_2$. (d) The dominant structural type $AlB_2$.

0021-3640/02/7511-0566$22.00 © 2002 MAIK "Nauka/Interperiodica"

The crystal structures of borides involve combinations of M–B, B–B, and M–M bond arrays. Selected representative fragments of boride structures are imaged in Fig. 1. Boron atoms can occur as separate atoms or pairs, or they can form zigzag linear structures (TiB) or planar unidimensional and two-dimensional hexagonal networks (Figs. 1a, 1b) [6, 7, 14–17]. Layer crystal structures of the $AlB_2$ type (Figs. 1c, 1d) are intrinsic to $MgB_2$, $TiB_2$, and transition-metal diborides $MB_2$ [1, 14, 17]. These structures are an alternation of layers of hexagonal networks formed from B and M atoms. Quasi-two-dimensional layer–network fragments are also intrinsic to the structures of classical high-$T_c$ cuprates [18]. In the structure of TiB (Fig. 1b), boron atoms form zigzag chains rather than layers or networks [16]. No superconductivity in TiB was discovered.

The occurrence of high-temperature superconductivity in binary titanium boride phases $TiB_k$ was predicted first by Zaitsev [5], then replicated by Shveikin and Ivanovskii [6, 7]. A layer structural model was ascribed to $TiB_k$. The final result was represented as a theoretical phase diagram with the field of $TiB_k$ compositions for which high-temperature superconductivity is expectable (Fig. 2). The Habbard–Emery generalized model [19, 20] including the suggested electronic states of atoms in the system was used in estimations. The occurrence of high-temperature superconductivity at $1.43 < k < 2.57$ (including the range of $2 < k < 18/7$ in $Ti_2B_5$) was predicted, as well as and its absence in TiB, $Ti_3B_4$, and $TiB_2$. However, variation in $T_c$ in $TiB_k$ as a function of $k$ was not quantified. This prediction mostly coincides with data [3, 4] that indicate the possibility of high-temperature superconductivity in $TiB_k$ phases.

It is interesting that, in terms of the BCS model, borides of light elements have higher $T_c$ among the isostructural compounds. Existing evidence is consistent with the model: examples are ZrB (3.4 K) and HfB (3.1 K), an NaCl structure; NbB (8.25 K) and TaB (4.0 K), a δ-CrB structure; $Mo_2B$ (5.86 K) and $W_2B$ (3.18 K), a $CuAl_2$ structure [21].

We have attempted to experimentally verify the prediction of high-temperature superconductivity in $TiB_k$ phases. The experience of investigations into oxide high-$T_c$ systems requires the design of definite crystal-chemical structures of working phases and the absence of external impurities and other polymorphs in them. This requirement also applies to boride systems. Temperatures of up to 1500–2000°C are required to ensure the completion of the B(solid) + M(solid) $\longrightarrow$ $MB_k$ (solid) solid-state reaction during synthesis of refractory transition-metal borides. The starting components and reaction products (B, M, $MB_k$) have high affinities to $O_2$, $N_2$, $H_2O$, and carbon, making the formation of oxide, nitride, carbide, and other external phases possible. High temperatures are also necessary for perfect crystal structures to form.

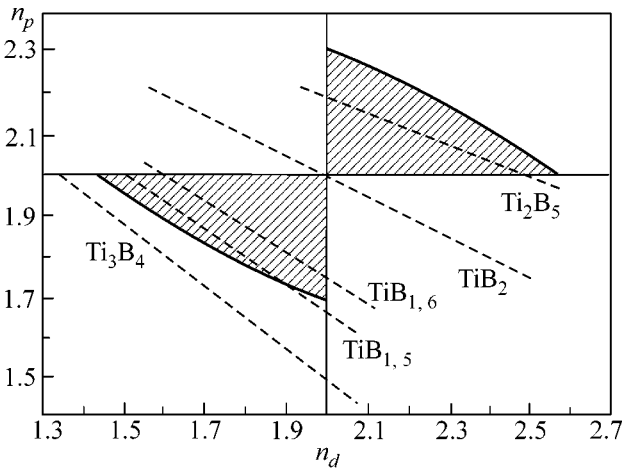


**Fig. 2.** Phase diagram for the compound $TiB_k$ [5]. Superconducting fields are shaded. Notation: $n_p$ is the number of holes in the $2p^4$ shell of boron anions, and $n_d$ is the number of holes in the $3d^4$ shell of titanium cations. The electrical neutrality lines for several $TiB_k$ compounds are shown by dashed straight lines.

However, a pair of more stable borides, TiB and $TiB_2$, is more likely to form than the desired $TiB_k$ phases. To avoid this difficulty, we prepared samples that could contain $TiB_k$ inclusion phases in the polycrystalline titanium matrix.

Our experiments were carried out on commercial titanium samples shaped into $5 \times 4 \times 1.5$-mm plates. Samples with $TiB_k$ inclusions in the structure of surface layers were prepared by doping titanium metal by boron from a diborane(6) $B_2H_6 + H_2$ gas flow at 610–700°C for 3–4 h. Above 600°C, $B_2H_6$ dissociates to $H_2$ and B. The newly formed boron deposits on the titanium surface and then diffuses into the metal to yield $TiB_k$ inclusion boride phases of variable composition. To form $TiB_k$ inclusion structures, coated plates were annealed in vacuum at 710–820°C for 4–5 h. Pure $B_2H_6$ mixed with $H_2$ (1 : 1 vol/vol) was prepared from a mechanochemical solid-state reaction of $SnCl_2$ with $NaBH_4$ in a hermetic vibrational gas-producer installation [22]. Previously, titanium plates were polished with a fine abrasive, and surface oxides were removed by aqueous hydrochloric plus hydrofluoric acid mixtures. The vapor boration was carried out in a sealed quartz tubular reactor heated by an electrical furnace and equipped with a thermocouple and a temperature controller. The reactor was attached by tubing to the $B_2H_6$ producer and a vacuum system. Batches of four to five samples were processed in a gradient-free zone of the reactor. Black diffuse layers of $TiB_k$ borides appeared on the samples as a result.

Secondary ion mass spectrometry in tandem with $Ar^+$ ion surface etching was used to determine the B : Ti

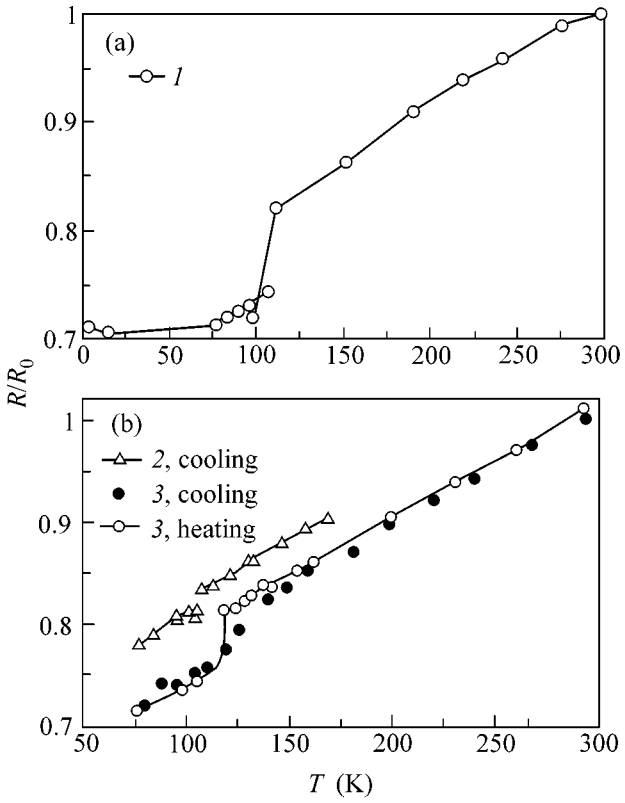


**Fig. 3.** $R(T)/R_0$ curves for (a) sample 1 and (b) samples 2 and 3. The curves are numbered to correspond to sample numbering.

atomic ratio and to estimate the variation in $k$ for $TiB_k$ compositions with $h$, the depth of the diffuse boride layer. The instrument used was an MS-702 AEI mass spectrometer (see table).

Resistance $R$ was measured by a standard four-probe technique with a 2-mA current from 77 to 293 K.

Determination of the B : Ti atomic ratio in boride layers on titanium for selected samples as a function of depth $h$

| Character of the $R/R_0(T)$ curve | $h$, μm | B : Ti atomic ratio |
|---|---|---|
| Transition at 110 K (Fig. 3a) | 0–0.3 | 10 |
| | 1.4 ± 0.3 | 1 |
| | 2.8 ± 0.3 | 0.5 |
| No transition; semiconductor conductivity | 0–0.3 | 6 |
| | 1.4 ± 0.3 | 0.1 |
| | 2.8 ± 0.3 | 0.05 |
| No transition; metal conductivity | 0–0.3 | 3 |
| | 1.9 ± 0.6 | 0.1 |
| | 3.8 ± 0.6 | 0.02 |
| No transition; starting titanium (unexposed to $B_2H_6$) | 0–0.3 | 0.0003 |

The probes were four copper wires positioned at a distance of 1 mm parallel to one another. A test sample was pressed to the probes at a certain force, such that an electrical contact appeared along the entire length of the sample. The assembly—a cell with contacts, a sample, and conductor wires—was mounted in a bulky temperature-controlled copper block, which was cooled by the vapor of liquid nitrogen or helium. The temperature was measured by a copper–constantan thermocouple with an error of ±0.01 K; the voltage was measured with an error of ±0.01 μV.

The following measurement procedure was practiced. First, the starting resistance of the sample $R_0$ was measured, then the measurement cell was cooled, and $R$ was measured after fixing temperature $T$. After reaching the temperature of liquid nitrogen, the temperature was raised in steps, and $R$ was measured again. The results of the measurements are presented as $R/R_0$ versus $T$ plots in Fig. 3.

Even during provisional investigations, we observed $R(T)$ dropped in a jump at 100–110 K when cooling several boride-coated titanium samples. Of the two batches, only a few samples showed this effect upon cooling (see Fig. 3, curves for samples *1*, *2*, and *3*). When the temperature was raised, $R$ increased in a jump at the same temperature (Fig. 3, sample *3*). The starting metallic (uncoated) titanium has no such effect.

We relate the jump in $R$ of samples 1, 2, and 3 to the appearance of superconducting inclusion phases $TiB_k$ with $2 < k < 18/7$ (for example, $Ti_2B_5$) in the layers whose composition varies with depth, in accordance with theoretical predictions [3–5]. Note that not all titanium samples processed by $B_2H_6$ under identical conditions showed such transitions in $R$. Of the two replicate batches, only a few samples showed this transition: two samples of the ten prepared in batch I and seven of the twenty five prepared in batch II. A total of 12 samples showed the transition at 110 K. Clearly, in our case, boride layers of sufficient thickness with definite B-to-Ti ratios are the necessary condition for high-$T$ superconductivity to appear in $TiB_k$ inclusions. Some samples had pure metallic $R(T)$ curves; others had semiconductor curves (probably, due to a compact boron film).

The table displays the B-to-Ti atomic ratio in boride layers on titanium measured by mass spectrometry at various depths $h$. In a sample showing a clear-cut transition at 110 K (Fig. 3a), B : Ti = 10–0.5 (table) at boride layer depths of $h$ = 0–2.8 μm; that is, $TiB_k$ with $2 < k < 18/7$ can be present, especially at $h \sim 0.3$–1.4 μm. The other two samples show no transition; they do not bear boride layers of the required thickness and composition: their B : Ti ratio for $h > 0.3$ μm is almost an order of magnitude lower than in sample 1.

To estimate the volume of the superconducting phase in the samples, we employed phenomenological theory to calculate a resistance jump in a composite material consisting of a normal component and super-

conducting inclusions that have a definite shape of the other component with $T_c$ transition in the effective medium approximation [23]. In the approximation of the smallness of the volume fraction $c_s$ of the superconducting phase,

$$\rho_s/\rho_n = 1 - c_s/n_c, \quad (1)$$

where $\rho_n$ is the resistance of the composite in the limit where $c_s$ tends to zero, $\rho_s$ is the resistance of the material after the superconducting transition in the other inclusion phase occurred, and $n_c$ is the demagnetization factor (for spheric inclusions, $n_c = 1/3$). With reference to the percolation threshold [24],

$$\rho_s/\rho_n = 1 - (c_s/n_c)(l - c_s/c_p) - (c_s/c_p)^2. \quad (2)$$

In Eq. (2), the threshold concentration $c_p$ for the transport current is a function of the geometry of superconducting domains. For spheric superconducting inclusions, estimation gives a value of $c_p \approx 0.15$. Using Eq. (2) and our data of Fig. 3a for sample 1 (this sample showing the largest jump in $R$ in the region of 110 K) and regarding inclusions as spheric, we estimated the volume fraction of the superconducting $TiB_k$ phase. For this sample, $c_s \approx 0.026$; for samples 2 and 3, $c_s < 0.01$. The estimate according to Zhdanov [24] showed that, with the amount of the superconducting phase in our sample being less than 2.5%, the diamagnetic moment is less than $10^{-9}$ A m$^2$, making its measurements difficult.

Apart from diborane(6), other volatile boron compounds were used to apply diffuse layers to titanium. We used decaborane(14) $B_{10}H_{14}$ and its sulfur derivative $SB_9H_{11}$ in vapor borating the surface of titanium plates. Diffuse layers bearing B, C, and N were prepared from triethylamine borane $(C_2H_5)_3N \cdot BH_3$ vapor. $B_2H_2$ was used to coat titanium mononickelide TiNi. However, none of the samples prepared in these manners showed low-temperature resistance jumps.

The general result of this study is the following. We have shown that titanium samples coated by diffuse boride layers of variable composition $TiB_k$ show a jump in the $R(T)/R_0$ curve at 100–110 K; this jump can serve as a sign of the presence of newly formed high-$T$ inclusion phases. Relatively low temperatures (610–700°C) and synthesis involving the $B_2H_6$ gas phase could be essential for the formation of boride phases with desired structures and compositions.

Evidently, the results presented here are the basis for further investigations to give a deeper insight into the phenomenon in question.

This work was in part supported by the High-Temperature Superconductivity Program, project no. 98009 and the Russian Foundation for Basic Research, project no. 02-02-16564.

## REFERENCES

1. J. Nagamatsu, N. Nakagawa, T. Muranka, *et al.*, Nature **410**, 63 (2001).
2. A. L. Ivanovskiĭ, Usp. Khim. **70**, 811 (2001).
3. F. Vahldiek, New Technology Week, 9 January, 6 (1989).
4. V. Ahern, Supercond. Week, 23 January, 9 (1989).
5. P. O. Zaĭtsev, Sverkhprovodimost: Fiz., Khim., Tekh. **2**, 36 (1989).
6. G. P. Shveĭkin and A. L. Ivanovskiĭ, Usp. Khim. **63**, 751 (1994).
7. A. L. Ivanovskiĭ and G. P. Shveĭkin, *Quantum Chemistry in Material Science: Boron, Its Alloys and Compounds* (Izd. "Ekaterinburg," Yekaterinburg, 1997).
8. N. Leyarovska and E. A. Lelarovski, J. Less-Common Met. **67**, 249 (1979).
9. G. V. Samsonov, L. Ya. Markovskiĭ, A. F. Zhigach, and M. G. Valyashko, *Boron, Its Compounds and Alloys* (Izd. Akad. Nauk Ukr. SSR, Kiev, 1960).
10. R. J. Sobozak and M. J. Sienko, J. Less-Common Met. **67**, 167 (1979).
11. R. Hiebl and M. J. Sienko, Inorg. Chem. **19**, 2179 (1980).
12. D. C. Johnston and H. F. Braun, in *Superconductivity in Ternary Compounds II: Superconductivity and Magnetism*, Ed. by M. V. Maple and O. Fischer (Springer-Verlag, Berlin, 1982), pp. 11–140.
13. E. J. Felten, J. Am. Chem. Soc. **78**, 5977 (1956).
14. N. N. Greenwood, in *Comprehensive Inorganic Chemistry*, Ed. by A. F. Trotman-Diskenson (Pergamon, Oxford, 1973), Vol. 1, pp. 665–991.
15. E. L. Muetterties, *The Chemistry of Boron and Its Compounds* (Wiley, New York, 1967).
16. B. F. Decker and J. S. Kasper, Acta Crystallogr. **7**, 77 (1954).
17. V. Post, F. W. Glaser, and D. Moskowits, Acta Metall. **2**, 20 (1954).
18. R. B. King, Inorg. Chem. **29**, 2164 (1990).
19. J. Hubbard, Proc. R. Soc. London, Ser. A **281**, 401 (1964).
20. V. J. Emery, Phys. Rev. Lett. **58**, 2794 (1987).
21. Z. Fisk, in *Proceedings of the Conference on Boron-Rich Solids, Albuquerque, 1990*, Ed. by D. Emin, T. L. Aselage, A. C. Switendick, *et al.* (American Institute of Physics, New York, 1991), AIP Conf. Proc. **231**, 155 (1991).
22. V. V. Volkov and K. G. Myakishev, Zh. Prikl. Khim. **69**, 199 (1996).
23. A. Davidson and M. Tinkham, Phys. Rev. B **13**, 3261 (1976).
24. K. R. Zhdanov, Preprint No. 91-08, Inst. Neorg. Khim. Sib. Otd. Akad. Nauk SSSR (Institute of Inorganic Chemistry, Siberian Division, Academy of Sciences of USSR, Novosibirsk, 1991).

*Translated by O. Fedorova*

JETP Letters, Vol. 75, No. 11, 2002, pp. 570–574. Translated from Pis'ma v Zhurnal Éksperimental'noĭ i Teoreticheskoĭ Fiziki, Vol. 75, No. 11, 2002, pp. 689–694.


# Bose Condensation of Interwell Excitons in Double Quantum Wells

**A. V. Larionov[1], V. B. Timofeev[1]*, P. A. Ni[1], S. V. Dubonos[2], I. Hvam[3], and K. Soerensen[3]**

[1] *Institute of Solid-State Physics, Russian Academy of Sciences, Chernogolovka, Moscow region, 142432 Russia*

[2] *Institute of Microelectronic Technology, Russian Academy of Sciences, Chernogolovka, Moscow region, 142432 Russia*

[3] *Microelectronic Centre, DK 2800 Lyngby, Denmark*

**e-mail: timofeev@issp.ac.ru*

Received April 29, 2002

The luminescence of interwell excitons in double quantum wells GaAs/AlGaAs (*n–i–n* heterostructures) with large-scale fluctuations of random potential in the heteroboundary planes was studied. The properties of excitons whose photoexcited electron and hole are spatially separated in the neighboring quantum wells were studied as functions of density and temperature within the domains on the scale less than one micron. For this purpose, the surfaces of the samples were coated with a metallic mask containing specially prepared holes (windows) of a micron size an less for the photoexcitation and observation of luminescence. For weak pumping (less than 50 μW), the interwell excitons are strongly localized because of small-scale fluctuations of a random potential, and the corresponding photoluminescence line is inhomogeneously broadened (up to 2.5 meV). As the resonant excitation power increases, the line due to the delocalized excitons arises in a thresholdlike manner, after which its intensity linearly increases with increasing pump power, narrows (the smallest width is 350 μeV), and undergoes a shift (of about 0.5 μeV) to lower energies, in accordance with the filling of the lowest state in the domain. With a rise in temperature, this line disappears from the spectrum ($T_c \leq 3.4$ K). The observed phenomenon is attributed to Bose–Einstein condensation in a quasi-two-dimensional system of interwell excitons. In the temperature range studied (1.5–3.4 K), the critical exciton density and temperature increase almost linearly with temperature. © *2002 MAIK "Nauka/Interperiodica"*.

PACS numbers: 73.21.Fg; 73.20.Mf

**1.** Since a hydrogen-like exciton in a semiconductor consists of two fermions (electron and hole), its spin is an integer, and, hence, it is a composite Bose particle. This gives grounds to assume, as was formulated in a number of theoretical works in early 1960s [1], that, at sufficiently low temperatures, Bose–Einstein condensation (BEC) may occur in a weakly nonideal and low-density exciton gas in semiconductors ($na_{\text{ex}}^d \ll 1$, where $n$ is the exciton density, $a_{\text{ex}}$ is the electron Bohr radius, and $d$ is the system dimensionality). In recent years, much effort has been devoted to a search for excitonic BEC in two-dimensional (2D) systems based on semiconducting heterostructures [2–18]. In an ideal and unconfined 2D system, where the single-particle density of states is constant, BEC cannot occur at finite temperatures for fundamental reasons, namely, because the number of occupied states diverges when $\mu \longrightarrow 0$ and because of the fluctuations that destroy the order parameter [19]. However, in the spatially confined quasi-two-dimensional and 2D systems, BEC may occur at finite temperatures. The critical temperature in the laterally confined 2D system, where the number of states is finite, is equal to

$$T_c \approx n\hbar^2 N_{\text{ex}}/k_B m_{\text{ex}} \ln(N_x S); \qquad (1)$$

i.e., it decreases logarithmically with an increase in the area $S$ occupied by a 2D gas of Bose particles with density $N_{\text{ex}}$ and the effective mass $m_{\text{ex}}$; $k_B$ is the Boltzmann constant.

The spatial confinement in the quantum-well (QW) plane may be due to the large-scale fluctuations of a random potential caused by the variations $w(r)$ of the QW width at the heteroboundaries. These variations give rise to the variations of the effective lateral potential $U(r) = U(w(r))$ [14]. At quasiequilibrium, the exciton density distribution is determined from the equation $\mu(N(r)) + U(r) = \mu$, where the chemical potential $\mu$ of the interwell excitons is determined by their mean density, and $\mu(N)$ is the chemical potential of the homogeneous excitonic phase in the spatial confinement domain. Evidently, $|\mu(r)| < |\mu|$, because $\mu(N) = -|E_{\text{ex}}| + |\delta(U(r))|$ ($E_{\text{ex}}$ is the exciton binding energy), so that excitons are more easily accumulated in the lateral confinement domains, where, hence, the exciton density may be appreciably higher than the mean density in the QW planes [14]. For this reason, the critical conditions for the Bose condensation of interwell excitons can be created more easily precisely in the lateral domains.

With this in mind, we studied the properties of interwell excitons at various densities and temperatures in

double quantum wells (DQW) GaAs/AlGaAs with large-scale fluctuations of random potential. The fluctuations at the QW heteroboundaries were produced using the epitaxial growth interruption technique [20]. By applying bias to DQW and, hence, tilting the bands, one can create excitons whose electron and hole occur in different quantum wells, which are separated by a transparent tunnel barrier. Such excitons are called spatially indirect or interwell excitons (IWE), as opposed to direct intrawell excitons, whose electron and hole are located in the same QW. Compared to intrawell excitons, interwell excitons are long-lived, because the overlap of their electron and hole wave functions through the tunnel barrier is weaker than in intrawell excitons. As a result, interwell excitons can easily be accumulated and cooled to a rather low temperature. The dipole moment of the interwell excitons is nonzero even in the ground state, so that they are not bound into molecules because of dipole–dipole repulsion.

The *n–i–n* GaAs/AlGaAs heterostructure with double quantum wells GaAs/AlAs/GaAs (120-Å-thick GaAs wells and ~11-Å AlAs barrier) was studied. The structure was grown by molecular-beam epitaxy on a doped *n*-type GaAs substrate (concentration of Si dopants was $2 \times 10^{18}$ cm$^{-3}$) with the (001) crystallographic orientation. A 0.5-μm Si-doped ($2 \times 10^{18}$ cm$^{-3}$) GaAs buffer layer was first grown on the substrate. Then an isolating 20 nm-thick $Al_xGa_{1-x}As$ ($x = 0.35$) layer and a 10-period superlattice $AlAs/Al_xGa_{1-x}As$ ($x = 0.35$) with a period of 3 nm were applied. Next, a GaAs/AlAs/GaAs DQW was grown and an isolating 120-nm $Al_xGa_{1-x}As$ ($x = 0.35$) layer containing a 10-period superlattice $AlAs/Al_xGa_{1-x}As$ ($x = 0.35$) with a period of 3 nm was applied again. Next was a 0.1-μm Si-doped ($2 \times 10^{18}$ cm$^{-3}$) GaAs layer. The whole structure was capped by a 100-Å GaAs layer. Metallic contacts made from a Cr/Ge/Au/Cr/Au alloy were attached to the buffer layer and the doped layer at the upper part of the mesa.

At the surface of the *n–i–n* structure with the above architecture, a 120-nm metal mask (aluminum film) with holes (up to 0.5 μm in diameter) was formed by lift-off electron-beam lithography. The excitation and recording of the luminescence signal were accomplished through these windows. The aluminum film was not in contact with the doped $n^+$-contact region of the heterostructure.

The results pointing to the exciton condensation were obtained upon optical excitation of the sample through the windows with diameters less than one micron. Experiments were carried out under conditions of laser resonance excitation of intrawell excitons on heavy holes (1*s*HH excitons) using a tunable Ti– sapphire laser. In all measurements, the size of the laser spot focused onto the sample did not exceed 20 μm. The luminescence spectra of interwell excitons (*I*) measured at various biases are shown in Fig. 1. The optical transitions of interest are schematically illustrated in Fig. 1b. In the intrawell luminescence range (not shown in the figure), two lines are seen at zero bias: due to a free exciton on a heavy hole 1*s*HH and to a bound exciton [9]. The interwell exciton line (*I* line) appears in the spectra when the bias-induced Stark shift of the size-quantization bands in the neighboring quantum wells is such that $eF\Delta(z) \geq E_D - E_I$ ($E_D$ and $E_I$ are the binding energies of the intra- and interwell excitons, respectively, and $F$ is the electric field). The *I*-line shift depends almost linearly on the electric field (Fig. 1c). At large voltages ($U > 0.3$ V) and stationary excitation, the IWE line dominates, while the luminescence of the intrawell excitons and charged excitonic complexes under the same conditions is several orders of magnitude less intense. In the structures studied, the IWE luminescence quantum yield is high and the radiationless transitions can be ignored. This statement is based on the fact that, as the voltage applied increases, the IWE lifetimes change by more than an order of magnitude, whereas the luminescence intensity virtually does not change (Fig. 1).

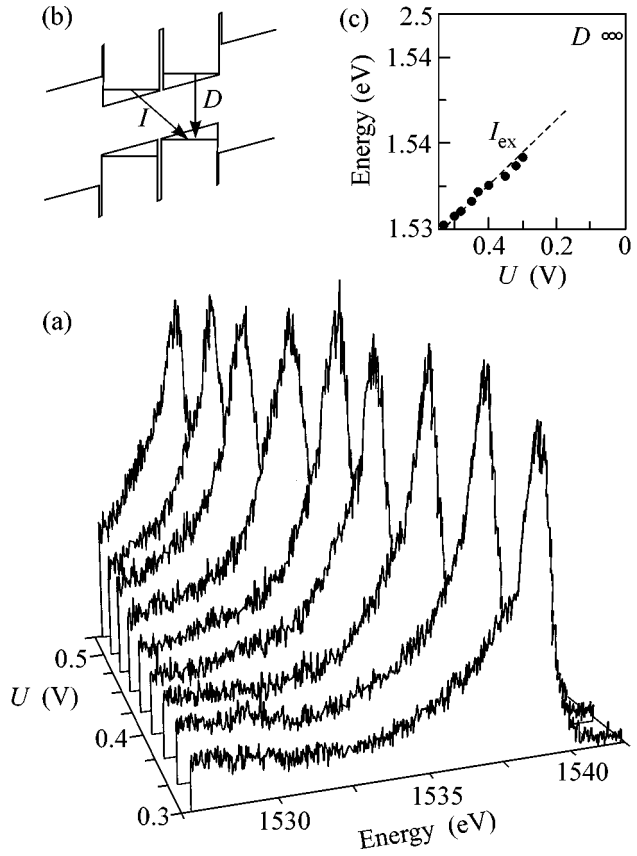


**Fig. 1.** (a) Luminescence spectra of interwell excitons for various applied voltages. Temperature $T = 1.51$ K and optical excitation power $P = 300$ μW. (b) Scheme of optical transitions. (c) Line positions in the spectra of (*D*) direct exciton and ($I_{ex}$) IWE vs. applied bias.

At low excitation power (lower than 50 μW), a moderately broad asymmetric band (with a width of about

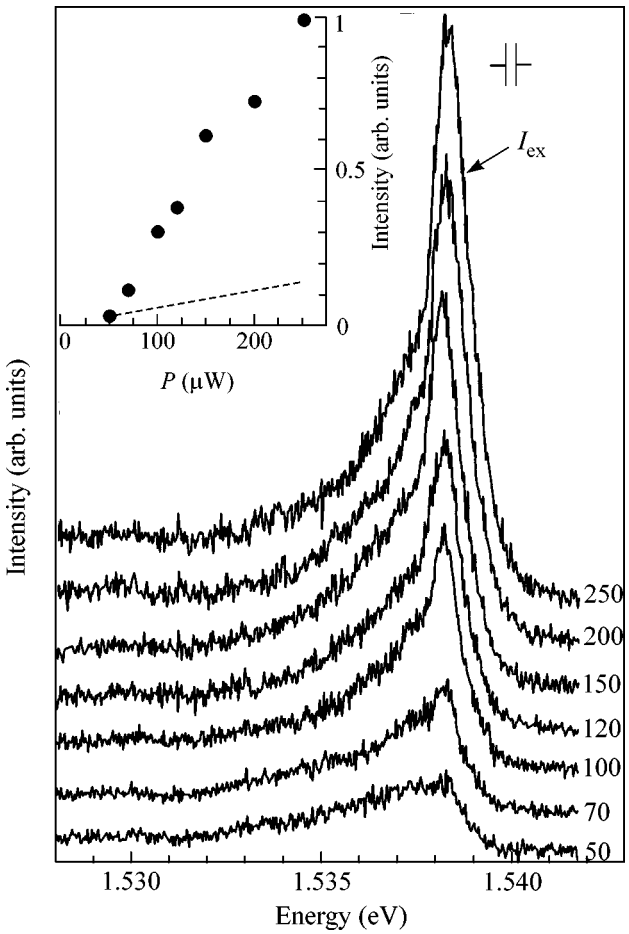


**Fig. 2.** Photoluminescence spectra of the interwell exciton ($I_{ex}$ line) under conditions of resonance excitation of the direct 1*s*HH exciton for various excitation powers, bias $U$ = 0.3 V, and $T$ = 1.51 K. The numbers to the right of the spectra indicate the excitation power in μW. The spectral resolution of the instrument is shown at the top right. Inset: the IWE line intensity (dots) vs. optical excitation power. The dashed line is the extrapolation of the linear dependence of the background intensity.

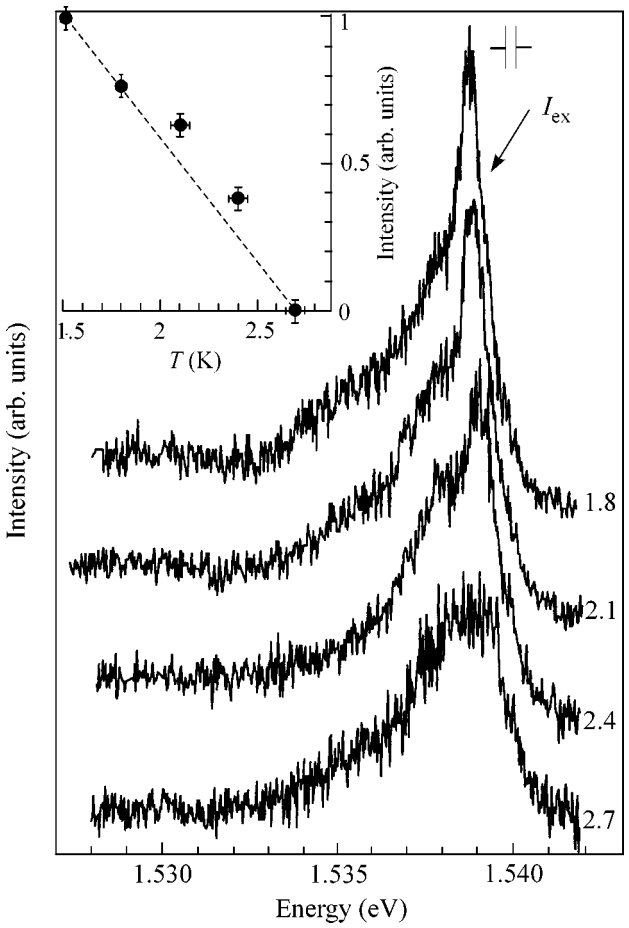


**Fig. 3.** Temperature dependence of the IWE line intensity for the excitation power $P$ = 150 μW and the bias $U$ = 0.3 V. The numbers to the right indicate the temperature in K. Dots in the inset show the temperature behavior of the IWE line intensity, and the dashed line is the extrapolation of the $I_T \propto (1 - T/T_c)$ dependence.

2.5 meV; see Fig. 2) of the interwell excitons is observed in the spectra. This band is inhomogeneously broadened and is due to the strong localization of interwell excitons in the small-scale fluctuations of a random potential created by the residual charged impurities. As the pump increases (≥50 μW), a narrow line appears in a threshold manner at the violet side of the broad band. The intensity of this line linearly increases with pump power (see inset in Fig. 2). It increases much faster than its luminescence background; simultaneously, the line slightly narrows and shifts by approximately 0.5 meV to lower energies. The smallest measured width of this line is 350 μeV. Considering that the spectral width of the spectrometer slit is 250 μeV, one can state that the actual width of this line is smaller than 250 μeV. Note that the structureless background also linearly increases with an increase in pump power. Upon further increase in pumping (higher than 0.5 mW), the narrow IWE line starts to broaden, after which it gradually broadens and shifts to higher energies.

Temperature studies showed that the narrow IWE line disappears at $T \geq 3.4$ K. Figure 3 illustrates the typical temperature behavior of the *I* line at a fixed pumping level. One can see that, at $T$ = 1.8 K and an excitation power of 150 mW, this line rises above the structureless luminescence band of localized excitons and has a high intensity. As the temperature increases, the intensity of *I* line decreases in a nonactivation manner, its width changes only slightly, and at $T$ = 2.7 K it disappears on the background of the structureless spectrum of localized excitons, which retains its shape. Measurements of the temperature behavior of the *I*-line intensity in the temperature range $T$ = 1.51–3.4 K at

various pump powers established that the temperature behavior of this line obeys the law

$$I_T \propto (1 - T/T_c), \quad (2)$$

where $I_T$ is the line intensity at temperature $T$, and $T_c$ is the critical temperature corresponding to the disappearance of the line at a fixed pumping level.

We believe that the experimental results presented above are indicative of the Bose condensation of interwell excitons in a single less-than-micron-sized lateral domain whose origin is associated with the large-scale fluctuations of the random potential. At low pumping levels and low temperatures, the photoexcited IWEs are strongly localized at the small-scale defects (e.g., residual charged impurities). This gives rise to a broad inhomogeneous IWE luminescence band at low excitation powers. Due to the strong dipole–dipole repulsion, only one exciton can be localized at a defect, so this luminescence channel is saturated rather rapidly. In the structures studied, this occurs at concentrations lower than $5 \times 10^9$ cm$^{-2}$. On a further increase in pump power (above the percolation threshold), the interwell excitons become delocalized. On achieving critical density, excitons condense into the lowest delocalized state. Experimentally, this is manifested by the thresholdlike appearance of a narrow luminescence line, its narrowing with an increase in pumping, and its shift to lower energies, in accordance with the fact that excitons obey the Bose–Einstein statistics and fill the lowest state in the domain. The critical temperature behavior of the observed properties is the strongest argument in favor of the exciton condensation.

Bose condensation in the structures studied is observed in a limited range of exciton concentrations: $N_{\text{loc}} < N_{\text{exc}} < N_{I-M}$. The lower limit (low densities) is due to the strong localization of excitons at the domain defects ($N_{\text{loc}} \approx 5 \times 10^9$ cm$^{-2}$), and the upper limit $N_{I-M}$ (high densities) is due to exciton destruction as a result of the isolator–metal transition. Indeed, as the excitation power exceeds 0.5 mW, the IWE luminescence line starts to broaden, whereupon it continues broadening and shifts to higher energies. The broadening of the $I$ line is due to the overlap between the exciton wave functions and to the arisen Fermi repulsion between electrons in one well and holes in the other. The estimates made for the density at which the interwell excitons lose their individuality to form *e–h* plasma with electrons and holes spatially separated in the neighboring quantum wells give $N_{I-M} \approx 8 \times 10^{10}$ cm$^{-2}$. A dimensionless parameter corresponding to this density is $r_s = 1/(\sqrt{\pi N_{I-M}}\, a_B) = 1.8$ (the exciton Bohr radius $a_B$ = 150 Å was determined from the diamagnetic shift of the interwell exciton). The arisen *e–h* plasma starts to screen the external electric field, and the interwell-recombination band starts to move toward higher energies. This fact can be used to determine the *e–h* density. Note that, in the case of micron-sized domains, the number of excitons in the condensate is on the order of several hundred.

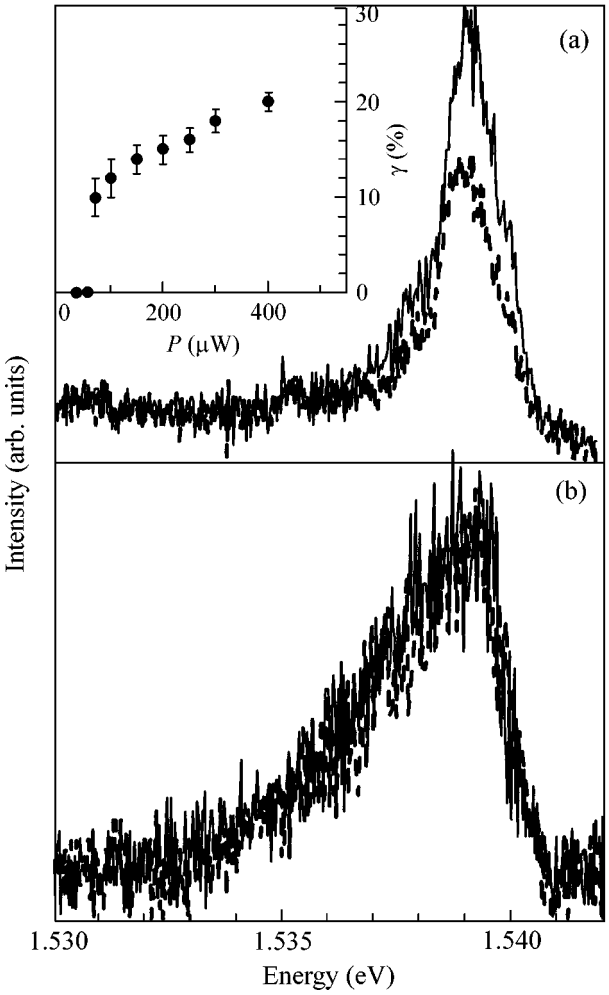


**Fig. 4.** The IWE photoluminescence spectra for the resonance excitation of the intrawell 1sHH exciton by a circularly polarized light ($\sigma^+$) with a power of (b) 50 and (a) 500 μW. Solid lines are for the measured intensity of $\sigma^+$ polarization, and dashed lines are for $\sigma^-$ polarization. Inset: the degree γ of circular polarization (dots) vs. excitation power for the resonance excitation at the line maximum; the contribution from the structureless background was not taken into account. Temperature $T$ = 1.51 K and bias $U$ = 0.3 V.

The condensed excitons must be spatially coherent. The spatial coherence should appear at least on the scale of thermal de Broglie wavelength $\lambda_{\text{ex}}$ of interwell excitons. At $T$ = 2 K, one has $\lambda_{\text{ex}} = h/\sqrt{\pi m_{\text{exc}} kT} = 1.5 \times 10^3$ Å, which is an order of magnitude larger than the exciton Bohr radius. Since the excitons should be in phase on the spatial coherence scale, the radiative decay rate of the excitons in the condensate may increase. To verify this, experiments on the resonance excitation of excitons by a circularly polarized light

were conducted. Recall that the ground state of the interwell exciton is not a Kramers doublet but is fourfold degenerate with respect to the projections of the angular momentum $M = \pm 1, \pm 2$ (only the $M = \pm 1$ states are optically active). The resonance excitation of the intrawell 1*s*HH excitons by a circularly polarized light resulted in a sharp increase in the degree of circular polarization of the narrow IWE line (Fig. 4). This effect is evidence that the radiative recombination rate of the excitons in the condensate substantially increases compared to the recombination rate of the localized incoherent excitons. We assume that the spin relaxation rate does not change appreciably in this case. A high degree (about 30%) of circular polarization obtained experimentally for the *I* line points also to the fact that the optical excitation can be used to create coherent vortical states of interwell excitons.

We are grateful to G.M. Éliashberg and S.V. Iordanskiĭ for discussions. This work was supported by the Russian Foundation for Basic Research (project nos. 01-02-16471, 02-02-06349, 02-02-16791) and, in part, by the State Scientific and Technical Program of FTNS on nanostructures.

## REFERENCES

1. S. A. Moskalenko, Fiz. Tverd. Tela (Leningrad) **4**, 276 (1962) [Sov. Phys. Solid State **4**, 199 (1962)]; I. M. Blatt, K. W. Boer, and W. Brandt, Phys. Rev. **126**, 1691 (1962); R. S. Casella, J. Appl. Phys. **34**, 1703 (1963).
2. Yu. E. Lozovik and V. I. Yudson, Pis'ma Zh. Éksp. Teor. Fiz. **22**, 556 (1975) [JETP Lett. **22**, 274 (1975)].
3. T. Fukuzawa, E. E. Mendez, and J. M. Hong, Phys. Rev. Lett. **64**, 3066 (1990).
4. J. E. Golub, K. Kash, J. P. Harbison, and L. T. Flores, Phys. Rev. B **41**, 8564 (1990).
5. L. V. Butov, A. Zrenner, G. A. Abstreiter, *et al.*, Phys. Rev. Lett. **73**, 304 (1994); L. V. Butov, in *Proceedings of the 23rd International Conference on Physics of Semiconductors, Berlin, 1996.*
6. V. B. Timofeev, A. V. Larionov, A. S. Ioselevich, *et al.*, Pis'ma Zh. Éksp. Teor. Fiz. **67**, 580 (1998) [JETP Lett. **67**, 613 (1998)].
7. V. V. Krivolapchuk, E. S. Moskalenko, A. L. Zhmodikov, *et al.*, Solid State Commun. **111**, 49 (1999).
8. L. V. Butov, A. Imamoglu, A. V. Mintsev, *et al.*, Phys. Rev. B **59**, 1625 (1999).
9. A. V. Larionov, V. B. Timofeev, J. M. Hvam, and K. Soerensen, Zh. Éksp. Teor. Fiz. **117**, 1255 (2000) [JETP **90**, 1093 (2000)].
10. L. V. Butov, A. V. Mintsev, Yu. E. Lozovik, *et al.*, Phys. Rev. B **62**, 1548 (2000).
11. A. V. Larionov, V. B. Timofeev, J. M. Hvam, and K. Soerensen, Pis'ma Zh. Éksp. Teor. Fiz. **75**, 233 (2002) [JETP Lett. **75**, 200 (2002)].
12. D. Yoshioka and A. H. MacDonald, J. Phys. Soc. Jpn. **59**, 4211 (1990).
13. X. M. Chen and J. J. Quinn, Phys. Rev. Lett. **67**, 895 (1991).
14. Xuejun Zhu, P. L. Littlewood, M. S. Hybersten, and T. Rice, Phys. Rev. Lett. **74**, 1633 (1995).
15. J. Fernández-Rossier and C. Tejedor, Phys. Rev. Lett. **78**, 4809 (1997).
16. Yu. E. Lozovik and O. L. Berman, Zh. Éksp. Teor. Fiz. **111**, 1879 (1997) [JETP **84**, 1027 (1997)].
17. Yu. E. Lozovik and I. V. Ovchinnikov, Pis'ma Zh. Éksp. Teor. Fiz. **74**, 318 (2001) [JETP Lett. **74**, 288 (2001)].
18. V. B. Timofeev, A. V. Larionov, M. Grassi Alessi, *et al.*, Phys. Rev. B **60**, 8897 (1999).
19. P. C. Hoenberg, Phys. Rev. **158**, 383 (1967).
20. S. W. Brown, T. A. Kennedy, D. Gammon, *et al.*, Phys. Rev. B **54**, R17339 (1996).

*Translated by V. Sakun*

JETP Letters, Vol. 75, No. 11, 2002, pp. 575–578. Translated from Pis'ma v Zhurnal Éksperimental'noĭ i Teoreticheskoĭ Fiziki, Vol. 75, No. 11, 2002, pp. 695–698.


# Spin-Reorientation Phase Transition on the Surface and in the Bulk of $\alpha$-$Fe_2O_3$ Single Crystals

**A. S. Kamzin and D. B. Vcherashnii**

*Ioffe Physicotechnical Institute, Russian Academy of Sciences, ul. Politekhnicheskaya 26, St. Petersburg, 194021 Russia*

*e-mail: Kamzin@spb.cityline.ru.*

Received May 6, 2002

Direct comparison of the properties of a thin surface layer and the bulk of macroscopic hematite ($\alpha$-$Fe_2O_3$) crystals was used to study the magnetic structure of the surface layer and the bulk and the processes attendant on spin-reorientation phase transition (SRT). The investigation tool was simultaneous $\gamma$-ray, X-ray, and electronic Mössbauer spectroscopy, which enabled us to study the bulk and surface properties of macroscopic samples simultaneously and to compare them directly. Direct evidence of the existence of a surface "transition layer" on hematite crystals is obtained. The existence of this layer was suggested and described by Krinchik and Zubov [JETP **69**, 707 (1975)]. The study in the SRT region showed that (1) the Morin SRT in the crystal bulk occurs in a jump (as a first-order phase transition), whereas in the surface layer of about 200 nm thick, some smoothness appears in the mechanism of magnetic-moment reorientation; (2) SRT in the surface layer, as in the bulk, involves an intermediate state in which low- and high-temperature phases coexist; and (3) SRT in the surface layer occurs at a temperature several degrees higher than in the bulk. Our experimental evidence on the SRT mechanism in the surface layer correlates with the inferences from phenomenological theory developed by Kaganov [JETP **79**, 1544 (1980)]. © *2002 MAIK "Nauka/Interperiodica".*

PACS numbers: 75.30.Kz; 75.70.-i

Surface effects on the properties of a near-surface layer of macroscopic crystals have been receiving systematically growing attention since the late 1960s. Of special interest are processes occurring in the surface layers of a macrocrystal and attendant to fundamental phenomena such as phase transitions in the bulk of the sample. The first theoretical descriptions of the behavior of the surface layer in the region of critical transitions at the Curie or Néel points [1, 2] were followed by numerous theoretical and experimental studies of the surface properties upon these transitions (see [3–5] and references quoted therein). Surface processes in macrocrystals attendant on phenomena such as spin-reorientation phase transitions (SRTs) are understood far less well.

SRTs in the surface layer of crystals were first studied on powdered samples, because the surface in such objects substantially dominates over the bulk. No difference (to within a measurement error of about 5) between the SRT temperatures on the surface and in the bulk was observed in $\alpha$-$Fe_2O_3$ powders [6].

Studies on macroscopic $ErFeO_3$ [7] and $TbFeO_3$ [8] single crystals showed that the onset spin reorientation temperature in the surface layer is about 40 K higher than in the bulk. Spin reorientation of the $G_xF_z \longleftrightarrow G_zF_x$ type in the bulk of $TbFeO_3$ transforms to the Morin transition $G_xF_z \longleftrightarrow G_y$ in the surface layer [9]. Mössbauer studies on $\alpha$-$Fe_2O_3$ single crystals showed that SRT in the surface layer shifts in temperature by several degrees compared to the bulk transition [10]. Simultaneous investigations of the surface and bulk properties were carried out on macroscopic $Fe_3BO_6$ crystals [11]; $Fe_3BO_6$ is also an antiferromagnet with weak ferromagnetism. The boundaries of the SRT widen as they approach the crystal surface; however, the middle point of the SRT region does not shift [11]. In the bulk, magnetic moments change their orientation in a jump; the moment reorientation is progressively smoothed in proportion to proximity to the surface. Outside the SRT region, there is a layer on the $Fe_3BO_6$ surface in which magnetic moments are not collinear to the moments in the crystal bulk [11]. When iron ions in $Fe_3BO_6$ are 7.5% replaced by diamagnetic gallium ions to yield $Fe_{2.75}Ga_{0.25}BO_6$, the SRT temperature is insignificantly reduced, but the reorientation mechanism of magnetic moment both in the bulk and on the surface is conserved [12]. Experimental evidence [11, 12] correlates with the inferences from phenomenological theory concerning SRTs on the surface of semi-infinite (macroscopic) crystals developed by Kaganov [13]. Kaganov [13] was the first to describe the forms of a temperature hysteresis loop for an SRT occurring on the surface of macrocrystals for various orientations of the easy axis on the surface in the case of a first- or second-order SRT in the bulk of a magnet.

0021-3640/02/7511-0575$22.00 

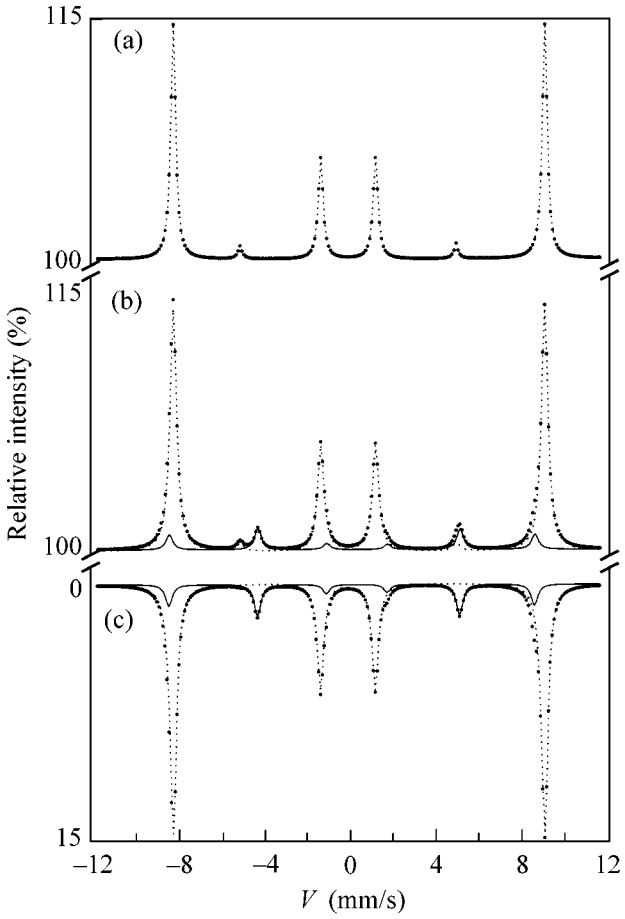


**Fig. 1.** Mössbauer spectra of $\alpha$-$Fe_2O_3$ measured in the SRT region at 242.6 K with detecting (a) $\gamma$-ray quanta and (b, c) conversion and Auger electrons, that is, recorded from the crystal bulk and surface layers 0 to 100 nm and 100 to 200 nm thick, respectively. An observed spectrum is presented by a dotted line. The spectrum due to the phase observed at temperatures above SRT is shown by a solid line; the spectrum due to the phase observed at temperatures below SRT, by a dashed line.

The experimental evidence is clearly insufficient to compare with the theoretical data and is controversial. In addition, the aforementioned data [7, 8, 10] were obtained from rather thick surface layers (of several hundreds of nanometers); the properties of these layers can be similar to the bulk properties of a crystal. In view of the above, we intended to study SRT in the surface layer up to about 100 nm thick of macroscopic hematite crystals (the chemical formula is $\alpha$-$Fe_2O_3$).

In choosing hematite, we were guided by the simplicity of its magnetic structure. The iron ions of this compound occupy one crystallographic position, and Mössbauer spectra in the magnetically ordered region are a single Zeeman sextuplet. The good resolution of the lines of this sextuplet enables a high accuracy in the analysis of observed Mössbauer spectra. In addition, the bulk properties of hematite are well studied by various methods, including Mössbauer effect measurements [14–16, references therein], which allows us to compare experimental evidence concerning the bulk properties obtained in this study with the related literature.

At temperatures below the Néel point (~960 K), hematite is an antiferromagnet with a weak ferromagnetic moment. The magnetic moments of iron ions are located in a plane perpendicular to the *c* axis. Upon reduction in temperature, the Morin SRT $G_xF_z \longleftrightarrow G_y$ is observed in the region of ~260 K. Magnetic moments become oriented along the *c* axis in the course of this transition, and the weak ferromagnetic moment disappears. Spin reorientation in hematite occurs over a rather wide temperature range of about 10 K.

The investigation tool was simultaneous $\gamma$-ray, X-ray, and electronic Mössbauer spectroscopy (SGXEMS) described elsewhere [17]. This method is based on the simultaneous record of Mössbauer spectra with the detection of radiations having various mean free paths in the substance, namely, $\gamma$-ray quanta (GQ), characteristic X-ray radiation, and conversion and Auger electrons (CAE). The Morin transition in hematite occurs at below room temperatures (ca. 260 K). We adapted SGXEMS for use at temperatures from 300 to 10 K with the temperature maintained accurate to $\pm$1.5 K [18]. The use of this method enabled us to study the bulk properties and the properties of surface layers several microns thick and up to about 300 nm thick on macroscopic crystals simultaneously under the same conditions (under which a test sample is kept).

The $\alpha$-$Fe_2O_3$ single crystals were flux-grown. The grown crystals had a natural concentration of $^{57}$Fe or 100% $^{57}$Fe. Platelets 10 mm in diameter and 50 $\mu$m thick were cut from the single crystals. X-ray diffraction measurements showed that the *c* axis was directed normal to the plane of the platelets. In Mössbauer studies, the *c* axis of the plates was oriented parallel to the wave vector of the incident $\gamma$-rays with an accuracy better than 1°. The quality of the test surface was given special attention in crystal preparation. Previous experiments [19] showed that chemical polishing in orthophosphoric acid at 90°C for 1 min could provide a high-quality surface.

Mössbauer spectra measured at temperatures below or above the SRT region consist of Zeeman lines due to iron ions in one magnetically equivalent position. The GQ and CAE spectra recorded at 242.6 K are shown in Fig. 1. The positions of the Zeeman lines corresponding to different phases are shown by dashed lines. In the SRT region, the measured spectra are a superposition of the spectra observed below and above SRT. The spectral lines from different phases in the SRT region are well resolved, which allows the behavior of magnetic moments to be studied for each phase.

Analysis of the measured spectra showed that the line from the phase observed above SRT is reduced in intensity, as temperature decreases within the SRT

region, to disappear at some temperature. The phase observed below SRT grows in intensity from zero to a maximal value as temperature decreases.

From the intensity ratio of the first and second (fifth and sixth) lines of the Zeeman sextuplets and using the relationship

$$\theta = \arccos\left(\frac{4A_{1.6} - 3A_{2.5}}{4A_{1.6} + 3A_{2.5}}\right)^{1/2} = \arcsin\left(\frac{(3/2)A_{2.5}/A_{1.6}}{1 + (3/4)A_{2.5}/A_{1.6}}\right)^{1/2}, \quad (1)$$

(for example, [10]), we found the θ angles, which control the direction of magnetic moments relative to the wave vector of γ rays. Figure 2 plots θ versus temperature curves calculated from the observed γ-ray quanta and CAE spectra, that is, from the bulk and surface layers of the hematite crystal.

The θ angle as determined from Mössbauer spectra with detection of γ-ray quanta carrying information about the bulk properties of a crystal acquires either of the two values: 0 or π/2 (Fig. 2). This is made clear by the GQ spectrum of Fig. 1a, in which the intensity ratio for the Zeeman sextuplet observed at above SRT is 3 : 4 : 1 : 1 : 4 : 3. The intensity ratio for the sextuplet from the phase observed below SRT is 3 : 0 : 1 : 1 : 0 : 3 (Fig. 1a). Because the wave vector of incident γ rays is directed along the *c* axis, this means that the magnetic moments positioned in the crystal bulk at temperatures above and below SRT are located in a plane normal to the *c* axis and along the *c* axis, respectively. Within the temperature window of SRT, these two phases coexist. This is convincing evidence that spin reorientation in the bulk of an α-$Fe_2O_3$ crystal occurs as a first-order phase transition to yield an inhomogeneous state in the range of temperatures from $T_1$ to $T_2$, in agreement with the related literature [14–16].

The values and temperature dependences of θ as calculated from the Mössbauer spectra that were measured from surface layers differ from those observed in the crystal bulk (Fig. 2). At temperatures above or below the SRT region, magnetic moments in the surface layers deviate from the directions in which they are oriented in the bulk (Fig. 2). The deviation of the θ angle increases in proportion to proximity to the surface of the sample. This is made clear by the CAE spectra (Fig. 1): the spectra display second and fifth lines of the Zeeman sextuplet with the intensities increasing as the test layer approaches the surface (Figs. 1b, 1c). Experimental evidence from outside the SRT region shows a "transition" layer in the surface layer of macroscopic hematite crystals in which magnetic moments are oriented differently than in the bulk. Such a transition layer was first discovered using magnetooptical methods [20].

Within the SRT region, the magnetic moment deviation angles of iron ions located in the surface layer are slightly variable, whereas the moments of the iron ions positioned in the bulk acquire only a value of 0 or π/2

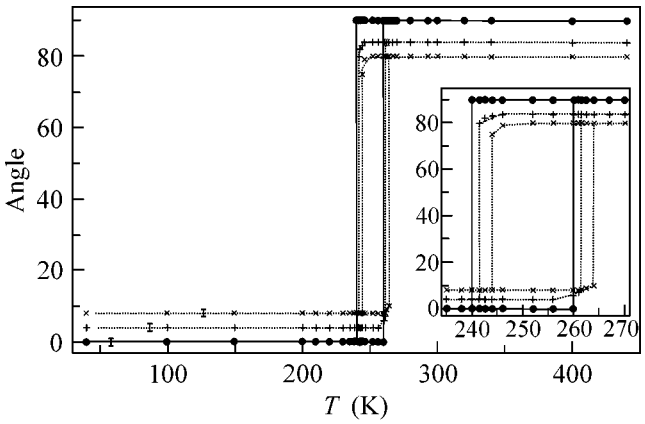


**Fig. 2.** Plots of the deviation angle θ of iron-ion magnetic moments versus temperature as derived from observed Mössbauer spectra of α-$Fe_2O_3$ for surface layers (×) 0 to 100 and (+) 100 to 200 nm thick and for (•) crystal bulk.

(Fig. 2). Magnetic moment reorientation in the surface layer ends in a jump. The temperature window of SRT both in the bulk and the surface layer has the same width (Fig. 2). With approach to the surface, the SRT region shifts to higher temperatures. This result is inconsistent with evidence from fine hematite powders [5] but coincides with the inferences made from the investigations of SRT in the surface layer of $ErFeO_3$ [6], $TbFeO_3$ [7], and α-$Fe_2O_3$ [10] macroscopic crystals.

The comparison of our experimental results for the SRT mechanism in the surface layer of a crystal with theoretical investigations has shown that experimental evidence combines two cases described in [13]. One case is where the jumped character of magnetic moment reorientation in the crystal bulk (a first-order transition) is smoothed toward the surface. Experimental curves (Fig. 2) in the SRT region also show some smoothness in the variation of magnetic moment orientation in the surface layer. The other theoretical case with which experimental evidence coincides is where the SRT boundaries on the surface are shifted compared to the reorientation transition boundaries in the bulk [13].

This work was supported by the Russian Foundation for Basic Research, project no. 01-02-17889.

## REFERENCES

1. M. I. Kaganov, Zh. Éksp. Teor. Fiz. **62**, 1190 (1972) [Sov. Phys. JETP **35**, 631 (1972)].
2. D. Mills, Phys. Rev. B **3**, 3887 (1971).
3. M. I. Kaganov and V. A. Chubukov, in *Magnetic Properties of Crystalline and Amorphous Media* (Nauka, Novosibirsk, 1989), p. 135.
4. H. W. Diehl, J. Mod. Phys. B **11**, 3503 (1997).
5. A. S. Kamzin and L. A. Grigor'ev, Zh. Éksp. Teor. Fiz. **105**, 377 (1994) [JETP **78**, 200 (1994)].
6. T. Shinjo *et al.*, J. Magn. Magn. Mater. **35**, 133 (1983).

7. E. A. Balykina, E. A. Gan'shina, and G. S. Krinchik, Zh. Éksp. Teor. Fiz. **93**, 1879 (1987) [Sov. Phys. JETP **66**, 1073 (1987)].
8. E. A. Balykina, E. A. Gan'shina, and G. S. Krinchik, Fiz. Tverd. Tela (Leningrad) **30**, 570 (1988) [Sov. Phys. Solid State **30**, 326 (1988)].
9. V. N. Derkachenko, A. M. Kadomtseva, *et al.*, in *Proceedings of the All-Union Conference on Physics Low Temperature, LT-19, 1976*, p. 594.
10. O. Nikolov, T. Ruskov, and T. Tomov, Hyperfine Interact. **39**, 409 (1988).
11. A. S. Kamzin and L. A. Grigor'ev, Pis'ma Zh. Éksp. Teor. Fiz. **57**, 543 (1993) [JETP Lett. **57**, 557 (1993)]; Zh. Éksp. Teor. Fiz. **104**, 3489 (1993) [JETP **77**, 658 (1993)].
12. A. S. Kamzin and L. A. Grigor'ev, Fiz. Tverd. Tela (Leningrad) **18**, 2795 (1976) [Sov. Phys. Solid State **18**, 1631 (1976)].
13. M. I. Kaganov, Zh. Éksp. Teor. Fiz. **79**, 1544 (1980) [Sov. Phys. JETP **52**, 779 (1980)].
14. F. Wan der Woode, Phys. Status Solidi **17**, 416 (1960).
15. A. P. Salugin, V. A. Povitskiĭ, M. V. Filin, *et al.*, Fiz. Tverd. Tela (Leningrad) **15**, 1227 (1974) [Sov. Phys. Solid State **15**, 792 (1974)].
16. T. Ruskov, T. Tomov, and S. Georgiev, Phys. Status Solidi A **37**, 295 (1976).
17. A. S. Kamzin and L. A. Grigor'ev, Pis'ma Zh. Tekh. Fiz. **16** (16), 38 (1990) [Sov. Tech. Phys. Lett. **16**, 616 (1990)].
18. A. S. Kamzin and D. B. Vcherashniĭ, Pis'ma Zh. Tekh. Fiz. **28** (9), 22 (2002) [Tech. Phys. Lett. **28**, 365 (2002)].
19. A. S. Kamzin, B. Stahl, R. Gellert, *et al.*, Pis'ma Zh. Éksp. Teor. Fiz. **16**, 38 (1999); B. Stahl, E. Kankeleit, R. Gellert, *et al.*, Phys. Rev. Lett. **84** (24), 5632 (2000).
20. G. S. Krinchik and V. E. Zubov, Zh. Éksp. Teor. Fiz. **69**, 707 (1975) [Sov. Phys. JETP **42**, 359 (1975)].

*Translated by O. Fedorova*

JETP Letters, Vol. 75, No. 11, 2002, pp. 579–582. Translated from Pis'ma v Zhurnal Éksperimental'noĭ i Teoreticheskoĭ Fiziki, Vol. 75, No. 11, 2002, pp. 699–702.


# Anisotropy of the Superconducting Transition in Magnetic Fields in a $Nd_{1.85}Ce_{0.15}CuO_4$ Single Crystal

**G. Kh. Panova[1], A. A. Shikov[1], N. A. Chernoplekov[1], G. A. Emel'chenko[2], A. N. Malyuk[2, 3], and S. T. Lin[3]**

[1] *Russian Research Centre Kurchatov Institute, Moscow, 123182 Russia*
[2] *Institute of Solid State Physics, Russian Academy of Sciences, Chernogolovka, Moscow region, 142432 Russia*
[3] *Max-Planck Institut für Festkörperforschung, D-70569 Stuttgart, Germany*
*e-mail: shikov@isssph.kiae.ru*
Received May 6, 2002

The anisotropy of superconducting properties of a $Nd_{1.85}Ce_{0.15}CuO_4$ single crystal is studied by resistance measurements over the temperature range 2–30 K in magnetic fields of 0, 1, 2, 4, and 6 T parallel to the *a*–*b* plane. A strong anisotropy of $T_c(H)$ and $H_{c2}(T)$ is observed for different orientations of magnetic field in the *a*–*b* plane. This anisotropy leads to a twofold symmetry of $T_c(H)$ and $H_{c2}(T)$, and the gap node direction is determined. An analysis of experimental data shows that this result can be attributed to a change in the local symmetry of the copper atom environment, which manifests itself as a reduction from tetragonal to orthorhombic symmetry in the low-temperature region. The comparison with $La_{1.85}Sr_{0.15}CuO_4$ suggests that the mechanisms of superconductivity in electron and hole doped superconductors are similar, and the difference observed in the experiment is related to the structural features of these materials. © *2002 MAIK "Nauka/Interperiodica"*.

PACS numbers: 74.25.Ha; 74.72.-h

The determination of the symmetry of the superconducting order parameter in high-$T_c$ superconductors provides important information on the mechanism of superconductivity, because the structure of the superconducting energy gap is related to the pairing symmetry. The anisotropy of the superconducting order parameter in *d*-wave superconductors leads to a number of characteristic features of their properties, as compared to conventional *s*-type superconductors. These features include the appearance of zero values of the order parameter on the Fermi surface and the anisotropy of vortices and vortex lattice structure in the magnetic fields $H_{c1} < H < H_{c2}$. On the whole, experimental data on the properties of the superconducting state in cuprates [1, 2] show that, in these materials, an anisotropic order parameter is realized with zero gap values at certain points of the Fermi surface and that, in high-$T_c$ superconductors with hole conduction, the superconducting order parameter has a *d*-wave symmetry. For years, it was believed that, in high-$T_c$ superconductors with electron conduction (one of the most studied of which is $Nd_{1.85}Ce_{0.15}CuO_4$), the superconducting order parameter has an *s*-wave symmetry. The results of the tunnel spectroscopy of the $Nd_{1.85}Ce_{0.15}CuO_4$ electron-type superconductor [3] rule out the *d*-wave symmetry for this material. At the same time, the studies of the quasiparticle spectra of excitations in $Nd_{1.85}Ce_{0.15}CuO_4$ single crystals by the STM/STS method [4] and by photoelectron spectroscopy [5] suggest that the superconducting order parameter is anisotropic and has a *d*-wave symmetry. Because of the contradictory data obtained from different experiments, the question of the symmetry of the superconducting order parameter in electron-type superconductors remains open.

In the cited publications, the conclusions were made on the basis of the measurements performed only in three directions in the $CuO_2$ plane: along the *a* or *b* axes and at an angle of 45° to these axes. In a tetragonal lattice, the 45° direction corresponds to the direction of the energy gap node, and the comparison with the results obtained along the *a* or *b* axes allows one to make certain inferences about the symmetry of the superconducting order parameter.

However, a closer examination of the structural features of the $Nd_{1.85}Ce_{0.15}CuO_4$ crystal lattice by neutron powder diffraction [6, 7] revealed considerable anisotropic displacements of the oxygen atoms and the effect of these displacements on the parameters of the crystal lattice. The strong anisotropy of the oxygen displacements observed in the experiment was attributed to changes in the local symmetry of the copper atom environment, which leads to the reduction of symmetry from tetragonal (*I*4/*mmm*) to orthorhombic (*Cmca*). This effect is most likely to be responsible for the discrepancy between the experimental data obtained for $Nd_{1.85}Ce_{0.15}CuO_4$.

The neutron scattering experiments [8] revealed nonmagnetic superstructure peaks located at the points with the coordinates $(\pi, \pi)$ in the reciprocal lattice. These reflections do not belong to the structure of the *I*4/*mmm* space group. This result implies the existence of an atomic displacement that is long-wave in the *a*–*b* plane and short-wave in the perpendicular plane. Since the intensity of the observed peak is about $10^{-3}$–$10^{-4}$ of the fundamental Bragg intensity for X-ray and neutron diffraction studies, atomic displacement occurs not only for oxygen atoms but also for other heavy atoms. Such fine features of the atomic structure can strongly affect the properties of high-$T_c$ superconductors.

To determine the symmetry of the superconducting order parameter in a $Nd_{1.85}Ce_{0.15}CuO_4$ electron-type superconducting single crystal, we studied the anisotropy of the superconducting transition by measuring the resistance in the temperature interval 2–30 K in magnetic fields of 0, 1, 2, 4, and 6 T oriented in the *a*–*b* plane. These measurements allowed us to study the behavior of the temperature and angular dependences of the upper critical magnetic field $H_{c2}$ and the angular and field dependence $T_c(H)$ in the *a*–*b* plane of a high-quality bulk single crystal of $Nd_{1.85}Ce_{0.15}CuO_4$.

**1. Sample preparation and their characteristics.** The $Nd_{1.85}Ce_{0.15}CuO_4$ single crystal under study was prepared by the crucibleless melting technique with radiation heating, as in [9]. We used a four-mirror furnace with 300-W lamps. The initial materials for preparing the feeding and seed rods were $Nd_2O_3$, CuO, and $CeO_2$ powders 99.9–99.99% pure. The crystal growth occurred under oxygen pressure of 0.08 atm at a rate of 0.4–0.8 mm/h along the *a* axis of the Nd–Ce–Cu–O seed crystal. During the growth process, the feeding rod and the growing crystal rotated in opposite directions at a rate of 20–30 rpm to provide an effective mixing and a uniform temperature distribution in the melt zone. The temperature in the melt zone was controlled by setting the current through the lamps.

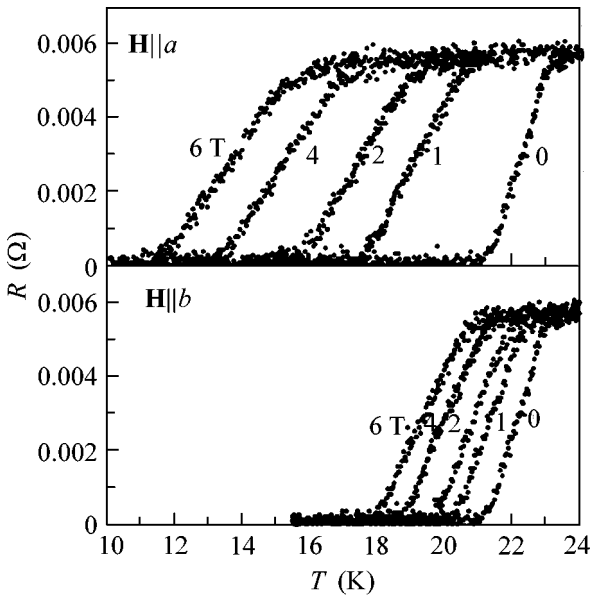


**Fig. 1.** Temperature dependence of the resistance in the superconducting transition region in magnetic fields of 0, 1, 2, 4, and 6 T oriented along the *a*–*b* plane for the cases **H** ∥ *a* and **H** ∥ *b*.

The sample grown in this way was tested for composition and homogeneity by ICP-OES spectroscopy (induction-confined plasma), electron-probe microanalysis (EPMA, Cameca SX100), and X-ray powder diffraction (XRD, Philips PW-3710).

Initially, the resulting $Nd_{1.85}Ce_{0.15}CuO_4$ single crystal was nonsuperconducting and measured 30–40 mm in length and 5 mm in diameter. The X-ray powder diffraction revealed no foreign inclusions. The study with a polarizing optical microscope confirmed that the (10–20)-mm-long terminal part of the crystal contained no other crystallites. The EPMA studies confirmed the homogeneity of the Ce distribution along the growth axis.

The $Nd_{1.85}Ce_{0.15}CuO_4$ single crystal became superconducting after it was annealed in a flow of 99.99%-pure argon at 1030°C during 10–20 h. Such a heat treatment allowed us to obtain a superconducting single crystal with $T_c$ = 21–22 K.

The resistance of the $Nd_{1.85}Ce_{0.15}CuO_4$ single crystal was measured by the four-terminal method with the current along the *a* axis. The sample rotated about the *c* axis in a constant magnetic field that was parallel to the *a*–*b* plane. We denote the angle between the field *H* and the *a* axis in the *a*–*b* plane by θ. The measurements were performed on a plate with dimensions of about $0.7 \times 1.5 \times 4$ mm. The leads were connected to the sample by indium. The current leads were attached at the ends of the sample, and the voltage leads were fixed in the *a*–*b* plane at a distance of ~4 mm from each other. The measuring current was fairly small (1 mA) to provide a linear mode of operation and the absence of hysteresis of the heating and cooling runs. The temperature measurements were performed by a TSKUM carbon resistance thermometer. The accuracy of the temperature measurements was within ±0.01 K in the absence of a magnetic field and ±0.02 K in a field of 6 T. The value of $T_c$ was determined as the midpoint of the resistive superconducting transition. The transitions observed in the experiment were rather narrow, which testified to the high quality of the single crystal.

**2. Experimental results and discussion.** Figure 1 presents the temperature dependence of the resistance $R(T)$ in the superconducting transition region in magnetic fields of 0, 1, 2, 4, and 6 T directed along the *a* and *b* axes. Magnetic fields of both directions shift the transition toward lower temperatures and cause an increase in its width $\Delta T_c$. The shift of $T_c$ with increasing mag-

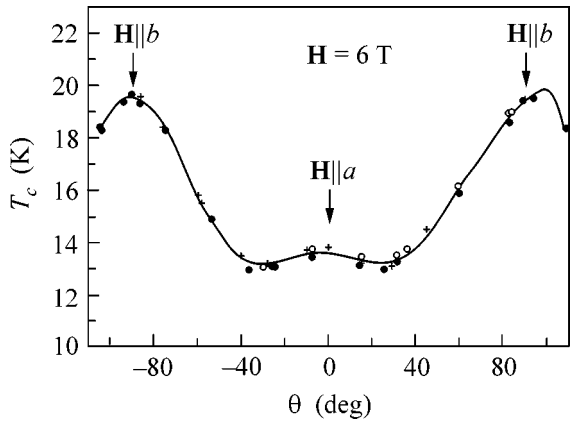


**Fig. 2.** Angular dependence of the superconducting transition temperature $T_c(\theta)$ in a magnetic field of 6 T in the *a*–*b* plane (experiment no. (●) 1, (○) 2, and (+) 3).

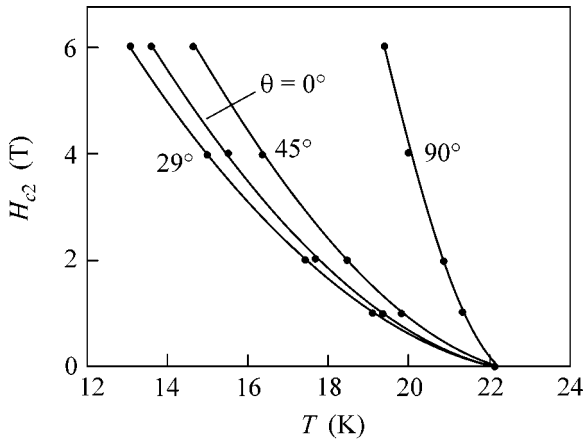


**Fig. 3.** Temperature dependence of $H_{c2}$ obtained from the resistance measurements in magnetic fields of 0, 1, 2, 4, and 6 T with the magnetic field orientation at the angles θ = 0°, 29°, 45°, and 90° to the *a* axis.

netic field is much greater in the case of **H** ∥ *a* than in the case of **H** ∥ *b*, which points to a strong anisotropy of $T_c(H)$ in the *a*–*b* plane and, hence, to the possible orthorhombicity of the lattice.

Figure 2 shows the dependence of the superconducting transition temperature on the angle θ in the *a*–*b* plane, $T_c(\theta)$, in a magnetic field of 6 T. This dependence has a maximum at θ = 90° (**H** ∥ *b*); as the angle θ decreases, the temperature $T_c$ also decreases, and its value at θ = 0° (**H** ∥ *a*) is characterized by the ratio $T_c(90°)/T_c(0°) = 1.4$. The minimum of $T_c(\theta)$ is observed at the angle θ = 29° to the *a* axis, and this angle determines the gap node direction. The observed anisotropy of the angular dependence of the superconducting transition temperature $T_c(\theta)$ in the *a*–*b* plane points to the twofold symmetry of $T_c(\theta)$ in the $Nd_{1.85}Ce_{0.15}CuO_4$ crystal. Our measurements provided the first experimental determination of the gap node direction in $Nd_{1.85}Ce_{0.15}CuO_4$.

Figure 3 displays the temperature dependence of the upper critical field $H_{c2}$ obtained from the superconducting transition measurements in magnetic fields of 0, 1, 2, 4, and 6 T for the field directions making the angles θ = 0°, 29°, 45°, and 90° with the *a* axis. The dependence is nonlinear with a positive curvature. The results of the measurements show a strong anisotropy of $H_{c2}$ in the *a*–*b* plane; $H_{c2}$ is maximal at θ = 90° (**H** ∥ *b*) and minimal at θ = 29°. This indicates not only the strong anisotropy of $H_{c2}$, but also the gap node direction in $Nd_{1.85}Ce_{0.15}CuO_4$.

As a result of our measurements, we observed a strong anisotropy of $T_c(H)$ and $H_{c2}(T)$ for different orientations of magnetic field in the *a*–*b* plane; this anisotropy led to the twofold symmetry of $T_c(H)$ and $H_{c2}(T)$. Another important result is that, at the angle θ = 29° to the *a* axis, the minimal values of $T_c(H)$ and $H_{c2}(T)$ are observed, which corresponds to the gap node direction. These anomalies are presumably related to the change in the local symmetry of the copper atom environment when the symmetry is reduced from tetragonal to orthorhombic in the low-temperature region. (Detailed studies of the local symmetry by the neutron diffraction method were performed on $Nd_{1.85}Ce_{0.15}CuO_4$ samples in [6–8].)

The experimental results obtained by us agree to some extent with the conclusions derived from the theoretical study [10] of the effect of a magnetic field on the electron density *E* of states of an orthorhombic superconductor. In the cited publication, the density of states in a two-dimensional *d*-wave superconductor was shown to depend on the orientation of the external magnetic field *H* in the *a*–*b* plane. For a tetragonal system, a fourfold symmetry is observed and the density of states exhibits minima along the gap node directions. For an orthorhombic system, a twofold symmetry should be observed with a minimum corresponding to the field orientation along the Fermi velocity at a gap node on the Fermi surface. The fourfold pattern changes to a twofold one because of the orthorhombicity in the lattice structure. It should be noted that the angle at which a minimum is observed in the density of states as a function of θ in an orthorhombic superconductor does not coincide with the angle corresponding to a gap node in the case of the tetragonal lattice.

The comparison of the results obtained for $Nd_{1.85}Ce_{0.15}CuO_4$ with the results obtained earlier for a $La_{1.85}Sr_{0.15}CuO_4$ single crystal [11] allows us to judge the symmetry type of the superconducting order parameter in an electron-type superconductor. Unlike the fourfold symmetry observed in $La_{1.85}Sr_{0.15}CuO_4$, the $Nd_{1.85}Ce_{0.15}CuO_4$ crystal exhibits a twofold symmetry of $T_c(H)$ and $H_{c2}(T)$ in the *a*–*b* plane. Another important result is the difference in the gap node directions. The

angle at which $T_c(H)$ and $H_{c2}(T)$ are minimal in $Nd_{1.85}Ce_{0.15}CuO_4$ is 29° with respect to the *a* axis. This value differs from the angle $\theta = 45°$ at which the gap node occurs in $La_{1.85}Sr_{0.15}CuO_4$. This result can be interpreted as a specific feature characterizing the anisotropy of the superconducting energy gap in the electron doped material and related to the *d*-wave order parameter in $Nd_{1.85}Ce_{0.15}CuO_4$. Such an interpretation, in its turn, suggests that the mechanisms of superconductivity in electron and hole doped superconductors are similar, and the difference observed in the experiment is related to the structural features.

This work was supported by the Ministry of Science under the State Contract in the framework of the Federal Special-Purpose Scientific-Engineering Program "Research and Development in Priority Directions of Science and Engineering," section "Basic Research in Physics," subject "Controlled Superconductivity," project no. 40.012.1.1.11.46.

## REFERENCES

1. C. C. Tsuei and J. R. Kirtley, Rev. Mod. Phys. **72**, 969 (2000).
2. Yu. A. Izyumov, Usp. Fiz. Nauk **169** (3), 225 (1999).
3. S. Kashiwaya, T. Ito, K. Oka, *et al.*, Phys. Rev. B **57**, 8680 (1998).
4. F. Hayashi, E. Ueda, M. Sato, *et al.*, J. Phys. Soc. Jpn. **67** (9), 3234 (1998).
5. N. P. Armitage, D. H. Lu, D. L. Feng, *et al.*, Phys. Rev. Lett. **86**, 1126 (2001).
6. V. I. Voronin, A. E. Kar'kin, B. N. Goshchitskiĭ, *et al.*, Fiz. Tverd. Tela (St. Petersburg) **40**, 177 (1998) [Phys. Solid State **40**, 157 (1998)].
7. S. J. L. Billinge and T. Egami, Phys. Rev. B **47**, 14386 (1993).
8. K. Kurahashi, H. Matsushita, M. Fujita, *et al.*, J. Phys. Soc. Jpn. **71**, 910 (2002).
9. I. Tanaka, T. Watanabe, N. Komai, and H. Kojima, Physica C (Amsterdam) **185–189**, 437 (1991).
10. E. Schachinger and J. P. Carbotte, Phys. Rev. B **60**, 12400 (1999).
11. G. Kh. Panova, A. A. Shikov, M. N. Khlopkin, *et al.*, Physica C (Amsterdam) **334**, 25 (2000).

*Translated by E. Golyamina*

JETP Letters, Vol. 75, No. 11, 2002, pp. 583–584. Translated from Pis'ma v Zhurnal Éksperimental'noĭ i Teoreticheskoĭ Fiziki, Vol. 75, No. 11, 2002, pp. 703–704.


# Electronic Conduction in Quasicrystals at Low Temperatures

**Yu. Kh. Vekilov* and É. I. Isaev**

*Moscow Institute of Steel and Alloys, Leninskiĭ pr. 4, Moscow, 119991 Russia*

** e-mail: yuri_vekilov@yahoo.com*

Received March 25, 2002; in final form, April 29, 2002

At low temperatures, a perfect quasicrystal is in the "critical" state of metal–insulator transition. A power-law temperature dependence of conductivity, which was experimentally observed at $T < 5$ K in the icosahedral phase of Al–Pd–Re, was obtained using the critical wave functions. Mott's hopping law was also observed in the Al–Pd–Re samples and explained by the delocalization of electronic states in the momentum space. © *2002 MAIK "Nauka/Interperiodica".*

PACS numbers: 71.23.Ft; 71.30.+h

Quasicrystals have a finite electronic contribution to heat capacity (density of states at the Fermi level is low but finite); a negative temperature coefficient of electrical resistivity, with the resistivity ratio $\mathcal{R} = \rho(4.2\text{ K})/\rho(300\text{ K})$ ranging from several units to two hundred and even higher, depending on the object and the sample quality; and a low residual conductivity, which decreases as the sample becomes more perfect and defects are annealed. As a rule, the resistivity ratio $\mathcal{R}$ is a measure of the sample quality: the higher $\mathcal{R}$, the higher the sample quality and the lower the residual resistivity.

Measurements of conductivity at low temperatures indicate that perfect quasicrystals behave similarly to the usual disordered objects (disordered metals, doped semiconductors, etc.) near the metal–insulator transition. For the samples of icosahedral quasicrystal *i*-Al–Pd–Re with different ratios $\mathcal{R}$, a root temperature dependence of conductivity $\sigma \sim T^{1/2}$ is ordinarily observed at $T < 20$ K. For samples with $\mathcal{R}$ on the order of 20 and higher, this dependence is replaced at $T < 5$ K by the law $\sigma \sim T^{1/3}$ [1, 2]. In some cases, for samples with high $\mathcal{R}$ (~45 and higher), a variable-range hopping (VRH) conduction obeying either Mott's law $\sigma = \sigma_0\exp[-(T_0/T)^{1/4}]$ or the Efros–Shklovskiĭ law $\sigma = \sigma_0\exp[-(T_0'/T)^{1/2}]$ [2] is observed (see review of experimental data in [7]).

It is known from the theory of metal–insulator transition (Anderson transition) that, as the transition to the insulator (metallic) phase is approached, the correlation length $\xi$ (localization length) tends to infinity. According to the scaling considerations for the Anderson transition with interacting electrons [3], at $L < L_T$ and $\xi \ll L_T$ ($L$ is the sample size, $L_T = \sqrt{D\hbar/T}$, and $D$ is the diffusion coefficient) the correction to the conductivity in this region is proportional to $\sqrt{T}$. In the critical region, $\xi \gg L_T > L$, and $\sigma \sim T^{1/3}$.

It is known that the electron wave functions near the metal–insulator transition point are neither extended nor exponentially decreasing but decrease with distance following the power law ("critical" wave functions). The wave functions in a three- dimensional perfect quasicrystal show the same behavior; i.e., $\varphi \sim r^{-\alpha}$ [4, 5]. We demonstrate below that the temperature dependence of conductivity for the critical wave functions in a quasicrystal is close to $\sigma \sim T^{1/3}$.

Let us consider the quasicrystal as a structural limit of a series of periodic approximants with increasing period and use the model of fractional Fermi surface (FFS) [6]. In [7], it was shown that the FFS model is capable of explaining not only the power-law temperature dependence of conductivity but also the VRH conduction in a quasicrystal, provided that the tunneling through the gaps formed by Bragg reflections are taken into account. As expected, Mott's law is obtained for the exponentially decreasing wave functions.

Following [7], we consider the VRH regime and calculate the tunneling integral using the critical wave functions $\varphi \sim r^{-\alpha}$ and, according to Mott's procedure, determine the conductivity

$$\sigma \sim I\exp(-\Delta E/kT), \tag{1}$$

where $\Delta E = 3/4\pi R^3 N(E_F)$ is the lowest activation energy for hopping at distance $R$, and $I$ is the tunneling integral

$$I \sim \left|R^{-\alpha}\right|^2 \equiv \exp(-2\alpha\ln R). \tag{2}$$

The expression

$$\exp(-2\alpha\ln R)\exp(-\Delta E/kT) \tag{3}$$

is maximum when the exponent

$$-2\alpha\ln R - \Delta E/kT \tag{4}$$

is minimum. By substituting $\Delta E$ in Eq. (4) and minimizing Eq. (4) with respect to $R$, we determine the optimal hopping length. It is then straightforward to obtain for the conductivity

$$\sigma \sim T^{2\alpha/3}. \quad (5)$$

The numerical estimates of the exponent $\alpha$ in the tight-binding approximation and the use of level statistics for determining the same exponent from a series of periodic approximants of a model quasicrystal [4, 5] yield values ranging from 0.6 to 0.8. Considering that the model is rather crude and that the processing of the experimental results for conductivity at low temperatures is not too accurate, the coincidence of the obtained dependence $\sigma \sim T^{2\alpha/3}$ with the experiment can be regarded as reasonable. Thus, the result obtained in the microscopic model coincides with the predictions of the scaling localization theory [3] for the critical metal–insulator transition region.

Mott's law $\sigma \sim \exp[-(T_0/T)^{1/4}]$ cannot be obtained with the use of critical wave functions [7]. It is obtained with the well-localized exponentially decreasing wave functions. Nevertheless, Mott's law in quasicrystals is observed experimentally, despite the fact that the wave functions are critical. This paradox can be resolved if one considers the localization of electronic states of a quasicrystal in the momentum (reciprocal) space (much as Al'tshuler and Levitov [8] reduced the problem of weak chaos in the Kepler quantum problem to the problem of electron motion in a periodic lattice of scatterers).

Under condition that $|U_{g-g'}| > |E_g - E_{g'}|$, where $U_{g-g'}$ is the Fourier components of lattice potential and $g$ and $g'$ are the reciprocal lattice vectors (in a quasicrystal, $\{g\}$ forms a dense set), resonances (and also resonances of the resonances themselves) may appear near the spectral gaps appearing due to the interaction of FFS with the face of Brillouin zone, and this may be followed by the delocalization of electronic states in the momentum space [8]. As a result, the exponentially decreasing electronic states should appear and lead to Mott's law in real space [7]. The condition $|U_{g-g'}| > |E_g - E_{g'}|$ for the appearance of resonances in a quasicrystal can easily be met, e.g., for the gaps corresponding to the reciprocal lattice vectors forming the Brillouin quasi-zone (the first strong reflections in the diffraction pattern), so that the observation of Mott's law can serve as the experimental confirmation of the existence of resonances.

We are grateful to S.I. Mukhin and D.V. Livanov for discussions. This work was supported by the Russian Foundation for Basic Research (project no. 00-02-17668), the NWO (grant no. 047-008- 016), the Royal Swedish Academy of Sciences, and the Department of Science and Technologies of the Moscow Government (project no. 1.1.240).

## REFERENCES

1. J. Delahaye and C. Berger, Phys. Rev. B **64**, 094203 (2001).
2. V. Srinivas, M. Rodmar, R. König, *et al.*, Phys. Rev. B **65**, 094206 (2002).
3. B. L. Al'tshuler and A. G. Aronov, Pis'ma Zh. Éksp. Teor. Fiz. **37**, 349 (1983) [JETP Lett. **37**, 410 (1983)].
4. D. V. Olenev, É. I. Isaev, and Yu. Kh. Vekilov, Zh. Éksp. Teor. Fiz. **113**, 1009 (1998) [JETP **86**, 550 (1998)].
5. Yu. Kh. Vekilov, E. I. Isaev, and S. F. Arslanov, Phys. Rev. B **62**, 14040 (2000).
6. S. E. Burkov, A. A. Varlamov, and D. V. Livanov, Phys. Rev. B **53**, 11504 (1996).
7. Yu. Kh. Vekilov, É. I. Isaev, and D. V. Livanov, Zh. Éksp. Teor. Fiz. **121**, 203 (2002) [JETP **94**, 172 (2002)].
8. B. L. Altshuler and L. S. Levitov, Phys. Rep. **288**, 487 (1997).

*Translated by V. Sakun*

JETP Letters, Vol. 75, No. 11, 2002, pp. 585–587. Translated from Pis'ma v Zhurnal Éksperimental'noĭ i Teoreticheskoĭ Fiziki, Vol. 75, No. 11, 2002, pp. 705–708.


# Sign Reversals of the Carriers and the Volume Change in Al–Cu–Fe Quasicrystalline Alloys

**A. F. Prekul, V. A. Kazantsev, N. Yu. Kuz'min, and N. I. Shchegolikhina**

*Institute of Metal Physics, Ural Division, Russian Academy of Sciences, Yekaterinburg, 620219 Russia*

Received May 6, 2002

New results of dilatometric experiments with rapidly quenched Al–Cu–Fe quasicrystalline alloys in the course of their thermal annealing are presented. It is established that the icosahedral (I) phases with different types of carriers exhibit different signs of volume changes with ordering. The observed effect is a direct experimental proof of the fact that structural defects in icosahedral quasicrystals are electrically active centers. © *2002 MAIK "Nauka/Interperiodica".*

PACS numbers: 71.23.Ft; 72.20.Pa

It is well known that the electronic properties of stable icosahedral quasicrystals are highly sensitive to the degree of the structural perfection of their lattice. The origin of this phenomenon is still unknown. In this connection, researchers are searching for empirical laws that relate the kinetic and thermodynamic coefficients in the experiments where the heat treatment is a parameter of the system [1]. From such experiments, it was found that samples of fast-quenched quasicrystalline alloys increase in volume under a high-temperature annealing [2]. A volume change accompanying a structural transformation is a fairly common phenomenon, and the observed effect would hardly attract special attention, were it not for the following fact.

A thermal ordering of I phases is accompanied by a sharp drop in the residual conductivity $\sigma_0$ of the samples. The magnitude of the effect is different in different systems. For example, in the Al–Cu–V system, $\sigma_0$ is about 5000 $\Omega^{-1}$ cm$^{-1}$, in the Al–Cu–Fe system, it is about 100 $\Omega^{-1}$ cm$^{-1}$, and in Al–Pd–Re, about 10 $\Omega^{-1}$ cm$^{-1}$. It was found that the volume change and the value of the residual conductivity correlate with each other. The greater the volume change due to the annealing of the disordered phase, the closer the state of the ordered I phase to the metal–insulator transition. Since in quasicrystals the value of $\sigma_0$ is mainly determined by the concentration of metallic electrons, one can expect that the volume changes are somehow directly related to the concurrent existence of free carriers and structural defects in the system.

In trying to reveal the mechanism relating the electronic and structural (volume) transformations, we noticed that, in stable I phases, a sign reversal of the metallic carriers takes place. Depending on the contents of different components, either *n*-type (a negative Hall effect) or *p*-type (a positive Hall effect) I phases are realized [3, 4]. If we assume that the presence of free carriers in quasicrystals is related to the presence of defects, we arrive at an analogy with semiconductors in which the intrinsic defects are charged centers. When the number of these centers varies, the concentration of free electrons in the conduction band (or the concentration of free holes in the valence band) also varies. In this case, the volume changes are not only possible but also predictable. An excessive positive charge of a defect enhances the Coulomb repulsion of atoms in the defect region and causes a local expansion of the lattice. Conversely, an excessive negative charge of a defect weakens the direct Coulomb repulsion of atoms in the defect region and causes a local compression of the lattice. In the presence of a great number of charged defects and in conditions of a pronounced decompensation, one should expect that the sign reversal of the carriers may be accompanied by a sign reversal of the changes in the macroscopic dimensions of the sample.

We decided to verify whether the aforementioned reversals in quasicrystals accompany each other. For this purpose, we prepared Al–Cu–Fe alloys of the following compositions: $Al_{63}Cu_{25}Fe_{12}$, $Al_{62.8}Cu_{24.8}Fe_{12.4}$, $Al_{62}Cu_{25.5}Fe_{12.5}$, and $Al_{62.3}Cu_{24.9}Fe_{12.8}$. According to data from [3], the first two alloys are *n*-type I phases and the second two alloys are *p*-type I phases. The alloys were prepared in an arc furnace in high-purity argon from components whose purity was no lower than 99.99. The samples were obtained as follows. First, Cu and Fe were alloyed, and then Al was added. To make the alloy homogeneous, the ingot was five times remelted by turning it over with the exposure time up to 60 s. Then, an ingot of the alloy was melted on a flat surface and flattened by a falling copper block. Samples in the form of parallelepipeds with the dimensions $4 \times 4 \times 6$ mm were cut out of the resulting plate by the spark cutting method. The measurements were performed using a SINKU-RIKO quartz dilatometer. The procedure was as follows. The temperature was

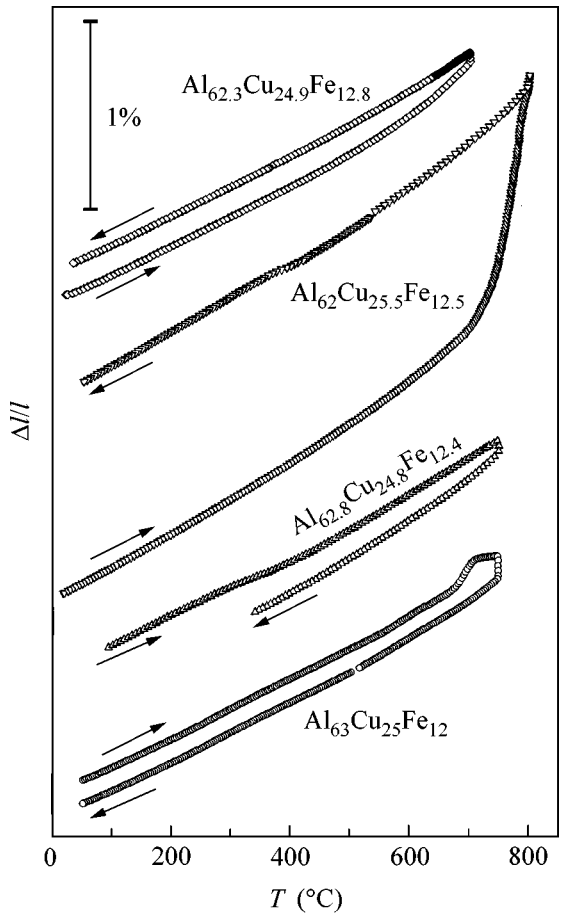


**Fig. 1.** Effect of the heat treatment on the linear dimensions of the samples of four quenched alloys.

increased at a rate of 5°C/min to 700–750°C and maintained constant at this level within 1 h; then, it was reduced to room temperature at a rate of 5°C/min. The dilatometer readings were continuously recorded.

The results of measurements are shown in Fig. 1. One can easily see that the alloys behave in different ways. The magnitude of the effect observed at the ordering temperature is different in different samples, but this is not the point of our concern. We are interested in the sign of the hysteresis observed in the linear dimensions of samples when they return to room temperature. One can see that, in *p*-type I phases, the annealing results in an expansion, whereas in *n*-type I phases, it causes a compression of the initial material. Phenomenologically, it means that the *n*-type imperfect I phases are less closely packed while the *p*-type imperfect I phases are more closely packed, as compared to the perfect phases.

According to the logic of the experiment, the observed effect with the sign reversal of the volume changes is a direct proof of the fact that the structural defects in icosahedral quasicrystals are electrically active centers. From the correlation between the sign of the metallic carriers and the sign of the volume changes with varying number of defects, we make the following inferences. The appearance of a defect in an *n*-type I phase is accompanied by electron transfer from the defect to the conduction band. In this case, the defect acquires a positive charge and causes a local expansion of the lattice. The appearance of a defect in a *p*-type I phase is accompanied by electron transfer from the valence band to the defect. In this case, free holes appear in the valence band, and the defect acquires a negative charge and causes a local compression of the lattice. When the samples are annealed, the number of defects decreases, and the sample volume decreases or increases, accordingly, to its equilibrium value. The concentration of metallic carriers decreases in both cases. If this scenario of metallic state evolution takes place, the Fermi level of an imperfect I phase is either near the bottom of an almost empty conduction band or near the top of an almost filled valence band. Correspondingly, I phases that differ in the number of defects and in the value of $\sigma_0$ form a homologous series of states at the metal–insulator transition with respect to the band filling.

Over the last ten years, numerous theoretical and experimental studies of the electronic structure of stable icosahedral quasicrystals have been carried out. However, the problem still remains poorly understood. Moreover, new problems challenging both theory and experiment have appeared [5]. Primarily, this refers to the role of aperiodicity. Until now, no physical properties that could be directly attributed to the aperiodic structure of I phases had been revealed. This is explained by two factors: the lack of knowledge of the type of electron states (extended, critical, or localized) in a perfect aperiodic structure and the lack of knowledge of the role of defects. In the framework of conventional band concepts, the semimetal version of the electronic structure, which represents the I phase as a two-band metal with a weak band overlapping, has been studied in detail. In this case, the role of defects is reduced to the limitation of the electron free path by the interatomic distance and to the formation of a pseudogap at the Fermi level [6]. The semiconductor version of the electronic structure (the nonoverlapping band approximation) was developed for explaining the giant negative temperature coefficient of resistance and the unusual magnetic and optical properties of quasicrystals [7–9]. In the framework of this approach, the role of defects was not specified. In this paper, the role of defects is determined, as far as we know, for the first time. The role of defects in quasicrystals proved to be opposite to their role in metallic systems. Evidently, the understanding of many features of the physical properties can undergo considerable changes. As an example, we consider the Curie-type component of magnetic susceptibility at low temperatures.

On the whole, the data of magnetic experiments testify that the atoms of high-structural-quality I phases of Al–Cu–Fe have no localized moments, i.e., are in the zero-spin state [10]. Therefore, earlier, we ascribed the Curie-type component to the presence of uncontrolled impurities or foreign phases [11]. Now, we may suppose that the nonzero spin is related to the electron configurations of the alloy's own atoms in the defect. Hence, the Curie constant can serve as the measure of the concentration of these defects and, what is most interesting, the measure of the free carrier concentration. We tested this assumption with the data of the experiment in [11], in which the temperature dependences of conductivity and magnetic susceptibility were studied for different stages of the heat treatment of a fast-quenched $Al_{62}Cu_{25.5}Fe_{12.5}$ alloy. The result of testing is shown in Fig. 2. One can see that the dependence is close to linear. This result is quite unexpected, because a linear dependence should be observed only when all defects are identical. In quasicrystals, a full identity of defects can hardly be possible, because the icosahedral lattice has no equivalent positions [5].

The subsequent confirmation and development of the concept of charged defects of an icosahedral lattice is possible by different experiments, both direct and indirect. For example, a structural experiment can consist in studying the dependence of interplanar spacings on the degree of perfection of the lattice in the *n*- and *p*-type I phases with the aim of detecting the sign reversal of these changes. As far as we know, such studies had never been carried out before. Spectroscopic methods can be used to study the changes that occur in the charge state of part of the atoms with varying degrees of perfection of the lattice. As for the indirect experiments, a good illustration could be the detection of different signs of the effect of hydrostatic pressure on the residual conductivity in *n*- and *p*-type I phases. Finally, different signs of the volume changes due to ordering may give rise to morphological differences between the samples of *n*- and *p*-type I phases. For example, on the surface [12, 13] and in the bulk [14] of some stable I phases, faceted voids are observed, whose origin has not yet been understood. The $Al_{62}Cu_{25.5}Fe_{12.5}$ phase, in which this phenomenon was observed and thoroughly investigated, has (according to the aforementioned data) a positive sign of the Hall effect and increases in volume as a result of ordering. For the other phase, $Al_{71}Pd_{20}Mn_9$, in which this phenomenon was also observed, the sign of the Hall effect is unknown, but it was found that the volume of this phase increases with ordering [13]. If the effect of faceted voids is of charge-related origin, one can expect that this effect will be mainly observed in *p*-type I phases.

We are grateful to M.I. Kurkin for the interest taken in this study and for the idea of taking into account the possible role of Coulomb interaction in the presence of charged defects. We are also grateful to V. Dmitrienko (Institute of Crystallography, Moscow) and J. Hartwig (European Synchrotron Radiation Facility, Grenoble) for useful information and for discussing the formation and morphology of icosahedral phases.

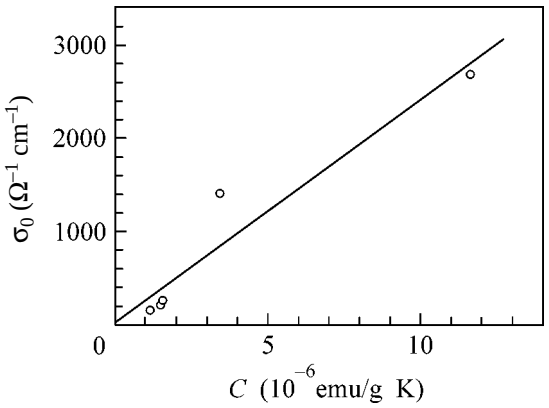


**Fig. 2.** Relation between the Curie constant $C$ and the residual conductivity $\sigma_0$ in the $Al_{62}Cu_{25.5}Fe_{12.5}$ alloy at different stages of its structural relaxation.

## REFERENCES

1. R. Haberkern and G. Fritsch, in *Proceedings of the 5th International Conference on Quasicrystals, Avignon, 1995* (World Scientific, Singapore, 1995), p. 460.
2. A. F. Prekul, V. A. Kazantsev, N. Yu. Kuz'min, *et al.*, Pis'ma Zh. Éksp. Teor. Fiz. **67**, 190 (1998) [JETP Lett. **67**, 203 (1998)].
3. P. Lindqvist, C. Berger, T. Klein, *et al.*, Phys. Rev. B **48**, 630 (1993).
4. R. Haberkern, K. Khedhri, C. Madel, *et al.*, Mater. Sci. Eng. **294–296**, 475 (2000).
5. Z. M. Stadnik, Springer Ser. Solid-State Sci. **257–293**, 126 (1999).
6. U. Mizutani, J. Phys.: Condens. Matter **10**, 4609 (1998).
7. D. N. Basov, F. S. Pierce, P. Volkov, *et al.*, Phys. Rev. Lett. **73**, 1865 (1994).
8. A. F. Prekul, L. V. Nomerovannaya, A. B. Rol'shchikov, *et al.*, Fiz. Met. Metalloved. **82**, 75 (1996).
9. A. F. Prekul, N. Yu. Kuzmin, and N. I. Shchegolikhina, Mater. Sci. Eng. **294–296**, 527 (2000).
10. S. Matsuo, H. Nakano, T. Ishimasa, and Y. Fukano, J. Phys.: Condens. Matter **1**, 6893 (1989).
11. A. F. Prekul, N. Yu. Kuzmin, and N. I. Shchegolikhina, in *Proceedings of the International Conference "Aperiodic Structures-2001," Krakow, 2001*, p. 138.
12. M. Audier, P. Guyot, and Y. Brechet, Philos. Mag. Lett. **61**, 55 (1990).
13. C. Beeli, T. Godecke, and R. Luck, in *Proceedings of the 6th International Conference on Quasicrystals, Tokyo, Japan, 1997*, p. 55.
14. L. Mancini, E. Reinier, P. Cloetens, *et al.*, Philos. Mag. A **78**, 1175 (1998).

*Translated by E. Golyamina*

JETP Letters, Vol. 75, No. 11, 2002, pp. 588–592. From Pis'ma v Zhurnal Éksperimental'noĭ i Teoreticheskoĭ Fiziki, Vol. 75, No. 11, 2002, pp. 709–713.


# Nonsinusoidal Current–Phase Relation in SFS Josephson Junctions[1]

**A. A. Golubov[1], M. Yu. Kupriyanov[2], and Ya. V. Fominov[3, 1]**

[1] *Department of Applied Physics, University of Twente, 7500 AE Enschede, The Netherlands*
*e-mail: a.golubov@tn.utwente.nl*

[2] *Nuclear Physics Institute, Moscow State University, Vorob'evy Gory, Moscow, 119899 Russia*
*e-mail: mkupr@pn.sinp.msu.ru*

[3] *Landau Institute for Theoretical Physics, Russian Academy of Sciences, ul. Kosygina 2, Moscow, 117940 Russia*
*e-mail: fominov@landau.ac.ru*

Received April 25, 2002

Various types of current–phase relation $I(\varphi)$ in superconductor–ferromagnet–superconductor (SFS) point contacts and planar double-barrier junctions are studied within the quasi-classical theory in the limit of thin diffusive ferromagnetic interlayers. The physical mechanisms leading to highly nontrivial $I(\varphi)$ dependence are identified by studying the spectral supercurrent density. These mechanisms are also responsible for the 0–π transition in SFS Josephson junctions. © *2002 MAIK "Nauka/Interperiodica".*

PACS numbers: 74.50.+r; 74.80.-g

The relation between the supercurrent $I$ across a Josephson junction and the difference φ between the phases of the order parameters in the superconducting banks is an important characteristic of structure. The form of $I(\varphi)$ dependence is essentially used for analyzing the dynamics of systems containing Josephson junctions [1]. Studying $I(\varphi)$ also provides information on pairing symmetry in superconductors [2].

In structures with tunnel-type conductivity of a weak link (SIS), the current–phase relation is sinusoidal, $I(\varphi) = I_c \sin\varphi$ with $I_c > 0$, over the whole temperature range below the critical temperature. At the same time, in point contacts (ScS) and junctions with metallic type of conductivity (SNS), strong deviations from the sinusoidal form take place at low temperatures $T$ [3] with the maximum of $I(\varphi)$ being achieved at $\pi/2 < \varphi_{max} < \pi$.

The situation drastically changes if there is a magnetoactive material in the region of the weak link. The transition from the 0 state [$I(\varphi) = I_c \sin\varphi$ with $I_c > 0$] to the π state ($I_c < 0$) in junctions containing ferromagnets was theoretically predicted for a variety of Josephson structures [4–12] and experimentally observed in the SFS and SIFS junctions [13, 14]. In the general case, modifications of $I(\varphi)$ are not reduced to the 0–π transition. It was shown that the tunneling across a ferromagnetic insulator ($F_I$) in clean $SF_IS$ junctions [15] or across a magnetically active interface between two superconductors [16] may result in a nonsinusoidal shape of $I(\varphi)$ due to the shift of Andreev bound states. A similar situation occurs in long SFS junctions with ideally transparent interfaces in the clean [17] and diffusive [7, 8] regimes.

However, in the latter case the effects take place only in a narrow interval of very low temperatures (due to the smallness of the Thouless energy), while here we will consider short-length structures, where the effects are more pronounced and exist practically over the whole temperature range (the role of temperature will be discussed elsewhere [18]).

In this letter, we investigate anomalies of the $I(\varphi)$ relation in several types of SFS structures which allow an analytic solution but have not yet been fully explored: the SFcFS point contact with clean or diffusive constriction as a weak link and the double-barrier SIFIS junction; the ferromagnetic layers are assumed to be thin, and the magnetization is homogeneous throughout the F part of the system. In particular, we show that the maximum of $I(\varphi)$ can shift from $\pi/2 \leq \varphi_{max} < \pi$ to $0 < \varphi_{max} < \pi/2$ as a function of the exchange field in the ferromagnet. Previously, a current–phase relation of this type was theoretically predicted either if superconductivity in the S electrodes was suppressed by the supercurrent in the SNS structure [19–21] or in the vicinity of $T = 0$ in long SFS junctions [7, 8].

The outline of the paper is as follows. We start by studying the SFcFS structure composed of two SF sandwiches linked by a clean Sharvin constriction with an arbitrary transparency $D$. We show that the energy–phase relation of this junction can have two minima: at $\varphi = 0$ and $\varphi = \pi$ (the junction energy in the pure 0 or π state has a *single* minimum at $\varphi = 0$ or $\varphi = \pi$, respectively). As a result, the $I(\varphi)$ dependence can intersect

[1] This article was submitted by the authors in English.

zero not only at $\varphi = 0$ and $\varphi = \pi$ but also at an arbitrary value $\varphi_0$ from the interval $0 < \varphi_0 < \pi$. The salient effects occurring in the junctions with clean constriction survive the averaging over the distribution of transmission eigenvalues and, thus, occur also in the diffusive point contacts. Physically, the properties of SFS structures are explained by the splitting of Andreev levels in the exchange field; to demonstrate this, we study the spectral supercurrent. Finally, we show that the same mechanism provides shifting of the $I(\varphi)$ maximum to $\varphi < \pi/2$ in the double-barrier SIFIS junctions, which can be more easily realized in experiment.

**SFcFS with clean constriction.** We start with a model structure composed of two superconducting SF bilayers connected by a clean constriction with transparency $D$ (the constriction size $a$ is much smaller than the mean free path $l$: $a \ll l$). We assume that the S layers are bulk and that the dirty-limit conditions are fulfilled in the S and F metals. For simplicity, we also assume that the parameters of the SF interfaces $\gamma$ and $\gamma_B$ obey the condition

$$\gamma \ll \max(1, \gamma_B),$$
$$\gamma_B = R_B\mathcal{A}_B/\rho_F\xi_F, \quad \gamma = \rho_S\xi_S/\rho_F\xi_F, \tag{1}$$

where $R_B$ and $\mathcal{A}_B$ are the resistance and the area of the SF interfaces, $\rho_{S(F)}$ is the resistivity of the S (F) material, and the coherence lengths are related to the diffusion constants $D_{S(F)}$ as $\xi_{S(F)} = \sqrt{D_{S(F)}/2\pi T_c}$, where $T_c$ is the critical temperature of the S material. We will consider symmetric structure and restrict ourselves to the limit where the thickness of F layers is small:

$$d_F \ll \min(\xi_F, \sqrt{D_F/2H}), \tag{2}$$

where $H$ is the exchange energy in the F layers.

Under condition (1), we can neglect the suppression of superconductivity in the S electrodes by the supercurrent and the proximity effect and reduce the problem to the solution of the Usadel equations [22] in the F layers

$$\xi_F^2\frac{\partial}{\partial x}\left[G_F^2\frac{\partial}{\partial x}\Phi_F\right] - \frac{\tilde{\omega}}{\pi T_c}G_F\Phi_F = 0, \tag{3}$$

with the boundary conditions at the SF interfaces ($x = \mp d_F$) in the form [23]

$$\pm\gamma_B\frac{\xi_F G_F}{\tilde{\omega}}\frac{\partial}{\partial x}\Phi_F = G_S\left(\frac{\Phi_F}{\tilde{\omega}} - \frac{\Phi_S}{\omega}\right),$$
$$G_S = \omega/\sqrt{\omega^2 + \Delta_0^2}, \quad \Phi_S(\mp d_F) = \Delta_0\exp(\mp i\varphi/2). \tag{4}$$

In the above equations, the $x$ axis is perpendicular to the interfaces and has its origin at the constriction; $\omega = \pi T(2n + 1)$ are the Matsubara frequencies; $\tilde{\omega} = \omega + iH$; and $\Delta_0$ is the absolute value of pair potential in the superconductors. The function $\Phi$ parameterizes the Usadel functions $G$, $F$, and $\bar{F}$:

$$G_F(\omega) = \frac{\tilde{\omega}}{\sqrt{\tilde{\omega}^2 + \Phi_F(\omega)\Phi_F^*(-\omega)}},$$
$$F_F(\omega) = \frac{\Phi_F(\omega)}{\sqrt{\tilde{\omega}^2 + \Phi_F(\omega)\Phi_F^*(-\omega)}}, \quad \bar{F}_F(\omega) = F_F^*(-\omega). \tag{5}$$

Under condition (2), the spatial gradients in the F layers arising due to the proximity effect and current are small. Then, we can expand the solution to Eqs. (3)–(5) up to the second order in small gradients, arriving at [12]

$$\Phi_{F1,F2} = \Phi_0\exp(\mp i\varphi/2), \quad \Phi_0 = \Delta_0\tilde{\omega}/W, \tag{6}$$

where

$$W = \omega + \tilde{\omega}\gamma_{BM}\Omega, \quad \Omega = \sqrt{\omega^2 + \Delta_0^2}/\pi T_c,$$
$$\gamma_{BM} = \gamma_B d_F/\xi_F, \tag{7}$$

and the indices 1 and 2 refer to the left- and right-hand side of the constriction, respectively.

The supercurrent in the constriction geometry is given by the general expression [24]

$$I = \frac{4\pi T}{eR_N}$$
$$\times \mathrm{Im}\sum_{\omega>0}\frac{(\bar{F}_1F_2 - F_1\bar{F}_2)/2}{2 - D[1 - G_1G_2 - (\bar{F}_1F_2 + F_1\bar{F}_2)/2]}, \tag{8}$$

where $R_N$ is the normal-state resistance of the junction. Inserting Eq. (6) in this expression, we obtain

$$I = \frac{2\pi T}{eR_N}\mathrm{Re}\sum_{\omega>0}\frac{\Delta_0^2\sin\varphi}{W^2 + \Delta_0^2[1 - D\sin^2(\varphi/2)]}. \tag{9}$$

Finally, the current–phase relation takes the form

$$I(\varphi) = \frac{2\pi T}{eR_N}\sum_{\omega>0}\frac{A\Delta_0^2\sin\varphi}{A^2 + B^2},$$
$$A = \Delta_0^2[1 - D\sin^2(\varphi/2)] - H^2(\gamma_{BM}\Omega)^2 + \omega^2(1 + \gamma_{BM}\Omega)^2,$$
$$B = 2\omega H\gamma_{BM}\Omega(1 + \gamma_{BM}\Omega). \tag{10}$$

At small $\omega$, the function $A$ [and, thus, $I(\varphi)$] changes its sign at a finite phase difference $\varphi_c = 2\arcsin\sqrt{[1 - (\gamma_{BM}h)^2]/D}$ if the exchange field is in the range $1 - D < (\gamma_{BM}h)^2 < 1$; here, $h$ is the normalized exchange field $h = H/\pi T_c$. The results for $I(\varphi)$ are shown in Figs. 1 and 2 and can be understood by considering the spectral supercurrent density $\mathrm{Im}J(\varepsilon)$. The latter is obtained by analytic continuation in Eq. (9) and is given

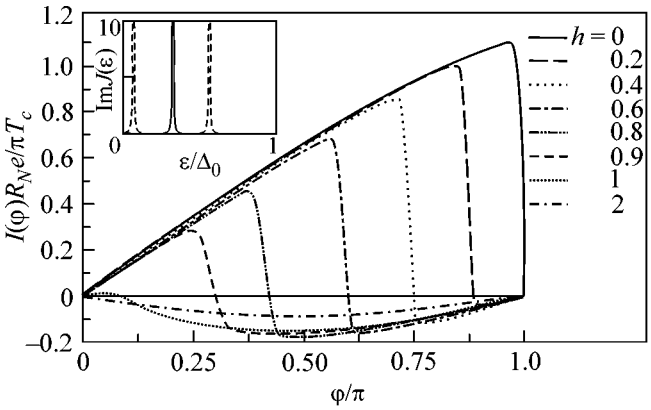


**Fig. 1.** Current–phase relation in a clean SFcFS junction with ideally transparent constriction ($D = 1$) at $T/T_c = 0.01$ and $\gamma_{BM} = 1$ for the different values of normalized exchange field $h$. Inset: spectral supercurrent density at $\varphi = 2\pi/3$ for $h = 0$ (solid line) and $h = 0.4$ (dashed line).

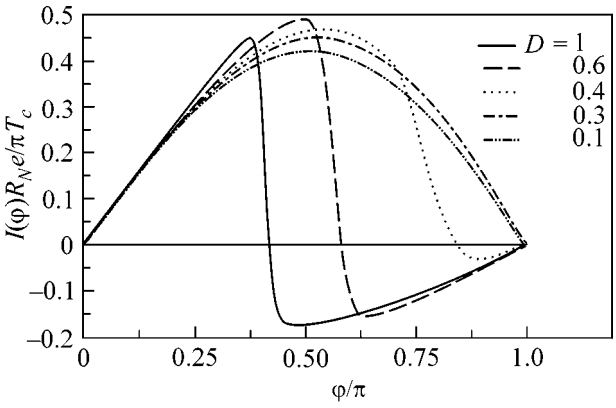


**Fig. 2.** Current–phase relation in a clean SFcFS junction at $T/T_c = 0.01$, $\gamma_{BM} = 1$, and $h = 0.8$ for different values of barrier transparency $D$.

by a sum of delta functions $\delta(\varepsilon - E_B)$, where $E_B$ are the energies of the Andreev bound states. At $\gamma_{BM} = 0$, the well-known result $E_B = \pm\Delta_0\sqrt{1 - D\sin^2(\varphi/2)}$ is reproduced, while at finite $\gamma_{BM}$ the exchange field splits each bound level into two states (see inset in Fig. 1). At $\varphi = \varphi_c$, one of these split (positive) peaks crosses zero leaving the domain $\varepsilon > 0$, and, simultaneously, the negative peak moves from the region $\varepsilon < 0$ into $\varepsilon > 0$, reversing the supercurrent sign.

The sign reversal of the supercurrent (the 0–π transition) can also be achieved at a *fixed H* due to the nonequilibrium population of levels. This phenomenon was studied in long diffusive SNS [25–27] and SFS junctions [7, 8].

**SFcFS with diffusive constriction.** To obtain the $I(\varphi)$ relation for a diffusive point contact [$l \ll a \ll \min(\xi_F, \sqrt{D_F/2H})$], we integrate $\int_0^1 \rho(D)I(D)dD$, where $I(D)$ is given by Eq. (9) for the clean case (note that $R_N \propto D^{-1}$ in this equation) and $\rho(D)$ is Dorokhov density function $\rho(D) = 1/2D\sqrt{1-D}$ [28]. Finally, we arrive at the result

$$I(\varphi) = \frac{4\pi T}{eR_N}\mathrm{Re}\sum_{\omega>0}\frac{\Delta_0\cos(\varphi/2)}{\sqrt{W^2 + \Delta_0^2\cos^2(\varphi/2)}} \times \arctan\left(\frac{\Delta_0\sin(\varphi/2)}{\sqrt{W^2 + \Delta_0^2\cos^2(\varphi/2)}}\right). \quad (11)$$

This expression coincides with the direct solution to the Usadel equations, and at $\gamma_{BM} = 0$ it reproduces the Kulik–Omelyanchuk formula for the diffusive ScS constriction [29].

Calculation of $I(\varphi)$ using the above expression yields results similar to those for the clean point contact, however the transition from the 0 to the π state becomes less sharp (see Fig. 3).

Temperature dependence of the critical current in this case shows a thermally-induced 0–π crossover with a nonzero critical current at the transition point, in agreement with the results of [8, 10] (the results for $I_c(T)$ will be presented elsewhere [18]). This result is natural, since the barrier transparency is high and the current–phase relation is strongly nonsinusoidal. We note that in [13] the measured critical current vanished at the 0–π transition point because of the low-transparency regime (and, hence, sinusoidal current–phase relation) realized in that experiment.

**SIFIS.** Now, we turn to a double-barrier SIFIS junction (I denotes an insulating barrier); this structure is easier for experimental implementation than the SFcFS junction. In the case of SIFIS, due to dephasing effects (this situation is similar to the SINIS junction [30]), the supercurrent cannot be obtained by integrating over the corresponding transmission distribution (except for the case of vanishing $\gamma_{BM}$) and must be calculated by solving the Usadel equations.

We assume that condition (1) is satisfied; then we can neglect the suppression of superconductivity in the S electrodes by the supercurrent and the proximity effect. In this case, the system is described by Eqs. (3)–(5), although now instead of two F layers connected by a constriction we have a continuous F layer (at $-d_F < x < d_F$).

We also assume that the F layer is thin [condition (2)] and that $\gamma_B \gg d_F/\xi_F$; hence, the spatial gradients in the F layer are small. Then (similarly to the case of con-

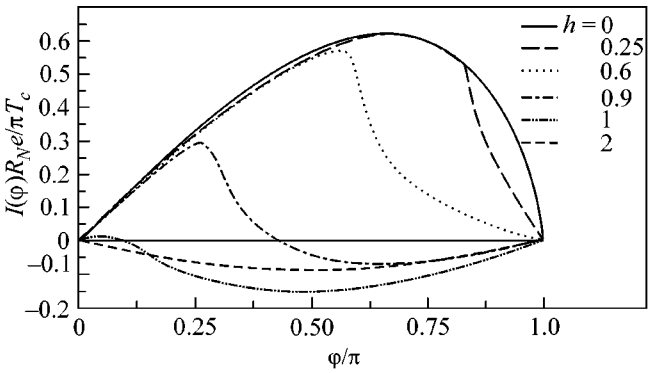


**Fig. 3.** Current–phase relation in diffusive SFcFS point contact at $T/T_c = 0.01$ and $\gamma_{BM} = 1$ for different values of exchange field $h$.

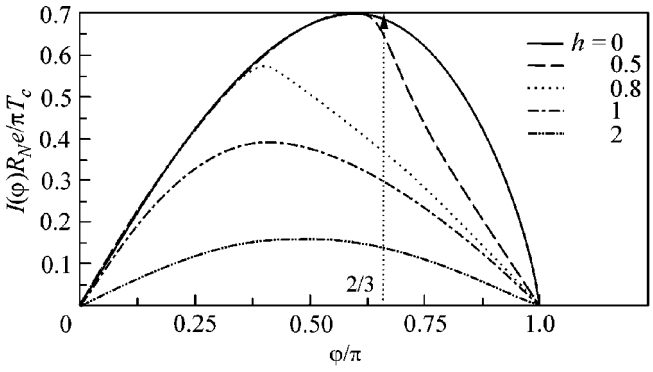


**Fig. 4.** Current–phase relation in a double-barrier SIFIS junction at $T/T_c = 0.02$ and $\gamma_{BM} = 1$ for different values of exchange field $h$. The value $\varphi = 2\pi/3$ is used in Fig. 5.

striction) we can expand the solution to Eqs. (3)–(5) up to the second order in small gradients, arriving at

$$\Phi_F = \Phi_0 \cos(\varphi/2) + i\frac{\tilde{\omega} G_S \Delta_0 \sin(\varphi/2)}{\omega G_F}\frac{\chi}{\gamma_B}\frac{\chi}{\xi_F}, \qquad (12)$$

$$G_F = \frac{\tilde{\omega}}{\sqrt{\tilde{\omega}^2 + \Phi_0^2 \cos^2(\varphi/2)}}, \qquad (13)$$

with $\Phi_0$ defined in Eq. (6) [in the final result (12), we retained only the first order in gradients; this accuracy is sufficient for calculating the current].

Inserting solution (12), (13) into the general expression for the supercurrent

$$I = -\frac{\pi T \mathcal{A}_B}{e\rho_F} \times \mathrm{Im}\sum_{\omega}\frac{G_F^2(\omega)}{\tilde{\omega}^2}\Phi_F(\omega)\frac{\partial}{\partial x}\Phi_F^*(-\omega), \qquad (14)$$

we obtain

$$I(\varphi) = \frac{2\pi T}{eR_N} \times \mathrm{Re}\sum_{\omega>0}\frac{\Delta_0^2 \sin\varphi}{\sqrt{\omega^2 + \Delta_0^2}\sqrt{W^2 + \Delta_0^2\cos^2(\varphi/2)}} \qquad (15)$$

(our assumptions imply that $R_N \approx 2R_B$). This result demonstrates that the SIFIS junction with a thin F layer is always in the 0 state.[2] Nevertheless, $I(\varphi)$ is strongly modified by a finite $H$ (see Fig. 4), especially at low temperatures. Figure 4 clearly demonstrates that an increase in $H$ results not only in the suppression of critical current but also in the shift of the $I(\varphi)$ maximum from $\varphi_{\max} \approx 1.86$ at $H = 0$ to values smaller than $\pi/2$. In the limit of large exchange fields, $h \gg \gamma_{BM}^{-1}$, $I(\varphi)$ returns to the sinusoidal form.

The physical origin of these results can be clarified in the real-energy $\varepsilon$ representation. Making analytic continuation in Eq. (15) by the replacement $\omega \longrightarrow -i(\varepsilon + i0)$, we obtain the spectral supercurrent density $\mathrm{Im}J(\varepsilon)$, which contains contributions of Andreev bound states with different energies:

$$I = \frac{1}{4eR_N}\sum_{\sigma=\pm1}\int \mathrm{Im}J(\varepsilon, \sigma H)\tanh\left(\frac{\varepsilon}{2T}\right)d\varepsilon, \qquad (16)$$

$$\mathrm{Im}J(\varepsilon, H) = \mathrm{Im}\frac{\Delta_0^2 \sin\varphi}{\sqrt{\Delta_0^2 - \varepsilon^2}\sqrt{\Delta_0^2\cos^2(\varphi/2) - \tilde{\varepsilon}^2}}, \qquad (17)$$

$$\tilde{\varepsilon} = \varepsilon + \gamma_{BM}(\varepsilon - H)\Omega(\varepsilon), \quad \Omega(\varepsilon) = \sqrt{\Delta_0^2 - \varepsilon^2}/\pi T_c.$$

Equation (17) implies that, at $\varphi_c = 2\arccos(\gamma_{BM}h)$, the singularities in $\mathrm{Im}J(\varepsilon)$ are shifted to the Fermi level. At $\varphi > \varphi_c$, the negative singularity in $\mathrm{Im}J(\varepsilon)$ crosses the Fermi level for one spin projection and appears in the positive energy domain, whereas the positive peak for the other projection leaves the domain $\varepsilon > 0$ (this process is illustrated in Fig. 5). As a result, the contribution to the supercurrent from low energies changes its sign, and the supercurrent $I(\varphi)$ becomes suppressed at $\varphi > \varphi_c$ (see Fig. 4). However, at higher energies, $\varepsilon \sim \Delta_0$, the modifications in $\mathrm{Im}J(\varepsilon)$ are weak, and the resulting $I(\varphi)$ does not change its sign.

In conclusion, we have studied the nonsinusoidal current–phase relation for the Josephson junctions with thin ferromagnetic interlayers and identified the physical mechanisms of these effects in terms of Andreev bound state splitting in the junction by the exchange

[2] In the case under discussion, where the F layers are thin and the interface parameters obey condition (1), the phase of the pair potential is constant in the S part and almost constant in the F part; however, it jumps at the two SF interfaces [12]. The two jumps compensate each other in SIFIS with a single F layer, whereas in SFcFS they add up at the weak link, thus opening the possibility for the $\pi$ state.

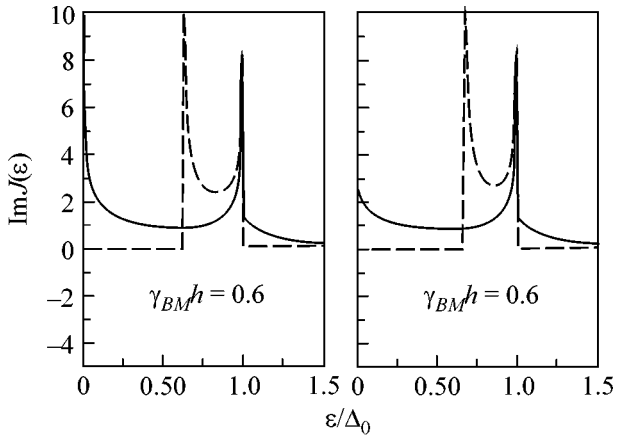


**Fig. 5.** Spectral supercurrent in a diffusive double-barrier SIFIS junction with thin ferromagnetic interlayer at $\gamma_{BM} = 1$ and $\varphi = 2\pi/3$ for the two values of exchange field $h$. The chosen value of $\varphi$ corresponds to $\varphi_c$ at $\gamma_{BM}h = 0.5$, and the figure demonstrates that the positive peak for one spin projection disappears while the negative peak for the other projection appears in the domain $\varepsilon > 0$.

field. In particular, we have shown that zero-energy crossing of Andreev bound states is responsible for the sign reversal of $I(\varphi)$, which also survives the averaging over the distribution of transmission eigenvalues in the diffusive junction. As a result, the energy–phase relation for the junction has two minima: at $\varphi = 0$ and $\varphi = \pi$. The phenomena studied in this work may be used for the engineering of cryoelectronic devices manipulating spin-polarized electrons and in the qubit circuits.

We are grateful to J. Aarts, N.M. Chtchelkatchev, K.B. Efetov, M.V. Feigel'man, V.V. Ryazanov, and M. Siegel for stimulating discussions. M.Yu.K. was supported by the Russian Ministry of Industry, Science, and Technology (RMIST). This work was supported in part (Ya.V.F.) by the Russian Foundation for Basic Research (project no. 01-02-17759), Forschungszentrum Jülich (Landau Scholarship), the Swiss National Foundation, RMIST, and the program "Quantum Macrophysics" of the Russian Academy of Sciences.

## REFERENCES

1. K. K. Likharev, *Dynamics of Josephson Junctions and Circuits* (Gordon and Breach, Amsterdam, 1991).
2. E. Il'ichev, M. Grajcar, R. Hlubina, *et al.*, Phys. Rev. Lett. **86**, 5369 (2001).
3. K. K. Likharev, Rev. Mod. Phys. **51**, 101 (1979).
4. L. N. Bulaevskii, V. V. Kuzii, and A. A. Sobyanin, Pis'ma Zh. Éksp. Teor. Fiz. **25**, 314 (1977) [JETP Lett. **25**, 290 (1977)].
5. A. I. Buzdin, L. N. Bulaevskii, and S. V. Panyukov, Pis'ma Zh. Éksp. Teor. Fiz. **35**, 147 (1982) [JETP Lett. **35**, 178 (1982)].
6. A. I. Buzdin and M. Yu. Kupriyanov, Pis'ma Zh. Éksp. Teor. Fiz. **53**, 308 (1991) [JETP Lett. **53**, 321 (1991)].
7. S.-K. Yip, Phys. Rev. B **62**, R6127 (2000).
8. T. T. Heikkilä, F. K. Wilhelm, and G. Schön, Europhys. Lett. **51**, 434 (2000).
9. E. A. Koshina and V. N. Krivoruchko, Phys. Rev. B **63**, 224515 (2001).
10. N. M. Chtchelkatchev, W. Belzig, Yu. V. Nazarov, and C. Bruder, Pis'ma Zh. Éksp. Teor. Fiz. **74**, 357 (2001) [JETP Lett. **74**, 323 (2001)].
11. Yu. S. Barash and I. V. Bobkova, Phys. Rev. B **65**, 144502 (2002).
12. A. A. Golubov, M. Yu. Kupriyanov, and Ya. V. Fominov, Pis'ma Zh. Éksp. Teor. Fiz. **75**, 223 (2002) [JETP Lett. **75**, 190 (2002)].
13. V. V. Ryazanov, V. A. Oboznov, A. Yu. Rusanov, *et al.*, Phys. Rev. Lett. **86**, 2427 (2001).
14. T. Kontos, M. Aprili, J. Lesueur, *et al.*, cond-mat/0201104.
15. Y. Tanaka and S. Kashiwaya, Physica C (Amsterdam) **274**, 357 (1997).
16. M. Fogelström, Phys. Rev. B **62**, 11812 (2000).
17. L. Dobrosavljević-Grujić, R. Zikić, and Z. Radović, Physica C (Amsterdam) **331**, 254 (2000).
18. A. A. Golubov, M. Yu. Kupriyanov, and Ya. V. Fominov, in preparation.
19. Z. G. Ivanov, M. Yu. Kupriyanov, K. K. Likharev, *et al.*, Fiz. Nizk. Temp. **7**, 560 (1981) [Sov. J. Low Temp. Phys. **7**, 274 (1981)].
20. A. A. Zubkov and M. Yu. Kupriyanov, Fiz. Nizk. Temp. **9**, 548 (1983) [Sov. J. Low Temp. Phys. **9**, 279 (1983)].
21. M. Yu. Kupriyanov, Pis'ma Zh. Éksp. Teor. Fiz. **56**, 414 (1992) [JETP Lett. **56**, 399 (1992)].
22. K. D. Usadel, Phys. Rev. Lett. **25**, 507 (1970).
23. M. Yu. Kupriyanov and V. F. Lukichev, Zh. Éksp. Teor. Fiz. **94**, 139 (1988) [Sov. Phys. JETP **67**, 1163 (1988)].
24. A. V. Zaitsev, Zh. Éksp. Teor. Fiz. **86**, 1742 (1984) [Sov. Phys. JETP **59**, 1015 (1984)].
25. A. F. Volkov, Phys. Rev. Lett. **74**, 4730 (1995).
26. F. K. Wilhelm, G. Schön, and A. D. Zaikin, Phys. Rev. Lett. **81**, 1682 (1998).
27. J. J. A. Baselmans, A. F. Morpurgo, B. J. van Wees, and T. M. Klapwijk, Nature **397**, 43 (1999).
28. O. N. Dorokhov, Solid State Commun. **51**, 381 (1984).
29. I. O. Kulik and A. N. Omelyanchuk, Pis'ma Zh. Éksp. Teor. Fiz. **21**, 216 (1975) [JETP Lett. **21**, 96 (1975)].
30. A. Brinkman and A. A. Golubov, Phys. Rev. B **61**, 11297 (2000).

JETP Letters, Vol. 75, No. 11, 2002, pp. 593–603. Translated from Pis'ma v Zhurnal Éksperimental'noĭ i Teoreticheskoĭ Fiziki, Vol. 75, No. 11, 2002, pp. 714–725.


# Mesoscopic Properties of Quasi-One-Dimensional Conductors with a Charge Density Wave

**Yu. I. Latyshev* and A. A. Sinchenko****

**Institute of Radio Engineering and Electronics, Russian Academy of Sciences, Moscow, 101999 Russia*

***Moscow Engineering Physics Institute, Kashirskoe sh. 31, Moscow, 115409 Russia*

Received April 29, 2002

Recent experiments on a search for small-scale quantum coherence in quasi-one-dimensional materials with a charge-density wave are reviewed. © *2002 MAIK "Nauka/Interperiodica".*

PACS numbers: 72.15.Nj; 71.45.Lr; 73.21.-b; 73.23.-b

## 1. INTRODUCTION

Quasi-one-dimensional conductors with a charge-density wave (CDW) (of which, $NbSe_3$, $TaS_3$, and $K_{0.3}MoO_3$ are the best studied) have been the subject of theoretical and experimental investigations over more than two decades. The condensed electronic state with a CDW was predicted by Peierls in [1]. It manifests itself as a bound electronic state at the Fermi surface (condensate) with a spatially modulated electron density and a gap in the excitation spectrum. One of the most intriguing properties of these materials is that CDW can make a collective contribution to the conductivity (so-called "Fröhlich" conductivity). This property was originally studied in the spirit of Fröhlich's idea [2] about nondissipative CDW motion. This approach was developed most consistently in Bardeen's theory of CDW quantum transport [3]. The models allowing the flux quantization in a mesoscopic CDW ring [4], the Andreev reflection at the normal metal–CDW interface [5], and analogs of the Josephson effect in heterostructures with CDW [6] were also considered theoretically. All these theoretically predicted manifestations of quantum-coherent properties of conductors with CDW have not been confirmed experimentally in macroscopic samples with sizes far exceeding the coherence length of the CDW order parameter. By contrast, virtually all the transport properties of macroscopic samples were satisfactorily described by the classical models of CDW transport [7]. The development of modern technologies has culminated in the possibility of fabricating submicron- and nanometer-scale mesostructures with CDW. This opened the way for studying the coherent properties of CDW on a length scale comparable to and smaller than the phase and amplitude correlation lengths of the CDW order parameter [8]. In this review, the methods of fabrication of the mesostructures with CDW using heavy-ion irradiation, electron-beam lithography, and focused ion beams, as well as the use of microcontacts for obtaining various heterostructures with CDW, will be briefly discussed. We will also discuss experiments on the observation and study of the Aharonov–Bohm effect for a CDW moving in columnar defects in $NbSe_3$, a study of an analog of the Andreev reflection at the normal metal–CDW interface, and the observation of depairing currents in the microchannels formed by the CDW–CDW point contacts in the chain direction. Experimental studies of CDW current conversion on the submicron length scale will also be briefly discussed, together with experiments on the observation of the coherent interlayer tunneling of carriers localized in "pockets" without a Peierls gap at the Fermi surface of a quasi-one-dimensional conductor with an incompletely demetallized electronic spectrum.

## 2. QUANTUM INTERFERENCE OF A CDW MOVING IN COLUMNAR DEFECTS WITH TRAPPED MAGNETIC FLUX

In the classical description, the CDW motion is considered as the motion of a classical object, either rigid [9] or deformable [10], in a periodic potential. In the quantum description, CDW is considered as a quantum object whose motion is a result of coherent tunneling [3]. The majority of observed properties of CDW, including its narrow-band generation, are rather well described by the appropriate classical models [9, 10]. The possible quantum tunneling of CDW was discussed only for very low temperatures [11, 12].

At the same time, it was predicted theoretically that quantum interference effects can be observed for a CDW in a ring formed by a quasi-one-dimensional conductor with a small diameter (comparable to the CDW coherence length) and containing a magnetic flux [4]. For the regime of CDW motion along a ring consisting of a single conducting chain, the magnetoresistance oscillations with a period corresponding to a flux change of a single "superconducting" quantum $\Phi_0 = hc/2e$ were predicted. The cited work motivated experimental search for quantum interference effects in

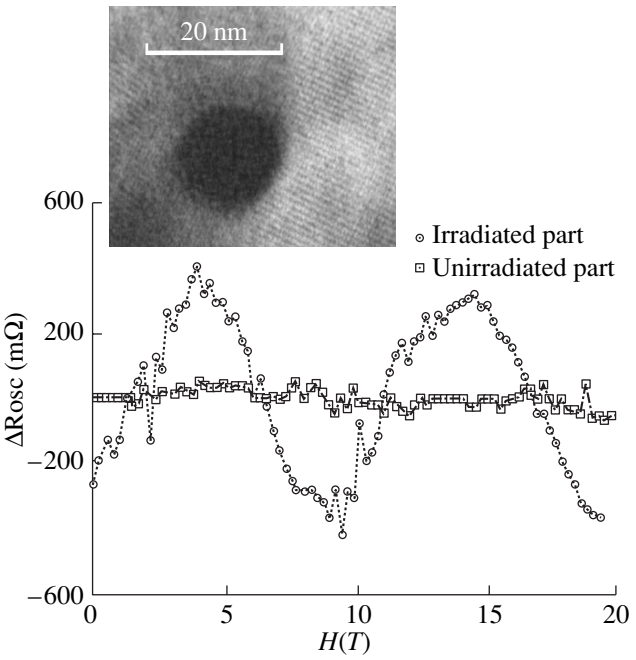


**Fig. 1.** Oscillating magnetoresistance component (quadratic background is subtracted) in the CDW slip regime vs. the magnetic field $H \parallel a^* \parallel$ CD axis in the $NbSe_3$ sample (B1-1) with CD concentration $C = 4 \times 10^9$ defect/cm$^2$ for $I = 100$ μA, $I_t = 100$ μA, and $T = 52$ K. Inset: HREM image of CD.

materials with CDW [13, 14]. The results of this search are presented below.

The experimental idea consisted in the selection of a thin, less than 1-μm-thick, CDW crystal ($NbSe_3$) containing columnar defects (CDs) formed by the irradiation of a material by heavy ions with an energy on the order of 1 GeV. As is well known [15], CD is a homogeneous amorphous cylinder with a diameter of ~10 nm and length of ~10 μm formed in the crystal matrix along the particle track as a result of melting and fast quenching of the material. Since each CD is formed by a single particle, all of them have the same size. It was assumed that, since the defect size is comparable to the CDW amplitude coherence length across the chains, the CDW, when moving through the defect, can "flow around" it to retain coherence in motion. In a magnetic field aligned with the defect axis, the CD behaves as a solenoid making an Aharonov–Bohm contribution [16] to the wave-function phase of the CDW passed through the defect. In the limiting case of the CDW coherent motion over the entire crystal, the contributions from all the defects may be synchronized, thereby increasing appreciably the probability of the effect being observed.

Analysis of the period of CDW conduction magnetooscillations

| No. | $C$ (defect/cm$^2$) | $T$ (K) | $D$ (nm) | $\Delta H$ $(\pi D^2/4)/\Phi_0$ |
|---|---|---|---|---|
| B1-1 | $4 \times 10^9$ | 52 | 15 | 0.86 |
| G1-1 | $5 \times 10^9$ | 50 | 16 | 0.85 |
| | | 36 | 16 | 0.84 |
| G1-3 | $10 \times 10^9$ | 36 | 16 | 0.89 |
| G2-2 | $3 \times 10^9$ | 40 | 16 | 0.97 |

Note: $C$ is the defect concentration; $T$ is the temperature of measurements; $D$ is the diameter of columnar defect; and $\Delta H$ is the oscillation period. The error of determining the quantity $\Delta H$ $(\pi D^2/4)/\Phi_0$ is 15%.

The perfect samples of the $NbSe_3$ single crystals selected were irradiated on two big accelerators, VIKSI (Berlin) and GANIL (Caen, France). For the reference measurements, a part of the sample was usually protected from irradiation. Several irradiation runs were performed using Xe, Pb, and U ions with energies of 0.3–6.0 GeV. The density of defects was varied from $2 \times 10^9$ to $2 \times 10^{10}$ defect/cm$^2$. The direction of the heavy-ion beam coincided with the $a^*$ axis of the irradiated crystal. Beam divergence was less than 0.5°. The diameter of defects was determined using the TEM and HREM techniques and was found to be ≈16 nm (see inset in Fig. 1).

The studies of the differential current–voltage characteristics of the irradiated samples and the spectra of Shapiro steps [17] at a frequency of ~10 MHz showed that, for CD concentrations less than $10^{10}$ defect/cm$^2$, the CDW transport characteristics vary insignificantly and that the coherence in the CDW motion persists over the entire length of the sample (~0.5 mm) [14]. These samples were selected for the magnetoresistance measurements. Magnetoresistance was measured on a Bitter magnet in fields of up to 23 T at the Laboratory of Strong Magnetic Fields (Grenoble). As a rule, the sample had six probes, which were aimed at simultaneously measuring the magnetoresistance of the section containing CDs and the defect-free section. At a given temperature and current through the sample, magnetic field was slowly scanned to the maximum value and back. The measurement results were accumulated and averaged over both scans.

In the CDW slip regime, we observed a magnetoresistance component oscillating with a period of 10 T in the section containing CDs, whereas, under the same conditions, there were no oscillations in the defect-free section [13] (Fig. 1). In the CDW pinning state, the magnetooscillations were not observed in either section. More recently, we carried out a detailed analysis of conditions for the existence of the oscillations and compared their period with the flux captured by the defect [14]. The following facts were established.

(i) Oscillations were reproduced in four samples. Their period corresponded, with an experimental accuracy of ≈15%, to a flux change of a single quantum $hc/2e$ in the defect and was independent of the temperature (36–52 K) and defect concentration ($3 \times 10^9$–$10^{10}$ defect/cm$^2$), see table:

(ii) The oscillation amplitude was maximal at currents stronger than $I_t$ by a factor of 2–3, where $I_t$ is the threshold current corresponding to the CDW depinning, and it decreased both with increasing current and upon approaching the threshold.

(iii) The oscillations were observed in a field aligned with the defect axis and disappeared for the orientations perpendicular to the defect axis [14].

(iv) The oscillations were observed in the perfect and thin samples containing CDs and disappeared in the samples thicker than 1 μm. The oscillations also disappeared upon CD degradation after keeping the sample at room temperature for several months [14].

These results indicate that the magnetoresistance oscillations have a quantum nature. They are observed only for the coherently moving CDW and under the condition that all defects are identical (as-irradiated samples). It was shown in [14] that the coherence of a moving CDW is lost upon increasing current by two to three times and also in the samples with thickness exceeding the phase coherence length (~1 μm) along the $a^*$ axis. The oscillations are observed at high temperatures (on the order of 50 K), at which the one-particle interference effects [18] are negligibly weak. Hence, we can conclude that the oscillations are due to the quantum interference of a CDW coherently moving in the columnar defects with captured flux.

Although the microscopic nature of the phenomenon is not quite clear, it follows from the experiment that the elementary charge determining the microscopic origin of the phenomenon is equal to $2e$, i.e., to the value typical of the quantum interference phenomena in superconductors. However, the validity of this analogy is as yet not clear. The question of the existence and possibility of observing persistent currents in nanostructures with CDW and Josephson-type effects in the heterostructures with CDW is still open [6].

The observed quantum interference of moving CDW raises new questions in the understanding of the mesoscopic properties of a condensed state with CDW and calls for further experimental study and the development of new microscopic theory that would account for the quantum properties of CDW. Recently, two theoretical models were suggested [19, 20] that explain, albeit from different viewpoints, some aspects of the phenomenon observed. In our opinion, both works are based on the model description and cannot account for the phenomenon in full detail. Recently, there has been some progress in the development of the quantum theory of CDW transport [21].

From the experimental point of view, the structures with columnar defects are rather complex and difficult to reproduce. For this reason, the study of the quantum interference of the CDW in a single nanohole is of great interest. At present, work is under way on the preparation of structures with a single nanohole using microetching in focused ion beams [focused ion-beam (FIB) technique; for detail, see below]. The resolution of this method makes it possible to obtain holes with a diameter less than 100 nm. The FIB technique can also be used to decorate columnar defects of a rather low concentration, because the amorphous substance inside the CD should be etched with a higher rate, after which the ion beam can be used to cut out a bridge containing a single CD.

## 3. CARRIER REFLECTION AT THE NORMAL METAL(N)–CDW INTERFACE. CDW GAP SPECTROSCOPY

It is well known that, at the normal metal–superconductor interface, an Andreev reflection (AR) can occur [22], in which a particle incident from the normal metal changes its charge and all momentum components upon reflection. In this case, a charge $2e$ is carried away as a Cooper pair upon transition through the interface, whereas the reflected particle moves back along the incident trajectory. Such a quantum transformation of charge is possible only if the energy of the incident particle is lower than the superconducting gap, where the quasiparticles have no permitted states. This fact was used to demonstrate the AR in the following way (van Kempen method) [23]: a thin normal-metal film with thickness $d$ smaller than the mean free path $l$ was deposited on the superconductor surface. Then, electrons were injected into the normal film from a point contact with diameter $a \ll l$ and reached ballistically the N–S interface. In the presence of AR, most of them would return as holes along the incident trajectories to the point contact (Fig. 2a), thereby reducing the contact resistance by a factor of approximately 2. Therefore, the differential resistance $R_d$ of the contact as a function of bias $V$ on it would have the form of a step function:

$$R_d(V) \approx \begin{cases} A & \text{at } |V| < \Delta \\ 2A & \text{at } |V| > \Delta, \end{cases} \quad (1)$$

where $2A$ is the contact resistance in the absence of AR. As was shown in [24], the presence of an N–S barrier at the interface reduces the AR probability at small biases, giving rise to a local maximum of $R_d(V)$ at $V = 0$. The $R_d(V)$ dependence of this type was observed in [23] (Fig. 2b).

The question of the possibility of observing the subgap carrier reflection at the N–CDW interface was first raised by Kasatkin and Pashitskiĭ in [5], where it was stated that the reflected particle must not change the sign of its charge but must, as in the AR, reverse all its velocity components. Compared to the $R_d(V)$ dependence for the N–S interface, the expected $R_d(V)$ dependence (Fig. 2c) should be mirror-symmetric about the $V$ axis (Fig. 2b), and $R_d(|V| < \Delta)$ should be $\gg R_d(|V| > \Delta)$, because most of the particles reflected along the incident trajectory should return to the contact without changing the charge sign. We undertook a search for this effect in the Au–$K_{0.3}MoO_3$ structures using point

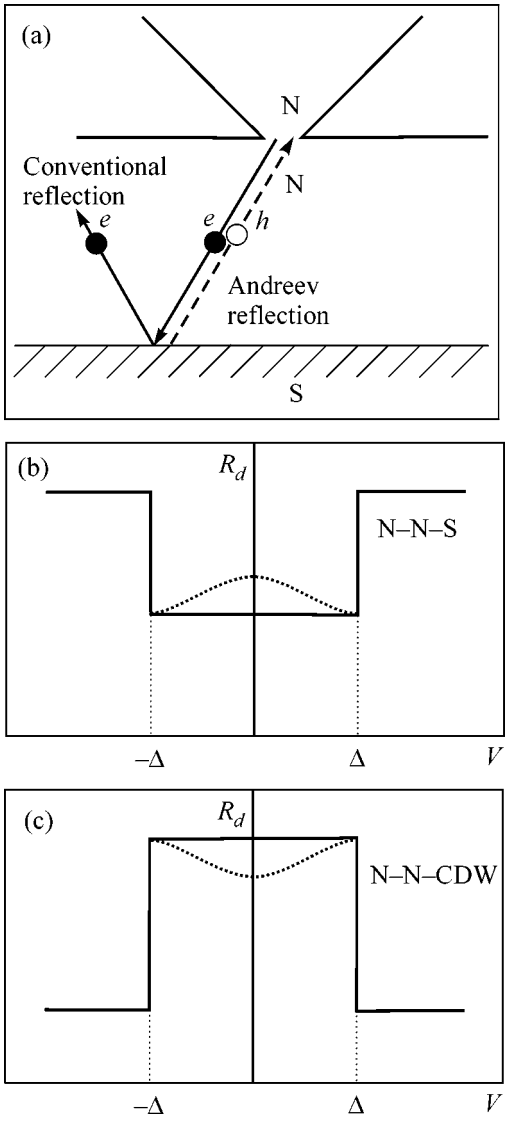


**Fig. 2.** (a) Schemes of normal and Andreev quasiparticle reflections upon the local injection of carriers into a thin normal-metal (N) film applied to a superconductor. (b) Schematic representation of the differential resistance $R_d$ as a function of bias $V$ for the N–N–S structure in the presence of an Andreev reflection at the N–S interface. (c) The $R_d(V)$ dependence expected for the N–N–CDW structure on the basis of the results obtained by Kasatkin and Pashitskiĭ in [5] for the Andreev-type reflection at the N–CDW interface.

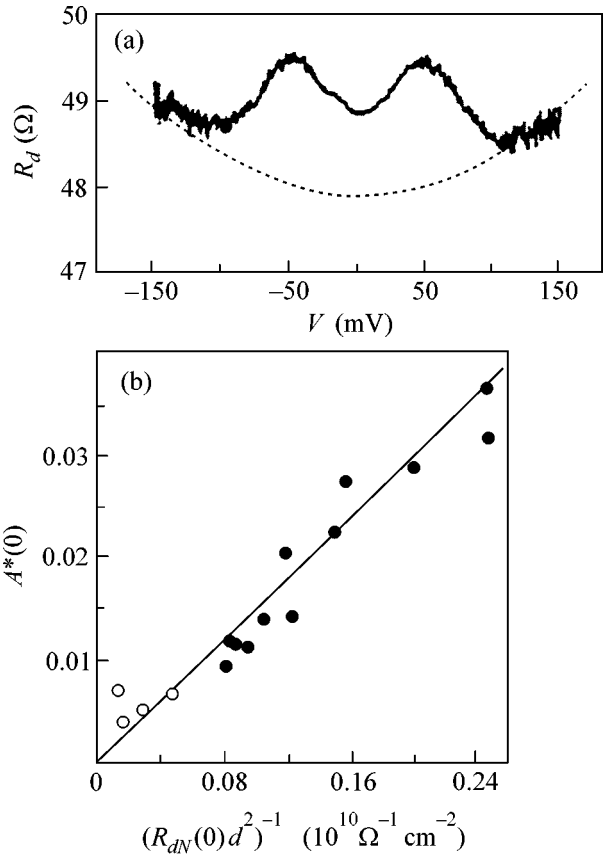


**Fig. 3.** (a) Reflection spectrum of the carriers locally injected at $T$ = 77 K and reflected from the N(Au)–CDW($K_{0.3}MoO_3$) interface. (b) Amplitude contribution from the particles reflected at $V$ = 0 vs. the parameter $(R_{dN}(0)d^2)^{-1} \propto a^2/d^2$, where $a$ is the contact diameter and $d$ is the thickness of the normal-metal film: $d$ = (●) 50 and (○) 100 nm and $T$ = 77 K.

counterelectrodes made from Au or Cu [25]. In the early experiments, a gold film with thickness 50–100 nm was laser deposited onto the end face perpendicular to the axis of conducting chains. Qualitatively, the obtained results were indeed very similar to the expected dependences [25, 26] (Fig. 3a). A sharp drop in $R_d(V)$ at $T$ = 77 K corresponded to the value $2\Delta \approx 100$ mV, which was consistent with the earlier measurements of the Peierls gap in $K_{0.3}MoO_3$ by other methods [27]. The occurrence of a local minimum at zero bias is noteworthy. This minimum indicates that the reflected particle is emitted from the condensate (as in the case of an Andreev reflection) and transmits through the surface barrier, whose transmittivity is small at small energies. At the same time, the contribution from the reflected particles was two orders of magnitude smaller than expected and was only 3%. It was shown in the more detailed studies [26] that the amplitude $A^*$ due to the reflected particles ($A^* = R_d/R_{dN} - 1$) is proportional to $(a/d)^2$ (Fig. 3b), where $a$ is the diameter of a point contact (determined from the contact resistance by the Sharvin formula [28]) and $d$ is the thickness of the gold film. It was concluded from these measurements that the Andreev-type contribution to the reflection comes only from the particles injected along the chains. This is in compliance with the statement [29] that the momentum of the incident particle is transferred to the CDW condensate that moves away from the interface. Contrary to a superconductor, where the Cooper pairs can move in any direction and, hence, the incident par-

ticles can undergo Andreev reflection at any angle, the CDW can move only in the chain direction, so that only those particles which are injected along the chains, whose contribution is small ($\sim 2\pi a^2/d^2$), can contribute to the Andreev-type reflection. The distinction from the AR is also that only the momentum transfer occurs through the N–CDW interface (and not the charge, as in the Andreev reflection). The wavevector of the incident particle is $k_F$, and the momentum of the reflected particle is $-(k_F - \delta k)$. The momentum transfer to the CDW is equal to $\hbar(2k_F + \delta k)$.

A detailed analysis of the alternative explanations and the measurement of the spectra of across-chain reflection [26] showed that the observed spectra of particles reflected from the Au–$K_{0.3}MoO_3$ interface can be explained neither by the mirror reflection from a barrier with height $\Delta$ nor by the Bragg reflection [30] with the participation of the transverse CDW wavevector component. So, the mechanism considered above is as yet the only possible explanation. It should be noted that this mechanism allows the direct subgap quasiparticle-current conversion into CDW current without the formation of a phase-slip center (PSC) [31] (see below for detail).

The $R_d(V)$ dependences similar to those found in the Au–$K_{0.3}MoO_3$ system were recently also observed in the Au–$NbSe_3$ system [32]. The corresponding measurements gave the energy gaps for the high-temperature ($2\Delta_1 \approx 200$ mV) and low-temperature ($2\Delta_2 \approx 60$ mV) CDW in $NbSe_3$ and their temperature dependences. These values agree well with the STM data [33]. Thus, the method of local injection into the N–CDW structures can be used for the spectroscopic determination of the Peierls gap in materials with a CDW. Note that the experiments in [32] were carried out using a direct Au–$NbSe_3$ contact without an intermediate metallic spacer. This allowed the spectra of reflected particles to be observed more distinctly with a maximal reflection amplitude of ~20%.

## 4. CRITICAL CURRENT FOR SUPPRESSING THE CDW GAP

It is well known that superconductivity is destructed by the electric current if the kinetic energy of a Cooper pair reaches a value comparable with the pairing energy $2\Delta$. This is the so-called depairing current. Continuing the analogy between the CDW slip state and superconductivity, we raise the question of the current-induced suppression of the CDW gap. A simple estimate of the critical velocity $v_c$ from the condition that the kinetic energy of a CDW must achieve a value equal to the CDW gap gives $v_c \sim (\Delta/M)^{1/2}$. For $\Delta \sim 100$ meV and $M = 100m_e$ [7], this gives $v_c \sim 10^5$ cm/s. This estimate seems to be reasonable, because it is smaller than the sound velocity in the materials with a CDW: the limiting CDW velocity probably cannot exceed the sound velocity because of the strong electron–phonon coupling, which provides the existence of the CDW. For a concentration of $10^{21}$–$10^{22}$ cm$^{-3}$ taken for the CDW-condensed electrons, one estimates the critical current density at $10^7$–$10^8$ A/cm$^2$. In bulk samples, current densities as high as those are difficult to achieve without Joule heating. However, it turned out that they can be achieved rather easily in microcontacts. In point contacts, the resistance is formed on the length scale $\sim a$, while the energy is scattered on the mean free path scale $l$ [34]. In the experimentally organized ballistic regime $a \ll l$, the electron velocities may reach very high values without heating the material.

The first evidence of the current-induced CDW-gap suppression was obtained in our experiments with Au–Au/$K_{0.3}MoO_3$ contacts [26]. For the contacts with different thicknesses of the Au sublayer (50–100 nm) and

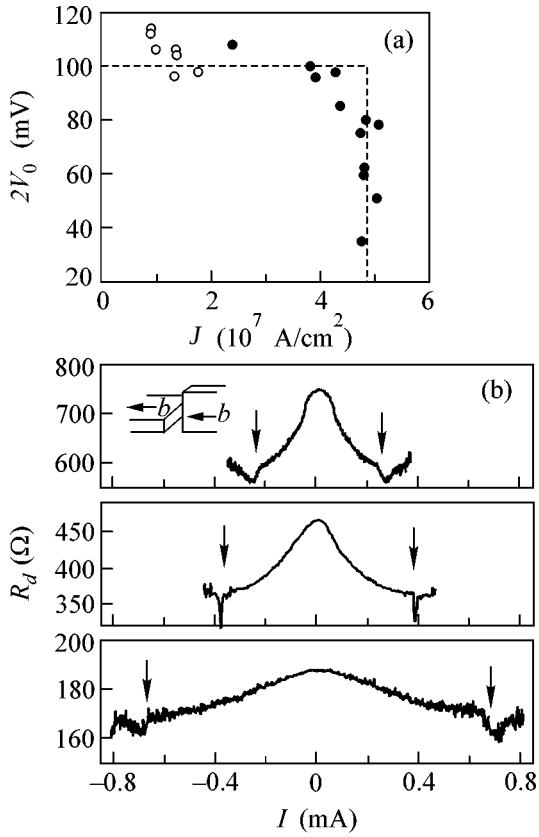


**Fig. 4.** (a) Characteristic voltage $2V_0$ determining the $K_{0.3}MoO_3$ CDW gap $2\Delta_0$ in the reflection spectra of the Au–$K_{0.3}MoO_3$ interface vs. current density through the interface [$d$ = (●) 50 and (○) 100 nm] at $T$ = 77 K. (b) The $R_d(I)$ spectra of the point contact $NbSe_3$–$NbSe_3$ formed along the conducting chains; the contact resistances (areas) are different in different panels. The contact geometry is schematically shown in the inset. The arrows indicate the characteristic jumps of differential resistance to the metallic state with $dR_d/dI > 0$ at currents exceeding $I_0$. Note that the product $I_0R_d$ determining the current density in the jump region is independent of the contact parameters.

different resistances (from several hundred to ten ohms), the Peierls gap in $K_{0.3}MoO_3$ was measured as a function of the current density passing through the contact. The contact diameter was calculated by the Sharvin formula [28]. The experiments showed a sharp narrowing of the gap (Fig. 4a) at current densities $\approx 5 \times 10^7$ A/cm$^2$. According to the estimates, the contact was heated by no more than 3 K. The critical CDW velocity $v_c = J_c/ne$ corresponding to this current density ($n$ is the concentration of condensed carriers) was $0.6 \times 10^5$ cm/s, which is several times lower than the sound velocity $c = 4.5 \times 10^5$ cm/s in $K_{0.3}MoO_3$ [35].

In the other group of our experiments with high current densities, the $NbSe_3$–$NbSe_3$ point contacts oriented along the chains were studied [36]. It was established that the nonlinear differential resistance $R_d$ caused by the contribution from the moving CDW drops abruptly with an increase in current and transforms into a state with a metallic character of the $R_d(I)$ dependence (Fig. 4b). The current density corresponding to the jump did not depend on the contact resistance and was of the same order of magnitude ($6 \times 10^7$ A/cm$^2$) as in the experiments of the first group. A value of $2.7 \times 10^5$ cm/s obtained for the corresponding CDW critical velocity in $NbSe_3$ also did not exceed the sound velocity in $NbSe_3$ ($5.5 \times 10^5$ cm/s [37]). The results obtained for different materials in independent experiments provide strong evidence for the existence of a universal mechanism of current-induced CDW-gap suppression. A more detailed understanding of this mechanism calls for further investigations, both theoretical and experimental.

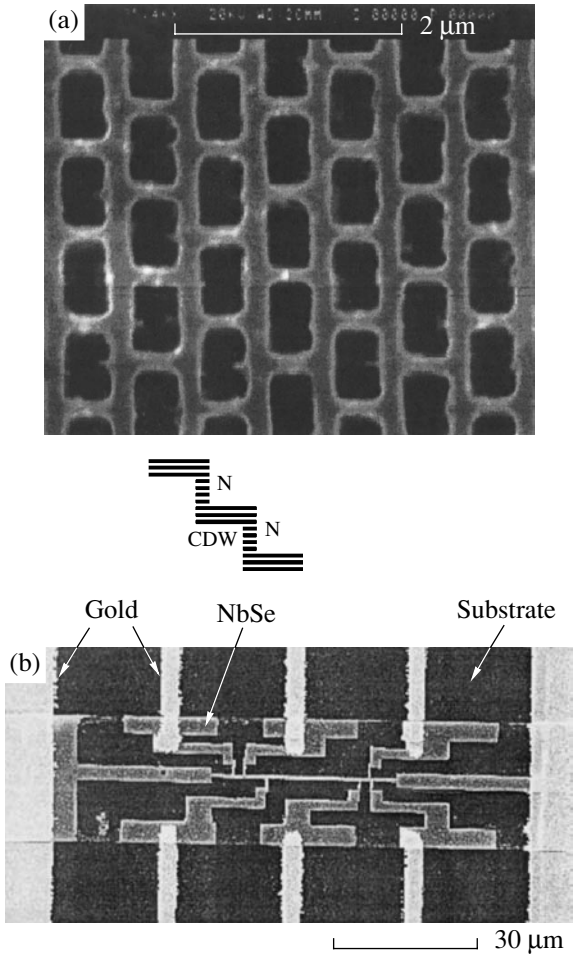


**Fig. 5.** Mesostructures obtained on thin $NbSe_3$ crystals by electron-beam lithography: (a) periodic 2D structure of antidots and (b) microline. The inset schematically demonstrates that the nonlinear transport in the antidot structure is caused by the contribution from only the short submicron sections along the conducting chains.

## 5. MESOSTRUCTURES ON $NbSe_3$

### *5.1. Structures Obtained Using Electron-Beam Lithography*

The use of modern technologies and, in particular, electron-beam lithography extended substantially the experimental possibilities for studying the CDW properties on the small-length scale. Below, two types of mesostructures are described which were obtained on $NbSe_3$ single crystals by electron-beam lithography and used for studying nonlinear CDW transport in segments as short as 0.5 μm. This made it possible to study the problem of CDW current conversion on the submicron length scale.

In early experiments of this type, we obtained structures containing periodic 2D rows of antidotes in thin $NbSe_3$ crystals [38] (Fig. 5a). The antidots constituted a triangular lattice in such a way that the CDW could move only inside a confined section between the antidots with a length equal to the lattice period along the chains ($b$ axis). In the transverse direction, these sections were electrically connected by linear conduction (inset in Fig. 5a). The resulting network contained from two to seven thousand cells, over which the single-cell properties were averaged.

The process of structure preparation included the fixation of a thin (<0.5 μm) sample on a substrate, coating it with a resist, the formation of a desired structural profile on the resist by electron-beam lithography, capping the resist with an Al mask (oblique evaporation), and etching the sample through the Al mask using plasmochemical etching ($SF_6$) [38]. The resulting periodic structures had a period from 3 to 0.5 μm along the $b$ axis. The smallest sizes of the conducting fragment along the $b$ axis were 0.5 μm with a cross section of $0.2 \times 0.3$ μm.

For the submicron-sized structures, the size effect consisting of a decrease in the linear conduction of the structure was observed below 40 K, when the carrier mean free path became greater than the minimal size of the structure [38]. This allowed the mean free path to be

estimated at $l \sim 0.3$ μm at $T \approx 40$ K. It was also established that the CDW-depinning threshold field increased almost fourfold upon decreasing the cell length from 1.5 to 0.5 μm [38] (see also [39]).

The process of CDW depinning in a finite-length section is usually accompanied by the formation of a PSC at the boundary (boundaries) with an immobile CDW. The reason is that the CDW phase is independent of time in the section with an immobile CDW, whereas it linearly increases with time in the section with a moving CDW. As a result, the order parameter turns to zero when the phase gradient at the boundary achieves its critical value and the phase "slips" by $2\pi$, after which the process is repeated periodically. This mechanism of CDW current conversion into quasiparticle current with the formation of the PSC was proposed by Gor'kov in [31]. More recently, the picture of current conversion was considered in more detail by Brazovskiĭ and Matveenko in [40].

In the general case, the formation of a PSC demands an additional energy associated with the CDW deformation in the near-contact region up to the critical values, with the formation of local phase-slip domains and the motion of corresponding dislocation loops to the sample surface. The corresponding CDW-depinning threshold voltage, measured between two contacts placed $L$ apart, can be expressed as [41] $V_t = E_t L + V_{ps}$, where $V_{ps}$ is the excess stress required for the formation of a PSC. It was previously thought that $V_{ps}$ is independent of the separation between the current contacts [i.e., $V_{ps}(L) = V_{ps0} \approx 1$ mV], based on experiments with $L$ decreasing to 20 μm [42]. Our experiments with the rows of submicron antidots allowed the energy of PSC formation to be estimated for $L \approx 0.5$ μm. It was found that the threshold voltage for the submicron sections is considerably (by a factor of 2–3) lower than $V_{ps0}$ [38]. This pointed to a considerable (by several times) decrease in the PSC formation energy on the submicron length scale. The obtained results were confirmed by the direct measurements of $V_{ps}$ in the individual microsections of a microline-type structure on $NbSe_3$ [43] with a distance between the probes varying from 7 to 0.5 μm (Fig. 5b). This effect cannot be explained within the framework of the available models of CDW current conversion [44], so new PSC models need to be developed for the mesoscopic samples. Qualitatively, the drop in $V_{ps}$ on a submicron length can be explained as follows. For large distances between the current contacts, the phase slip on them is uncorrelated. One can imagine that they become time-correlated with a decrease in distance; i.e., the addition of a CDW period in one contact is accompanied by the synchronous elimination of the CDW period in the other contact. Such a coherent phase slip requires weaker CDW deformation and, as a result, lower bias $V_{ps}$ than in the case of a large separation between the contacts [43].

Measurements on the periodic structure of antidots were used to compare the CDW conductivity $\sigma_{\text{micro}}^{CDW}$ of a submicron domain and $\sigma_{\text{macro}}^{CDW}$ of a macroscopic sample of the same geometry. This enabled us to estimate the length $l_{\text{conv}}$ of CDW current conversion into normal current. Assuming that the CDW in the submicron sample makes a contribution to the conductivity at the length $L - 2l_{\text{conv}}$, one has [38] $l_{\text{conv}} = \frac{1}{2}L(1 - \sigma_{\text{micro}}^{CDW}/\sigma_{\text{macro}}^{CDW})$. This estimate gives a value of 20 to 30 nm for $l_{\text{conv}}$, in agreement with the theoretical estimate $l_{\text{conv}} \sim h v_F/2\pi\Delta$ [31, 45].

### *5.2. Structures Obtained Using Focused Ion Beams*

One more efficient method for obtaining micro- and nanostructures consists of microetching with focused ion beams (FIB). This method has been intensively elaborated over the last decade mainly in connection with the appearance of stable liquid (gallium) cathodes and computer systems for controlling the ion beams and the microetching process. Commercial setups have already emerged with a resolution as high as 10 nm and currents of ~10 pA, which is superior to the resolution of electron-beam lithography. Another advantage of the FIB method is that there is no need for the resist and that it allows the preparation of 3D structures. The drawback is that the beam energy is rather high (from 16 to 30 kV), for which reason the defects can appear in the structure at a depth of ~30 nm along the beam and ~20 nm in the lateral direction. This renders the method less efficient in the preparation of structures with dimensions smaller than 50 nm.

Recently, we have used FIB to obtain submicron-sized mesostructures on the layered single crystals of high-$T_c$ superconductor $Bi_2Sr_2CaCu_2O_{8+x}$ [46, 47] with the aim of studying the interlayer tunneling of Cooper pairs and quasiparticles [48]. The methods developed were applied to the CDW materials with the object of preparing various microstructures on them. As an illustration of the FIB method, Fig. 6 shows the microphotographs of the structures of two types obtained by this method on the $NbSe_3$ single crystals: the first structure is of the planar microbridge type containing a hole with a diameter of 0.1 μm (Fig. 6a). This structure is designed for studying the Aharonov–Bohm effect on a single microhole with a trapped magnetic flux. These structures are currently under development. The second structure of the overlap type is designed for studying the transverse transport (transverse to the easily conducting *bc* layers) at a small area (Fig. 6b). The overlap length of the vertical cuts is less than 0.05 μm. The structures of the second type are considered below.

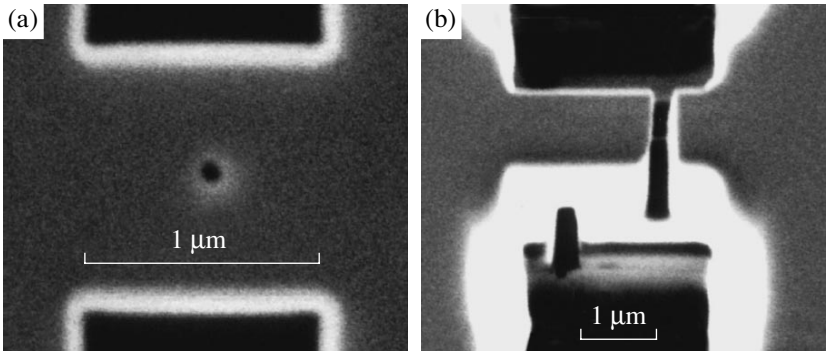


**Fig. 6.** Mesostructures obtained by the FIB method on thin $NbSe_3$ single crystals: (a) bridge containing a nanohole with a diameter of 80 nm and (b) overlap structure formed at the bridge by two lateral cuts overlapping by ~50 nm. The bridges in both cases are formed in the *bc* plane. The overlap structure is photographed at an angle of 45° to the *c* axis.

## 6. INTERLAYER TUNNELING IN $NbSe_3$

$NbSe_3$ has a well-defined layered structure. In conjunction with the conductivity anisotropy, this suggests that CDW may condense inside the elementary conducting layers separated by thin (on the atomic scale) isolating layers. In this case, similar to the layered high-$T_c$ superconductors [49], one can expect that the CDW order parameter is modulated along the $a^*$ axis perpendicular to the layers, so that transport across the layers is governed by the internal interlayer tunneling between the elementary layers with CDW. For the purpose of experimental verification of these premises, we carried out a direct experimental study [50] of the transport across the layers in $NbSe_3$ in the condensed state with CDW. Measurements were made on the layered mesostructures containing ~30 elementary layers (structures of the overlap type) with a small current-flow area ($S = 2 \times 2$ μm) across the layers and on the tight $NbSe_3$–$NbSe_3$ contacts oriented along the crystallographic axis $a^*$.

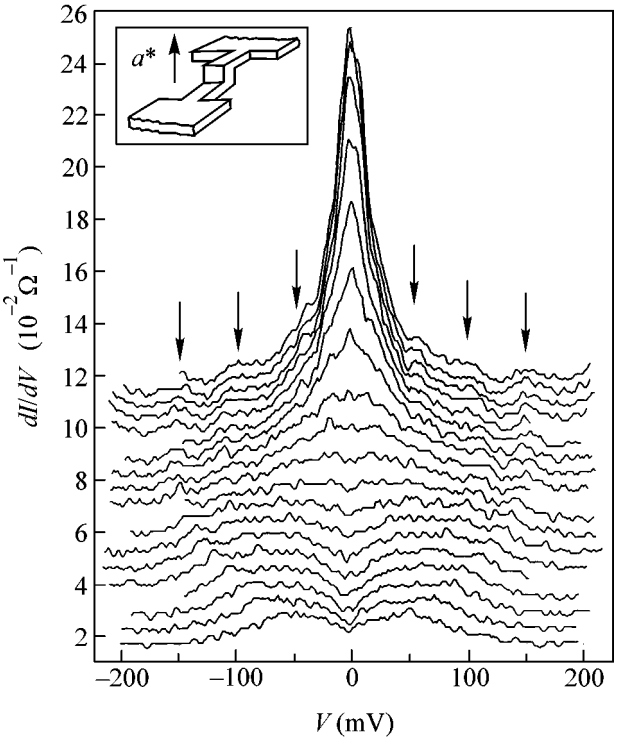


**Fig. 7.** The $dI/dV$ dependences as functions of bias $V$ in a high-quality overlap structure; $T$ = 59.5, 55.6, 52.1, 48.0, 43.7, 40.1, 37.0, 34.3, 31.0, 28.0, 25.1, 22.6, 19.1, 15.7, 12.8, 8.0, and 4.2 K. The dynamic conductivity scale corresponds to the curve for $T$ = 59.5 K. The remaining curves are shifted up for clarity. The configuration of the structure is schematically shown in the inset.

The most prominent feature of the measured characteristics of these structures was a strong conductivity peak observed at zero bias for both the overlap structures (Figs. 7, 8) and the point contacts (Fig. 8). In addition, the most perfect overlap structures showed a periodic peaking at $V = nV_0$ with $V_0$ = 50 mV (Fig. 7), analogous to the sequence of quasiparticle branches observed in the current–voltage characteristics of the layered Bi-2212 structures upon measuring across the layers [51]. Indeed, the value $V_0$ = 50 mV was close to twice the low-temperature $NbSe_3$ CDW gap, and the temperature dependence $V_0(T)$ corresponded to the BCS prediction. However, contrary to superconductors, the zero-bias conductivity was nonzero in $NbSe_3$. This indicates that the zero-bias interlayer conductivity is not due to the collective CDW contribution of the Josephson tunneling type.

It should be noted that, of all presently known quasi-one-dimensional compounds with CDW, $NbSe_3$ is a unique material. Whereas the ground state of the majority of compounds is semiconducting below the Peierls transition, $NbSe_3$ retains metallic properties down to the lowest temperatures. This is caused by the fact that the Fermi surface in the low-temperature Peierls state contains domains ("pockets") where the nesting conditions are not met, so the Peierls gap does not appear [7].

We managed to explain the data obtained by assuming that there is a coherent tunneling (tunneling with electron momentum conservation) of the CDW-noncondensed carriers. In this case, the theoretical calculation of the interlayer tunneling current–voltage characteristic yields the following expression for $eV < 2\Delta$ [50]:

$$I(V) = \frac{N(0)|t|^2\gamma eV}{2\pi^3(e^2V^2 + 4\gamma^2)}, \quad (2)$$

where $N(0)$ is the density of states in the pockets, $t$ is the matrix element for the interlayer tunneling with momentum conservation, $\gamma = \hbar\nu$, and $\nu$ is the collision frequency. The quantity $\gamma$ is determined by both the in-layer scattering ($\gamma_{sc}$) and the tunneling ($\gamma_{int}$) and can be represented as $\gamma = \gamma_{int} + \gamma_{sc}$. The expression for the dynamic conductivity has the form

$$\frac{\sigma(V)}{\sigma(0)} = 4\gamma^2\frac{4\gamma^2 - e^2V^2}{(e^2V^2 + 4\gamma^2)^2}. \quad (3)$$

One can see that the dynamic conductivity shows a peak at $V = 0$ with the width $\sim\gamma$ and becomes negative at $eV > 2\gamma$, indicating instability at these voltages. Based on the known data for the mobility $\mu = e/\nu_{sc}m^* \approx 4 \times 10^4$ cm$^2$/(V s) [52] and effective mass $m^* = 0/24m_e$ [53], one arrives at the following estimate for the in-layer scattering: $\gamma_{sc} = 0.13$ meV. A peak width of ~10 mV experimentally observed for the structure composed of 30 layers corresponds to $\gamma = 0.3$ meV. This implies that $\gamma_{int} \approx \gamma_{sc}$, and, hence, tunneling is coherent. In the interlayer electron tunneling, the energy is conserved [i.e., $\varepsilon(\mathbf{p}) = \varepsilon(\mathbf{q}) - eV$, where $\mathbf{p}$ and $\mathbf{q}$ are the electron momenta in the neighboring layers] to within $2\gamma$. For coherent tunneling, $\mathbf{p} = \mathbf{q}$ and $\varepsilon(\mathbf{p}) = \varepsilon(\mathbf{q})$, so that, if $eV \ll \gamma$, tunneling can occur and one arrives at the conventional Ohm's law. At $eV > \gamma$, tunneling cannot occur until $V$ achieves $2\Delta_p/e$. In this case, the CDW-condensed electrons start to contribute to the interlayer current via the usual tunneling of CDW quasiparticles through the doubled Peierls gap $2\Delta_p$. Therefore, the interlayer current can occur due to only one of the mechanisms described above. Because of the geometrical inhomogeneity of the layers in real multilayer structures (layer areas slightly differ from layer to layer), the voltage $V > 2\gamma/e$ cannot be achieved simultaneously for all individual tunneling transitions. At $V > 2\gamma/e$, some of the transitions occur in the coherent tunneling regime and some of them occur in the regime of single- particle tunneling through the gap. As a result, the current– voltage characteristic of the compound should display conductivity peaks at $V = 2n\Delta_p/e$, where $n = 1, 2, \ldots$. In the case of tight contacts, the incoherence of tunneling is enhanced, although it remains almost coherent in the best structures. As a result, the current–voltage characteristics of these structures show, in addition to the zero-bias conductivity peak, a singularity at $V = \Delta_p/e$ due to the single-particle tunneling of the N–I–CDW type.

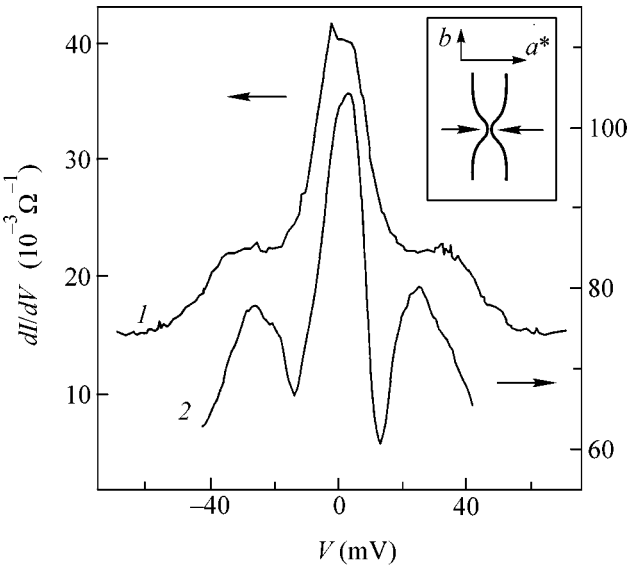


**Fig. 8.** The $dI/dV(V)$ dependences for (curve *1*) the tight $NbSe_3$–$NbSe_3$ point contact oriented along the $a^*$ axis and (curve *2*) the overlap structure with a planar defect. The configuration of the point contact is shown in the inset.

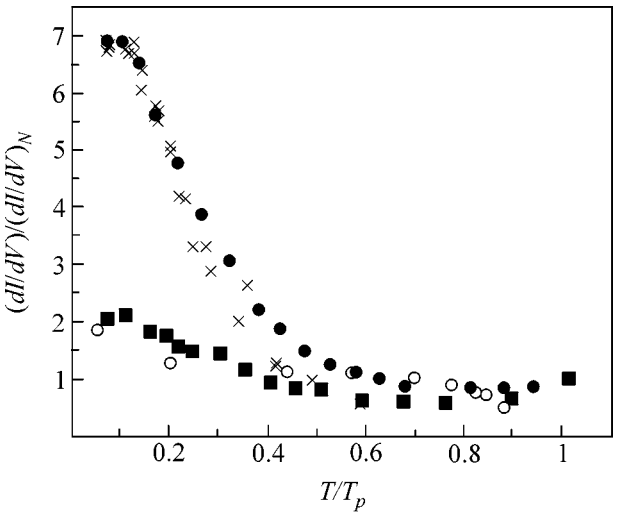


**Fig. 9.** Temperature dependences of the zero-bias dynamic conductivity: black circles correspond to the data obtained for a perfect overlap structure shown in Fig. 7; black squares correspond to the overlap structure with a defect; and empty circles correspond to the $NbSe_3$–$NbSe_3$ point contact. The conductivity is normalized to the $dI/dV$ value at $T = 62$ K. Crosses correspond to the theoretical dependence obtained from Eq. (2) and the known temperature dependence of mobility in $NbSe_3$ [52]. The quantity $\gamma_{int}$ was taken as a temperature-independent fitting parameter. The best agreement was obtained for $\gamma_{int}/\gamma_{sc} = 2$ at 4.2 K.

One can see that the temperature in Eq. (2) appears only in $\gamma(T)$. In this case, the zero-bias temperature dependence of conductivity, according to Eq. (2), is $\sigma(0, T) \propto [e\hbar/\mu(T)m^* + \gamma_{int}]^{-1}$. This dependence agrees rather well with the experiment (Fig. 9), if one takes the known in-layer $\mu(T)$ dependence [52] and assumes that $\gamma_{int}$ is independent of temperature. Thus, the saturation of $\sigma(0, T)$ at low temperatures can be explained by the saturation of $\mu(T)$ at $T \longrightarrow 0$.

It would be of interest to study the zero-bias conductivity peak in variously oriented magnetic fields. One can expect that a rather strong magnetic field perpendicular to the layers can change the momentum along the mean free path, leading to a decrease in the contribution from the coherent tunneling and, hence, to the peak suppression. It is also of interest to measure the angular dependence of magnetoresistance for a field rotated in the layer planes. This dependence can be used to determine the pocket orientations at the Fermi surface, similarly to that proposed in [54] for determining the directions of zeros of the order parameter in Bi-2212.

## 7. CONCLUSIONS

We have considered some experiments that were aimed at searching for quantum coherence in the materials with CDW on small length scales. Quantum coherence was observed in the interference of a CDW moving in the columnar defects with trapped magnetic flux; in the local reflection of carriers at the N–CDW interface; and in the interlayer tunneling of carriers localized in Fermi-surface pockets without a CDW gap. Further development of these studies will allow us to gain a better insight into the quantum nature of charge-density waves.

## REFERENCES


1. R. E. Peierls, Ann. Phys. **4**, 121 (1930); *Quantum Theory of Solids* (Oxford Univ. Press, Oxford, 1955), p. 108.
2. H. Frohlich, Proc. R. Soc. London, Ser. A **223**, 296 (1954).
3. J. Bardeen, Phys. Rev. Lett. **42**, 1498 (1979); **45**, 1978 (1980); **55**, 1010 (1985).
4. E. N. Bogachek, I. V. Krive, I. O. Kulik, and S. A. Rozhavsky, Phys. Rev. B **42**, 7614 (1990).
5. A. L. Kasatkin and É. A. Pashitskiĭ, Fiz. Nizk. Temp. **10**, 1222 (1984) [Sov. J. Low Temp. Phys. **10**, 640 (1984)]; A. L. Kasatkin and É. A. Pashitskiĭ, Fiz. Tverd. Tela (Leningrad) **27**, 2417 (1985) [Sov. Phys. Solid State **27**, 1448 (1985)].
6. M. I. Visscher and G. E. W. Bauer, Phys. Rev. B **54**, 2798 (1996).
7. *Density Waves in Solids*, Ed. by G. Gruener (Addison-Wesley, Reading, 1994).
8. Yu. I. Latyshev, P. Monceau, O. Laborde, and B. Pannetier, Synth. Met. **103**, 2582 (1999).
9. G. Grüner, A. Zavadovski, and P. M. Chaikin, Phys. Rev. Lett. **46**, 511 (1981); H. Fukuyama and P. A. Lee, Phys. Rev. B **17**, 535 (1978); P. A. Lee and T. M. Rice, Phys. Rev. B **19**, 3970 (1979).
10. L. Sneddon, M. C. Cross, and D. S. Fisher, Phys. Rev. Lett. **49**, 292 (1982).
11. S. V. Zaitsev-Zotov, Phys. Rev. Lett. **71**, 605 (1993).
12. F. Ya. Nad', Pis'ma Zh. Éksp. Teor. Fiz. **58**, 107 (1993) [JETP Lett. **58**, 111 (1993)].
13. Yu. I. Latysev, O. Laborde, P. Monceau, and S. Klaumuenzer, Phys. Rev. Lett. **78**, 919 (1997).
14. Yu. I. Latyshev, O. Laborde, Th. Fournier, and P. Monceau, Phys. Rev. B **60**, 14019 (1999).
15. Yimei Zhu, Z. X. Cai, R. C. Budhani, *et al.*, Phys. Rev. B **48**, 6436 (1993).
16. Y. Aharonov and D. Bohm, Phys. Rev. **115**, 485 (1959).
17. M. S. Shervin and A. Zettl, Phys. Rev. B **32**, 5536 (1985).
18. B. L. Al'tshuler, A. G. Aronov, B. Z. Spivak, *et al.*, Pis'ma Zh. Éksp. Teor. Fiz. **35**, 476 (1982) [JETP Lett. **35**, 588 (1982)].
19. M. I. Visscher and B. Rejaei, Europhys. Lett. **43**, 617 (1998).
20. A. S. Rozhavskiĭ, Fiz. Nizk. Temp. **24**, 880 (1998) [Low Temp. Phys. **24**, 662 (1998)].
21. J. H. Miller, Jr., C. Ordóñez, and E. Prodan, Phys. Rev. Lett. **84**, 1555 (2000).
22. A. F. Andreev, Zh. Éksp. Teor. Fiz. **46**, 1823 (1964) [Sov. Phys. JETP **19**, 1228 (1964)].
23. P. C. van Son, H. van Kempen, and P. Wyder, Phys. Rev. Lett. **59**, 2226 (1987).
24. G. E. Blonder, M. Tinkham, and T. M. Klapwijk, Phys. Rev. B **25**, 4515 (1982).
25. A. A. Sinchenko, Yu. I. Latyshev, S. G. Zybtsev, *et al.*, Pis'ma Zh. Éksp. Teor. Fiz. **64**, 259 (1996) [JETP Lett. **64**, 285 (1996)].
26. A. A. Sinchenko, Yu. I. Latyshev, S. G. Zybtsev, and I. G. Gorlova, Zh. Éksp. Teor. Fiz. **113**, 1830 (1998) [JETP **86**, 1001 (1998)].
27. C. Schlenker, J. Duma, *et al.*, Philos. Mag. B **52**, 643 (1985).
28. Yu. V. Sharvin, Zh. Éksp. Teor. Fiz. **48**, 984 (1965) [Sov. Phys. JETP **21**, 655 (1965)].
29. B. Rejaei and G. E. W. Bauer, Phys. Rev. B **54**, 8487 (1996).
30. S. N. Artemenko and S. V. Remizov, Pis'ma Zh. Éksp. Teor. Fiz. **65**, 50 (1997) [JETP Lett. **65**, 53 (1997)].
31. L. P. Gor'kov, Zh. Éksp. Teor. Fiz. **86**, 1818 (1984) [Sov. Phys. JETP **59**, 1057 (1984)].
32. A. A. Sinchenko, Yu. I. Latyshev, S. G. Zybtsev, *et al.*, Phys. Rev. B **60**, 4624 (1999).
33. T. Ekino and J. Akimitsu, J. Appl. Phys. **26**, 625 (1987); Physica B (Amsterdam) **194–196**, 1221 (1994); Zhenxi Dai, C. G. Slough, and R. V. Coleman, Phys. Rev. Lett. **66**, 1318 (1991); Phys. Rev. B **45**, 9469 (1992); A. Fournel, J. P. Sorbier, M. Konczykovski, and P. Monceau, Phys. Rev. Lett. **57**, 2199 (1986); J. P. Sorbier, H. Tortel, P. Monceau, and F. Levy, Phys. Rev. Lett. **76**, 676 (1996).

34. I. O. Kulik, A. N. Omel'yanchuk, and R. I. Shekhter, Fiz. Nizk. Temp. **3**, 1543 (1977) [Sov. J. Low Temp. Phys. **3**, 740 (1977)].
35. M. Saint-Paul and G. X. Tassema, Phys. Rev. B **39**, 8736 (1989).
36. A. A. Sinchenko, V. Ya. Pokrovski, S. G. Zybtsev, *et al.*, cond-mat/0101124.
37. P. Monceau, L. Bernard, R. Currat, *et al.*, Synth. Met. **19**, 819 (1987).
38. Yu. I. Latyshev, B. Pannetier, and P. Monceau, Eur. Phys. J. B **3**, 421 (1998).
39. S. V. Zaitsev-Zotov, V. Ya. Pokrovskii, and J. C. Gill, J. Phys. I **2**, 111 (1992).
40. S. A. Brazovskiĭ and S. I. Matveenko, Zh. Éksp. Teor. Fiz. **101**, 1620 (1992) [Sov. Phys. JETP **74**, 864 (1992)].
41. J. C. Gill, Physica B (Amsterdam) **143**, 49 (1986).
42. M. P. Maher, T. L. Adelman, D. A. DiCarlo, *et al.*, Phys. Rev. B **52**, 13850 (1995).
43. O. C. Mantel, F. Chalin, C. Dekker, *et al.*, Phys. Rev. Lett. **84**, 538 (2000).
44. S. Ramakrishna, M. P. Maher, V. Ambegaokar, and V. Ekkern, Phys. Rev. Lett. **68**, 2066 (1992); S. Ramakrishna, Phys. Rev. B **48**, 5025 (1993).
45. S. A. Brazovskiĭ, Zh. Éksp. Teor. Fiz. **78**, 677 (1980) [Sov. Phys. JETP **51**, 342 (1980)].
46. Yu. I. Latyshev, S.-J. Kim, and T. Yamashita, IEEE Trans. Appl. Supercond. **9**, 4312 (1999).
47. S.-J. Kim, Yu. I. Latyshev, and T. Yamashita, Supercond. Sci. Technol. **12**, 729 (1999).
48. Yu. I. Latyshev, T. Yamashita, L. N. Bulaevskii, *et al.*, Phys. Rev. Lett. **82**, 5345 (1999).
49. R. Kleiner and P. Müller, Phys. Rev. B **49**, 1327 (1994).
50. Yu. I. Latyshev, A. A. Sinchenko, L. N. Bulaevskiĭ, *et al.*, Pis'ma Zh. Éksp. Teor. Fiz. **75**, 103 (2002) [JETP Lett. **75**, 93 (2002)].
51. R. Kleiner, P. Müller, H. Kohlstedt, *et al.*, Phys. Rev. B **50**, 3942 (1994).
52. N. P. Ong and J. W. Brill, Phys. Rev. B **18**, 5265 (1978).
53. R. V. Coleman, M. P. Everson, Hao-An Lu, *et al.*, Phys. Rev. B **41**, 460 (1990).
54. L. N. Bulaevskii, M. J. Graf, and M. P. Maley, Phys. Rev. Lett. **83**, 388 (1999).

*Translated by V. Sakun*